Alma Mater Studiorum - Università di Bologna

DOTTORATO DI RICERCA IN

NANOSCIENZE PER LA MEDICINA E PER L'AMBIENTE

Ciclo 33

Settore Concorsuale: 03/B1 - FONDAMENTI DELLE SCIENZE CHIMICHE E SISTEMI INORGANICI

Settore Scientifico Disciplinare: CHIM/03 - CHIMICA GENERALE E INORGANICA

CRYSTAL ENGINEERING STRATEGIES FOR A HEALTHIER ENVIRONMENT: SOLID-STATE SYNTHESES AND CHARACTERIZATION OF ORGANIC/INORGANIC CO-CRYSTALS AND HOST-GUEST SYSTEMS WITH IMPROVED STABILITY AND PERFORMANCE ACTIVITIES.

Presentata da: Lucia Casali

Coordinatore Dottorato

Dario Braga

Supervisore

Fabrizia Grepioni

Co-supervisore

Dario Braga

Esame finale anno 2021

INDEX

References

Part I – Urea co-crystals

ABSTRACT

In a society increasingly aware of and concerned about environmental issues, chemistry is being asked to promote sustainability through the development of processes less impacting on the environment and of products environmentally friendly. In this context, the field of chemistry referred as crystal engineering can play a major role in the quest for sustainability. By exploiting sustainable synthetic methodologies - first of all the mechanochemical method - crystal engineering can guide solid-state modifications in order to obtain crystalline materials with an improved sustainable character.

This doctoral research activity addressed the synthesis and characterization of environmentally friendly crystalline materials. Two different lines of research were undertaken:

- *Optimization of materials of agrochemical interest, mainly through the co-crystallization method.*

The first systems investigated were urea-based co-crystals, designed (i) to improve the chemical-physical properties of urea by reducing its water solubility/dissolution rate and (ii) to exert an inhibition activity towards the soil enzymes urease and ammonia monooxygenase (AMO). The work resulted in the publication of three papers, which are presented in Chapter 2.

A further development of this research project concerned the synthesis and characterization of crystalline materials based on AMO inhibitors, aimed to modulate the physico-chemical properties of such inhibitors in terms of water solubility, thermal stability, and inhibition activity. The experiments discussed in Chapter 3 are quite promising: a paper has been submitted upon invitation, and two more manuscripts are in preparation.

- *Improvement in the photostability of organic UV filters commonly used in sunscreen formulations through their inclusion into β-cyclodextrin.*

The inclusion complexes of β-cyclodextrin with the UV filters avobenzone and octinoxate were synthesized and proved to possess the desired properties. The results led to the publication of a paper, which is presented in Chapter 4.

LIST OF ABBREVIATIONS AND ACRONYMS

AMO – ammonia monooxygenase

API(s) – Active Pharmaceutical Ingredient(s)

β-CD – β-cyclodextrin

CSD – Cambridge Structural Database

DCD - Dicyandiamide

DSC – Differential Scanning Calorimetry

IC(s) – Inclusion Complex(es)

IR – Infrared Spectroscopy

ICC(s) – Ionic Co-Crystal(s)

NMR- Nuclear Magnetic Resonance Spectroscopy

SCXRD – Single Crystal X-Ray Diffraction

TGA – Thermal Gravimetric Analysis

VT XRPD – Variable Temperature X-Ray Powder Diffraction

XRPD – X-Ray Powder Diffraction.

CHAPTER 1
INTRODUCTION

1.1 Crystal engineering

Over the last decades, the concept of chemistry changed considerably, evolving from pure molecular chemistry to the more sophisticated supramolecular chemistry.[1] The principle behind this field relies on the spontaneous self-assembly of molecular components into high-performing systems, able to accomplish more complex functions with respect to the simple components. Therefore, such systems were found to play a key-role in the scientific progress, with beneficial effects on essential areas such as medicine,[2] electronics[3] and catalysis,[4] just to name a few.

Given the potential of such discipline, the quest for supramolecular systems has affected all the fields of chemistry,[5,6] both in solution and in the solid-state. With regard to the latter, crystals turned out to be objects of interest for supramolecular purposes, resulting in one of the most investigated systems among the solid-state materials. In fact, according to the definition by Dunitz, *a crystal is, in a sense, the supramolecule par excellence: a lump of matter, of macroscopic dimensions, millions of molecules long, held together in a periodic arrangement by just the same kind of interactions as are responsible for molecular recognition and complexation at all levels - ion-ion, ion-dipole, dipole-dipole interactions, hydrogen bonding, London forces, and so on*.[7] Therefore, crystalline materials follow the principles of the supramolecular chemistry, which can be referred to as 'crystal engineering' for this specific area.

According to the definition provided by Desiraju in 1989, crystal engineering is defined as *the understanding of intermolecular interactions in the context of crystal packing and the utilization of such understanding in the design of new solids with desired physical and chemical properties.*[8] The first occurrences concerning this field date back to a few decades before, first with the brief note by Pepinsky in 1955 entitled *Crystal Engineering: A New Concept in Crystallography* [9] and then with Schmidt's research into solid-state photochemical reactivity,[10] which resulted in the knowledge that it is possible to control the solid-state behavior using crystal engineering principles.

By exploiting the stages of modeling, synthesis, characterisation and evaluation of the properties, crystal engineering is aimed to design and manufacture novel crystalline materials through the control on the solid-state assembly of chemical building blocks via non-covalent interactions.[11]

Since intermolecular interactions acquire great significance in the context of crystal engineering, an understanding of these interactions in chemical and energy terms represents the first step in the design of a crystal engineering experiment (Table 1).[12]

Interaction	*Energy (kJ/mol)*
Hydrogen bonding	
Strong	>85
Moderate	15-85
Weak	5-15
Halogen bonding	5-45
Ionic and dipolar interactions	
ion - ion	200-300
Ion - dipole	50-200
dipole - dipole	5-50
π interactions	2-50

Table 1: summary of the main supramolecular interactions.

1.1.1. Intermolecular interactions

Hydrogen bond

The hydrogen bond is an attractive interaction between a hydrogen atom from a molecule or a molecular fragment X-H in which X is more electronegative than H, and an atom or a group of atoms in the same or a different molecule (Y), in which there is evidence of bond formation (Fig.1).[13] Specifically, donors are groups with a hydrogen atom attached to electronegative atoms such as oxygen or nitrogen, so that a dipole is formed with a partial positive charge on the H-atom; on the other hand, acceptors are electron-rich atoms/bonds that can interact with the H-atom. The groups involved in a hydrogen bond can also bear a formal charge, as for $[N\text{-}H]^+$ donors or carboxylate acceptors, thus resulting in a *charged-assisted* bond:[14] the electrostatic dipole-dipole component of hydrogen bonding is enhanced, so this bond is generally stronger than its “neutral” counterpart.

The strength of the hydrogen bond varies with the electronegativity of the atoms X and Y, as also with the geometry and the environment in which the hydrogen bond takes place.[14] As a result, hydrogen bond is commonly divided into three categories, i.e. strong, moderate and weak hydrogen bonds:[15] strong hydrogen bonds present a quasi-covalent nature and are close to linearity (170-180°), moderate hydrogen bonds are largely electrostatic and weak hydrogen bonds are mainly stabilized by dispersive interactions.

Hydrogen bonds drive and control crystal packing by combining strength with directionality, resulting in one of the most powerful tool for supramolecular synthesis.[16]

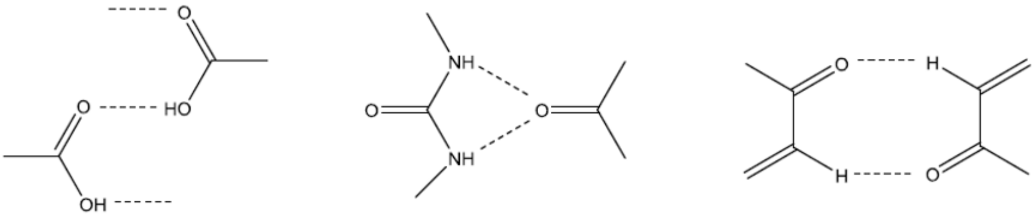

Fig.1: examples of hydrogen bonds.

Halogen bond

The halogen bond occurs when there is evidence of a net attractive interaction between an electrophilic region associated with a halogen atom in a molecular entity and a nucleophilic region in other, or the same, molecular entity (Fig.2).[17,18] The interaction energy follows the trend I>Br>Cl>F, with I-atoms involved in the strongest bonds.

Similar to hydrogen bond, halogen bond displays directional preferences, especially for the linear arrangements, thus gaining increasing interest in the crystal engineering context.[19]

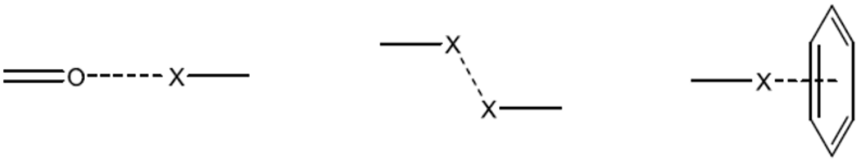

Fig.2: examples of halogen bonds.

Ionic and dipolar interactions

Ionic and dipolar interactions - ion-ion, ion-dipole and dipole-dipole interactions - arise from the electrostatic interactions between charges.

The ion-ion interactions - the strongest ones - rely on high charge densities, therefore they generally act on long range distances and do not display a directional arrangement.

For the ion-dipole interactions, it is possible to drive the spatial arrangement especially with regard to the metal-ligand coordination, since the number of links expected as well as the geometry of the binding center are (at least in the case of d-block metals) predictable.[20]

Finally, the dipole-dipole interaction can arrange itself in a parallel or orthogonal way - thus displaying a sort of directional preference - as a result of the balance between repulsive and attractive forces and of the shape of the components involved (Fig.3).

All these features make these interactions extensively exploited in the crystal engineering field for the design of new materials.[21]

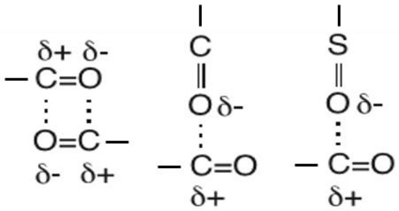

Fig.3: examples of different arrangements for dipole-dipole interactions.

π interactions

π interactions can be essentially of two types, depending on how the aromatic rings are oriented towards each other: the aryl edge-face (EF) mode and the aryl offset face-face (OFF) mode (Fig.4).[22] In the first case, the C-H···π interaction is formed as a result of the herringbone arrangement of the molecules, while the OFF mode is based on π···π interactions between molecules on top of each other (π stacking).

Generally, small molecules base their arrangement on the EF mode, large molecules on the OFF mode while intermediate size molecules can form both the interactions giving rise to a sandwich herringbone crystal.[23]

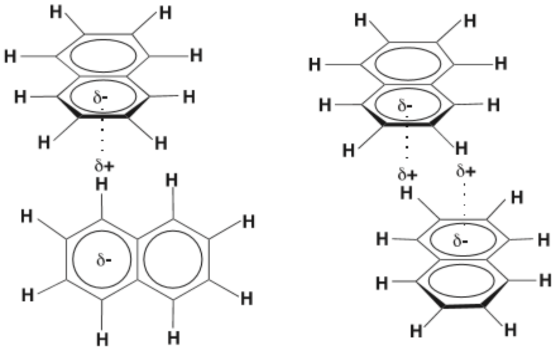

Fig.4: the aryl edge-face (EF) mode and the aryl offset face-face (OFF) mode (ref.12).

1.1.2 Supramolecular synthons

Along with the understanding of the nature and the energies of the intermolecular interactions that can occur between the components of a crystal, crystal engineering is based on an intentional and controlled use of such interactions. For this purpose, it is useful to find out the preferred spatial arrangement(s) of these interactions, i.e. the synthon(s).[24]

According to the definition provided by Desiraju in 1995, a synthon is *an identifiable pattern of interacting molecular groups that is likely to be repeated in other crystal structures that contain the same molecular functional groups. These linkers largely control how the individual molecules will assemble as crystals for both organic and inorganic substances* (Fig.5).[25] It follows that the most robust synthons for a given functional group are the most frequent ones, so it is theoretically possible to predict the preferred arrangements of such group in a crystal. [26]

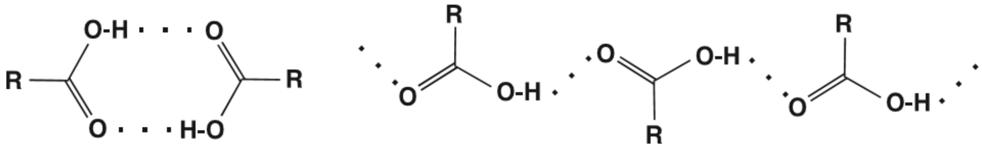

Fig.5: example of synthons - two possible arrangements for the carboxylic acids.

The next step in a crystal engineering experiment is to draw on all the crystallographic structures available and perform a statistical analysis of intermolecular interaction motifs and packing patterns. This function is doubly fulfilled by the CSD database[27] and the program Mercury.[28]

The CSD database gathers organic and organic-inorganic crystal structures, thus resulting in a highly effective means in the design of a crystal engineering experiment. The potential of such tool was acknowledged in 1983 by Allen and Kennard, which noted that *the systematic analysis of large numbers of related structures is a powerful research technique, capable of yielding results that could not be obtained by any other method*.[29]

Through the program Mercury, it is possible to to identify supramolecular synthons for a given functional group or to identify crystal structures containing a particular geometrical arrangement of the atoms, thus providing the potential crystal packing features on the basis of the chemical groups in the molecules.

However, it should be specified that the prediction of the crystal structure of a compound before any experiment is carried out is still a serious challenge. In fact, a crystal structure is just one of the many in the thermodynamic landscape of a crystal and the transition to a different energy minimum can be triggered by random and unforeseen events.

Therefore, the understanding of all the intermolecular interactions in energy and geometrical terms does help - but not guarantee – in predicting the outcome of a crystallization process. Because of the strong dependence of such process on the experimental conditions, this theoretical approach must always be accompanied by the experimental work.

1.1.3 Multiple crystal forms

The fundamental physicochemical properties of crystalline materials depend on the arrangement of the molecules: different crystalline forms of the same molecule can display different properties.

The crystallization process may result in the formation of several products,[30] especially when more than one component is involved in the process. In Fig.6 a number of possible products is shown, i.e. amorphous materials,[31] hydrates and solvates,[32] polymorphs,[33] molecular and ionic co-crystals,[34] salts[35] and solid solutions.[36,37]

Co-crystals, hydrates and polymorphs are the main crystalline forms investigated in this research project, therefore they are presented more in detail later in this section.

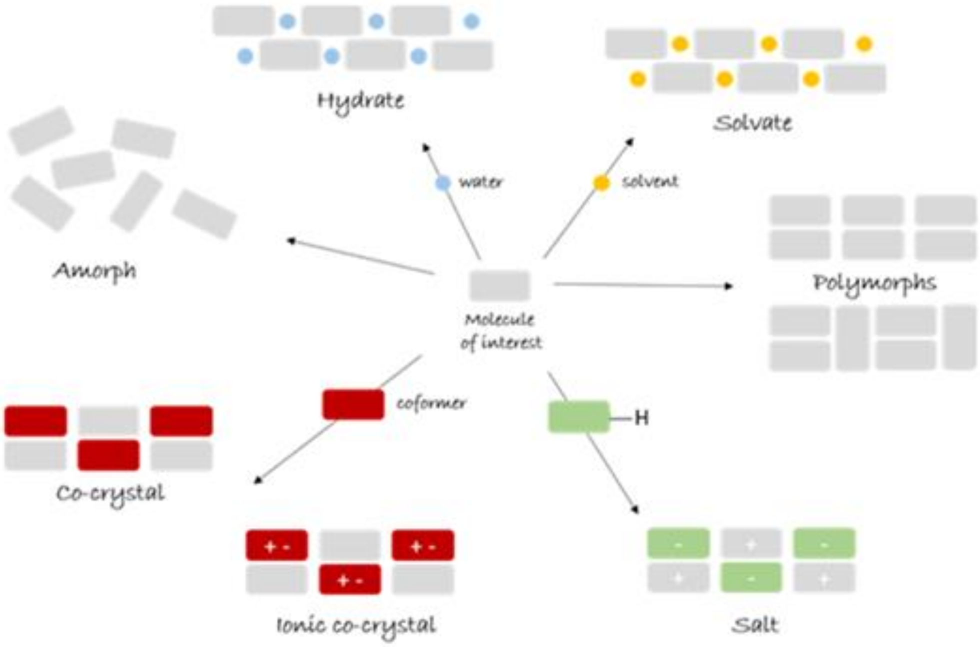

Fig.6: Schematic representation of the structural relationship between polymorphs, hydrates, solvates, co-crystals, salts and amorphs.

Polymorphs

Polymorphism is the ability of a given compound to crystallize in at least two different packing arrangements, resulting in materials with identical chemical composition but different spatial arrangement.[38]

Although such phenomenon was first recognized in 1822,[39] and further investigated in the years after,[40] polymorphism returned to gain interest quite recently, along with the understanding that the distribution of the molecules strongly influences the properties of a material. In fact, polymorphs can exhibit different solubility, hygroscopicity, melting point and compressibility, thus drawing the attention of the scientists working in the field of crystal engineering.

The main processes responsible of the spatial arrangement are nucleation and crystal growth. Given the impossibility of executing a full control on these determining steps, thus driving the molecular self-assembly towards the desired crystal form, polymorphism presents an intrinsic serendipitous nature.[41] In fact, external factors such as solvent and temperature can lead to the formation of unpredictable or multiple polymorphs, with unexpected implications in term of manufactory and reproducibility.[42]

Despite the great progress in the understanding of the phenomenon of polymorphism, we are still far from controlling such phenomenon: the computational prediction is not capable of foretelling the exact number of observable polymorphic forms of even the simplest molecules and an exhaustive experimental screening would require an infinite time. As stressed by McCrone, the *number of forms known for a given compound is proportional to the time and money spent in research on that compound.*[43]

Solvates and hydrates

Solvates are crystalline solids containing solvent molecules in a fixed (stoichiometry solvates) or variable (non-stochiometric solvates) amount.

Since several work-up processes are water-based, a compound is more likely to be exposed to water than organic solvents, and hydrates are formed.[44] Because of the extremely effective hydrogen bonds that water can form with molecules, the incidence of hydrates is quite impressive.[45]

The incorporation of water molecules into the crystal can induce a distribution of the molecules different from that of the anhydrate, so the physical properties of the hydrates may differ from those of the anhydrates.

Molecular and ionic co-crystals

The definition of co-crystal has been extensively debated in the academic literature over the last years.[46,47] Starting from the generic assumption that a co-crystal is a multi-component molecular crystal,[48] more specific definitions have been proposed,[49] with the aim of ruling out other types of crystalline materials such as solvates, hydrates, clathrates, salts and non-stoichiometric compounds. Zaworotko and coworkers, for example, have stated that a molecular co-crystal is a multiple component crystal where neutral molecular components are present in a definite stoichiometric ratio and all the components, when pure, are solid under ambient conditions.[50] Similarly, Aakeröy and Salmon have proposed the following criteria to define a molecular co-crystal, i.e. (1) only compounds constructed from discrete neutral molecular species are considered, (2) the components should be solids at ambient conditions and (3) the crystal must be a structurally homogeneous crystalline material containing two or more neutral building blocks in well-defined stoichiometric amounts.

The search for an unambiguous definition of co-crystal is due to the increasing importance that these materials are assuming in both the industrial and academic fields, especially for the pharmaceutical sector.[52] In fact, co-crystals offer multiple opportunities to modify the chemical and physical properties of an API, without making or breaking covalent bonds, but by changing its crystalline habit. Consequently, through a controlled co-crystallization of an API it is possible to dramatically expand the range of solid forms available for the formulation, obtaining in this way crystalline materials with different properties, such as habit, bulk density, solubility, compressibility, melting point, hygroscopicity, stability, bioavailability and dissolution rate.[34]

Co-crystallization is often aimed to transform amorphous or hard-to-crystallize APIs into crystalline products, which are generally preferred because of their easier and more reproducible characterization, lower hygroscopicity and greater chemical stability with respect to amorphs. Co-crystal formation plays a pivotal role also in the modulation of the solubility of an API, which can be increased or lowered depending on the nature of the other component(s), i.e. the co-former(s).[53]

When a co-former is an inorganic salt, a co-crystal is specifically defined as an ionic co-crystal. Although the first intentional crystallization of an organic molecule with a salt dates back to 1946,[54] a widespread use of ionic co-crystals began to occur recently, with the paper on the 'serendipitous' co-crystallization of barbituric acid with KBr.[55]

ICCs fall into the category of organic-inorganic compounds along with salts, metal organic framework, ionic liquids and deep eutectic mixtures. The advantage of ICCs over these other forms is given to the fact that there is no limit on the types of compounds which can be co-crystallized,[56] thus expanding the landscape of these materials. In terms of structure and intermolecular bonding features, these compounds do not differ from classical coordination compounds - except for the purposeful preparation behind them.[51]

ICCs are based on electrostatic interactions - oxygen or nitrogen atoms are usually electron donors towards the metal cations - with the possible additional contribution of hydrogen bonds between HB donors and anions ($OH\cdots Cl^-$, $NH\cdots Br^-$).[57] Because of the strong Coulombic interactions, the change in physicochemical properties is definitely more dramatic than in molecular co-crystals.

Since several inorganic salts are admitted by the pharmacopoeia, they result in suitable co-formers also for pharmaceutical applications, not to mention that they can possess pharmacological activity themselves.[85]

1.2 Mechanochemistry: a sustainable synthetic method

In the early nineties, Anastas and Warner introduced the concept of Green Chemistry, defined as the *design of chemical products and processes to reduce or eliminate the use and generation of hazardous substances*.[58] From a first ideal concept, the Green Chemistry manifesto was then structured, with the Twelve Principles as a guide for the design of new chemical products and processes.

Industrial processes are still heavily dependent on the use of solvents environmentally problematic, hazardous and energy-demanding during the production, purification and recycling steps.[59] The quest for green and sustainable industrial processes paved the way for alternative reaction media such as DES (Deep Eutectic Solvents),[60] ionic liquids[61] and supercritical carbon dioxide.[62] Even more remarkable is the possibility to break away from solvents, as for the mechanochemical method.

With the term mechanochemistry is meant that set of reactions, generally between solid materials, induced by the input of mechanical energy.[63] Although mechanochemistry has been known for centuries and Wilhelm Ostwald assessed the importance of such discipline already in the early 1900s,[64,65] it has been resumed quite recently.[66,67]

Mechanochemistry presents an intrinsically sustainable character, since reactions are quick, often quantitative and occur in the absence of solvent (grinding) or in the presence of a minimum amount of it (kneading).[68] Recent works in mechano-synthesis of small organic molecules[69] and metal–organic materials[70] suggest that mechanochemical methods can bring about approximately 10000-fold improvements in the solvent- and energy-usage.

With regard to the crystal engineering field, this method presents a whole range of benefits such as product crystallinity, control on stoichiometric composition and ability to generate crystalline materials regardless of the relative solubilities of the starting components.[71]

Beyond these advantages, mechanochemistry brings considerable improvements over the common solution-based methods in terms of crystallization control. In fact, the course of the reaction can be modulated by changing the milling conditions, such as the amount of solvent and the milling time.[72,73] Moreover, thanks to the development of new techniques, it is possible to monitor the course of such reactions,[74,75] thus getting into the details of the transformation process at the molecular and crystalline levels.

In view of these overall considerations, mechanochemistry turned out to be the preferential synthetic method adopted in my research activity. However, given the difficulties in obtaining crystallographic information from powder diffraction data, the mechanochemical synthesis was always performed along with the solution-based one, as the latter could yield single crystals suitable for single crystal X-ray diffraction and crystal structure determination.

1.3 Aim of the work

My PhD research activity was addressed to the synthesis and characterization of environmentally friendly crystalline materials. I took up two different lines of research, which differ essentially in the field of application for which these materials are intended:

- Optimization of materials of agrochemical interest mainly through the co-crystallization method.[76–78] Specifically, the aim of the project was to improve the chemical-physical properties of plants nutrients and inhibitors of the enzymes urease and AMO, in terms of thermal stability, hygroscopicity and solubility.

  The quest for innovative agrochemical materials was the main topic of my research activity: I worked on this project during all the three years of my PhD.

  The research activity was carried out in collaboration with the research group of prof. Stefano Ciurli - Laboratory of Bioinorganic Chemistry, Department of Pharmacy and Biotechnology, University of Bologna - which tested the inhibition activity of these materials towards the enzymes urease and AMO.

A further development of this research project concerned the synthesis and characterization of crystalline materials based on AMO inhibitors. A more in-depth solid-state characterization of these materials was performed at the research institute BAM - Federal Institute for Materials Research and Testing, Berlin - where I spent the last three months of my PhD under the supervision of Dr.Franziska Emmerling.

- Improvement in the photostability of organic UV filters commonly used in sunscreen formulation through the inclusion of such compounds into the β-CD cavity.[79]
  This project was a branch line of my research activity, on which I worked during the second year of my PhD program.

In the following chapters, an overview of the two topics is presented.
For copyright reasons, the manuscripts cannot be reproduced in this dissertation, but the links to the published material will be provided. The supporting information related to published works is instead reproduced here, as an evidence of the experimental work performed during my PhD research activity.

References

1. Wilson, A. J. Supramolecular chemistry. *Annu. Reports Prog. Chem. - Sect. B* **104,** 164–183 (2008).
2. Hirst, A. R., Escuder, B., Miravet, J. F. & Smith, D. K. High-tech applications of self-assembling supramolecular nanostructured gel-phase materials: From regenerative medicine to electronic devices. *Angew. Chemie - Int. Ed.* **47,** 8002–8018 (2008).
3. Percec, V., Glodde, M., Bera, T. K., Miura, Y., Shiyanovskaya, I., Singer, K. D., Balagurusamy, V. S. K., Heiney, P. A., Schnell, I., Rapp, A., Spiess, H. W., Hudsonk, S. D. & Duan, H. Self-organization of supramolecular helical dendrimers into complex electronic materials. *Nature* **417,** 384–387 (2002).
4. Daniel, M. C. & Astruc, D. Gold Nanoparticles: Assembly, Supramolecular Chemistry, Quantum-Size-Related Properties, and Applications Toward Biology, Catalysis, and Nanotechnology. *Chem. Rev.* **104,** 293–346 (2004).
5. De Greef, T. F. A. & Meijer, E. W. Supramolecular polymers How do they differ from conventional polymers? *Nature* **453,** (2008).
6. Sanders, J. K. M. Supramolecular photochemistry. *J. Incl. Phenom. Mol. Recognit. Chem.* **13,** 105–106 (1992).
7. Dunitz, J. D. *Thoughts on Crystals as Supermolecules*.
8. Desiraju, G. R. *Crystal Engineering: The Design of Molecular Solid*. (1989).

9. Pepinsky, R. No Title. *Phys. Rev.* **100,** 971–971 (1955).

10. Schmidt, G. M. J. Photodimerization in the solid state. *Pure Appl. Chem.* **27,** 647–678 (1971).

11. Engineering, C. Crystal engineering 1. 1–31 (1989).

12. Sommerer, S. O. Intermolecular Interactions. *Intermol. Interact.* 1–2 (1998). doi:10.1007/978-1-4615-4829-4_1

13. Arunan, E., Desiraju, G. R., Klein, R. A., Sadlej, J., Scheiner, S., Alkorta, I., Clary, D. C., Crabtree, R. H., Dannenber, J. J., Hobza, P., Kjaergaard, H. G., Legon, A. C., Mennucci, B. & Nesbitt, D. J. Definition of the hydrogen bond (IUPAC Recommendations 2011). *Pure Appl. Chem.* **83,** 1637–1641 (2011).

14. Thomas, S. The Hydrogen Bond in the Solid State. *Angew. Chemie Int. Ed.* **41,** 48–76 (2002).

15. Aakeröy, C. B. & Seddon, K. R. The hydrogen bond and crystal engineering. *Chem. Soc. Rev.* **22,** 397–407 (1993).

16. Umeyama, H. & Morokuma, K. The Origin of Hydrogen Bonding. An Energy Decomposition Study. *J. Am. Chem. Soc.* **99,** 1316–1332 (1977).

17. Hildebrand, J. H. & Benesi, H. A. Interaction of iodine with aromatic hydrocarbons [15]. *Nature* **164,** 963 (1949).

18. Metrangolo, P., Meyer, F., Pilati, T., Resnati, G. & Terraneo, G. Halogen bonding in supramolecular chemistry. *Angew. Chemie - Int. Ed.* **47,** 6114–6127 (2008).

19. Metrangolo, P., Neukirch, H., Pilati, T. & Resnati, G. Halogen bonding based recognition processes: A world parallel to hydrogen bonding. *Acc. Chem. Res.* **38,** 386–395 (2005).

20. Stang, P. J. & Olenyuk, B. Accounts Chem Res 1997 Stang Self-assembly symmetry and molecular architecture-502-518. **30,** 17 (1997).

21. Wilmer, C. E., Leaf, M., Lee, C. Y., Farha, O. K., Hauser, B. G., Hupp, J. T. & Snurr, R. Q. Large-scale screening of hypothetical metal-organic frameworks. *Nat. Chem.* **4,** 83–89 (2012).

22. Comments on the paper by S ir John 101. (1950).

23. Desiraju, G. R. & Gavezzotti, A. Crystal structures of polynuclear aromatic hydrocarbons. Classification, rationalization and prediction from molecular structure. *Acta Crystallogr. Sect. B* **45,** 473–482 (1989).

24. Simard, M. & Wuest, J. D. (Oc=Q 4 3. *Society* 4696–4698 (1991).

25. Desiraju, G. R. The Supramolecular Synthon in Crystal Engineering. *Stimul. Concepts Chem.* 293–306 (2005). doi:10.1002/3527605746.ch19

26. Desiraju, G. R. Crystal engineering: A holistic view. *Angew. Chemie - Int. Ed.* **46,** 8342–8356 (2007).

27. Allen, F. H. The Cambridge Structural Database: A quarter of a million crystal structures and rising. *Acta Crystallogr. Sect. B Struct. Sci.* **58,** 380–388 (2002).

28. Macrae, C. F., Bruno, I. J., Chisholm, J. A., Edgington, P. R., McCabe, P., Pidcock, E., Rodriguez-Monge, L., Taylor, R., Van De Streek, J. & Wood, P. A. Mercury CSD 2.0 - New features for the visualization and investigation of crystal structures. *J. Appl. Crystallogr.* **41,** 466–470 (2008).

29. Allen, F. H., Kennard, O. & Taylor, R. Systematic Analysis of Structural Data as a Research Technique in Organic Chemistry. *Acc. Chem. Res.* **16,** 146–153 (1983).

30. Vippagunta, S. R., Brittain, H. G. & Grant, D. J. W. Crystalline solids. *Adv. Drug Deliv. Rev.* **48,** 3–26 (2001).

31. Malek, J. Kinetic analysis of crystallization processes in amorphous materials. *Thermochim. Acta* **355,** 239–253 (2000).

32. Khankari, R. K. & Grant, D. J. W. Pharmaceutical hydrates. *Thermochim. Acta* **248,** 61–79 (1995).

33. Sanphui, P., Goud, N. R., Khandavilli, U. B. R., Bhanoth, S. & Nangia, A. New polymorphs of curcumin. *Chem. Commun.* **47,** 5013–5015 (2011).

34. Psimadas, D., Georgoulias, P., Valotassiou, V. & Loudos, G. Molecular Nanomedicine Towards Cancer : *J. Pharm. Sci.* **101,** 2271–2280 (2012).

35. Adams, C. J., Haddow, M. F., Lusi, M. & Orpen, A. G. Crystal engineering of lattice metrics of perhalometallate salts and MOFs. *Proc. Natl. Acad. Sci. U. S. A.* **107,** 16033–16038 (2010).

36. Paul, M., Chakraborty, S. & Desiraju, G. R. Six-Component Molecular Solids: ABC[D1-(x+y)ExFy]2. *J. Am. Chem. Soc.* **140,** 2309–2315 (2018).

37. Cruz-Cabeza, A. J., Lestari, M. & Lusi, M. Cocrystals Help Break the 'rules' of Isostructurality: Solid Solutions and Polymorphism in the Malic/Tartaric Acid System. *Cryst. Growth Des.* **18,** 855–863 (2018).

38. (a) Bernstein, J. Polymorphism - A perspective. *Cryst. Growth Des.* **11,** 632–650 (2011); (b) Bernstein, J. Polymorphism in Molecular Crystals

39. Mitscherlich. No Title. *Ann. Chim. Phys* **19,** 350 (1822).

40. Liebig, F. Wöhler, J. No Title. *Ann. Pharm. III* **249,** 514 (1832).

41. Price, S. L. Computed crystal energy landscapes for understanding and predicting organic crystal structures and polymorphism. *Acc. Chem. Res.* **42,** 117–126 (2009).

42. Braga, D. & Grepioni, F. Making crystals from crystals: A green route to crystal engineering and polymorphism. *Chem. Commun.* 3635–3645 (2005). doi:10.1039/b504668h

43. McCrone, W. C. *Polymorphism in physics and chemistry of the organic solid-state*. (1965).

44. Gillon, A. L., Feeder, N., Davey, R. J. & Storey, R. Hydration in molecular crystals - A Cambridge Structural Database analysis. *Cryst. Growth Des.* **3,** 663–673 (2003).

45. Infantes, L., Fábián, L. & Motherwell, W. D. S. Organic crystal hydrates: What are the important factors for formation. *CrystEngComm* **9,** 65–71 (2007).

46. Desiraju, G. R. Crystal and co-crystal. *CrystEngComm* **5,** 466–467 (2003).

47. Dunitz, J. D. Crystal and co-crystal: A second opinion. *CrystEngComm* **5,** 506 (2003).

48. Bond, A. D. What is a co-crystal? *CrystEngComm* **9,** 833–834 (2007).

49. Barbour, L. J., Das, D., Jacobs, T., Lloyd, G. O. & Smith, V. J. *Concepts and Nomenclature in Chemical Crystallography*. *Supramol. Chem.* (2012). doi:10.1002/9780470661345.smc108

50. Duggirala, N. K., Perry, M. L., Almarsson, Ö. & Zaworotko, M. J. Pharmaceutical cocrystals: Along

the path to improved medicines. *Chem. Commun.* **52,** 640–655 (2016).

51. Braga, D., Grepioni, F. & Shemchuk, O. Organic-inorganic ionic co-crystals: A new class of multipurpose compounds. *CrystEngComm* **20,** 2212–2220 (2018).
52. Steed, J. W. The role of co-crystals in pharmaceutical design. *Trends Pharmacol. Sci.* **34,** 185–193 (2013).
53. Aakeröy, C. B., Forbes, S. & Desper, J. Using cocrystals to systematically modulate aqueous solubility and melting behavior of an anticancer drug. *J. Am. Chem. Soc.* **131,** 17048–17049 (2009).
54. 157872a0.pdf.
55. Braga, D., Grepioni, F., Maini, L., Prosperi, S., Gobetto, R. & Chierotti, M. R. From unexpected reactions to a new family of ionic co-crystals: The case of barbituric acid with alkali bromides and caesium iodide. *Chem. Commun.* **46,** 7715–7717 (2010).
56. Kelley, S. P., Narita, A., Holbrey, J. D., Green, K. D., Reichert, W. M. & Rogers, R. D. Understanding the effects of ionicity in salts, solvates, co-crystals, ionic co-crystals, and ionic liquids, rather than nomenclature, is critical to understanding their behavior. *Cryst. Growth Des.* **13,** 965–975 (2013).
57. Braga, D., Grepioni, F., Maini, L., Capucci, D., Nanna, S., Wouters, J., Aerts, L. & Quéré, L. Combining piracetam and lithium salts: Ionic co-crystals and co-drugs? *Chem. Commun.* **48,** 8219–8221 (2012).
58. Anastas, P. & Eghbali, N. Green chemistry: Principles and practice. *Chem. Soc. Rev.* **39,** 301–312 (2010).
59. Sheldon, R. A. Green solvents for sustainable organic synthesis: State of the art. *Green Chem.* **7,** 267–278 (2005).
60. Phadtare, S. B. & Shankarling, G. S. Halogenation reactions in biodegradable solvent: Efficient bromination of substituted 1-aminoanthra-9,10-quinone in deep eutectic solvent (choline chloride:urea). *Green Chem.* **12,** 458–462 (2010).
61. Cui, X., Zhang, S., Shi, F., Zhang, Q., Ma, X., Lu, L. & Deng, Y. The influence of the acidity of ionic liquids on catalysis. *ChemSusChem* **3,** 1043–1047 (2010).
62. Leitner, W. Supercritical carbon dioxide as a green reaction medium for catalysis. *Acc. Chem. Res.* **35,** 746–756 (2002).
63. Do, J. L. & Friščić, T. Mechanochemistry: A Force of Synthesis. *ACS Cent. Sci.* **3,** 13–19 (2017).
64. Boldyrev, V. V. J Mat Syn and Proc Volume 8 issue 3-4 2000 V. V. Boldyrev; K. Tkáčová -- Mechanochemistry of Solids- Past, Present, and Prospects.pdf. **8,** (2000).
65. Takacs, L. The historical development of mechanochemistry. *Chem. Soc. Rev.* **42,** 7649–7659 (2013).
66. Julien, P. A., Užarević, K., Katsenis, A. D., Kimber, S. A. J., Wang, T., Farha, O. K., Zhang, Y., Casaban, J., Germann, L. S., Etter, M., Dinnebier, R. E., James, S. L., Halasz, I. & Friščić, T. In Situ Monitoring and Mechanism of the Mechanochemical Formation of a Microporous MOF-74 Framework. *J. Am. Chem. Soc.* **138,** 2929–2932 (2016).

67. Wang, G. W. Mechanochemical organic synthesis. *Chem. Soc. Rev.* **42,** 7668–7700 (2013).

68. Road, S. & Kingdom, U. Mechanochemistry : new and cleaner synthesis. **44,** 0–78

69. Szuppa, T., Stolle, A., Ondruschka, B. & Hopfe, W. Solvent-free dehydrogenation of γ-terpinene in a ball mill: Investigation of reaction parameters. *Green Chem.* **12,** 1288–1294 (2010).

70. Friić, T. New opportunities for materials synthesis using mechanochemistry. *J. Mater. Chem.* **20,** 7599–7605 (2010).

71. Karki, S., Friščić, T., Jones, W. & Motherwell, W. D. S. Screening for pharmaceutical cocrystal hydrates via neat and liquid-assisted grinding. *Mol. Pharm.* **4,** 347–354 (2007).

72. Braga, D., Maini, L. & Grepioni, F. Mechanochemical preparation of co-crystals. *Chem. Soc. Rev.* **42,** 7638–7648 (2013).

73. Shan, N., Toda, F. & Jones, W. Mechanochemistry and co-crystal formation: Effect of solvent on reaction kinetics. *Chem. Commun.* **2,** 2372–2373 (2002).

74. Batzdorf, L., Fischer, F., Wilke, M., Wenzel, K.-J. & Emmerling, F. Direct In Situ Investigation of Milling Reactions Using Combined X-ray Diffraction and Raman Spectroscopy. *Angew. Chemie* **127,** 1819–1822 (2015).

75. Klimakow, M., Klobes, P., Thünemann, A. F., Rademann, K. & Emmerling, F. Mechanochemical synthesis of metal-organic frameworks: A fast and facile approach toward quantitative yields and high specific surface areas. *Chem. Mater.* **22,** 5216–5221 (2010).

76. Casali, L., Mazzei, L., Shemchuk, O., Honer, K., Grepioni, F., Ciurli, S., Braga, D. & Baltrusaitis, J. Smart urea ionic co-crystals with enhanced urease inhibition activity for improved nitrogen cycle management. *Chem. Commun.* **54,** (2018).

77. Casali, L., Mazzei, L., Shemchuk, O., Sharma, L., Honer, K., Grepioni, F., Ciurli, S., Braga, D. & Baltrusaitis, J. Novel Dual-Action Plant Fertilizer and Urease Inhibitor: Urea·Catechol Cocrystal. Characterization and Environmental Reactivity. *ACS Sustain. Chem. Eng.* **7,** 2852–2859 (2019).

78. Mazzei, L., Broll, V., Casali, L., Silva, M., Braga, D., Grepioni, F., Baltrusaitis, J. & Ciurli, S. Multifunctional urea cocrystal with combined ureolysis and nitrification inhibiting capabilities for enhanced nitrogen management. *ACS Sustain. Chem. Eng.* **7,** 13369–13378 (2019).

79. D'Agostino, S., Azzali, A., Casali, L., Taddei, P. & Grepioni, F. Environmentally Friendly Sunscreens: Mechanochemical Synthesis and Characterization of β-CD Inclusion Complexes of Avobenzone and Octinoxate with Improved Photostability. *ACS Sustain. Chem. Eng.* **8,** (2020).

85. Shemchuk, O., Braga, D. & Grepioni, F. Ionic Cocrystals of Levodopa and Its Biological Precursors l-Tyrosine and l-Phenylalanine with LiCl. Cryst. Growth Des. 19, 6560–6565 (2019).

CHAPTER 2

CRYSTALLINE MATERIALS OF AGROCHEMICAL INTEREST

PART I

UREA CO-CRYSTALS

2.1 The journey of urea: from industrial production to applications

In recent years there has been a growing interest in environmental issues, such as global warming and other human-driven changes to the environment, which raise concerns about the future livability of the Earth.[1] With the #FridaysForFuture initiative promoted by the Swedish activist Greta Thunberg, over than 1.6 million people around the globe mobilized last year to defend the environment from climate change and plastic pollution, giving rise to an historical breakthrough in environmental activism.[2] Political action is also being taken in this direction, with several countries committed to align national policies with the 2030 Agenda for Sustainable Development, a program of 17 goals signed by the governments of the 193 UN member states in September 2015.[3] These actions arise in response to the tangible environmental problems caused by the modern society, whose irreversible consequences have been stressed for decades by scientists.[4]

We live today in what the scientific community defines as Anthropocene, an age characterized by the territorial, structural and climatic changes due to the human activity.[5] Various start dates for the Anthropocene have been proposed, ranging from the Industrial Revolution in the 19th century to the Great Acceleration after World War II,[6] period characterized by one of the most important invention of the 20th century - the Haber-Bosch process for the synthesis of ammonia (NH_3).[7]

The Haber-Bosch process enables to produce an endless source of reactive nitrogen through the fixation of the atmospheric nitrogen (N_2), obtaining in this way a constant availability of nitrogen for plants nutrition and, consequently, food production. Therefore, it can be deduced the importance of such process during the population boom of the 1950s, since it allowed ensured food supply, as well as the growth of food factories and the diffusion of vast monocultures.[8] However, this unprecedented and unbounded use of nitrogen has irreversibly damaged its natural cycle, with several harmful effects on the environment such as pollution and eutrophication.[9] Moreover, the synthesis of NH_3 occurs via hydrogenation of N_2 using H_2 derived from natural gas, through a process that consumes ~1% of the global energy and ~4% of the total natural gas supply.[10] In view of these negative effects related to the Haber-Bosch process, the research is aimed toward the optimization of such process,[11] which is still central to the fertilizers industry.

By the reaction of ammonia with carbon dioxide, urea - the nitrogen-based fertilizer most commonly used – is obtained.[12] However, because of the activity of several enzymes contained in the soil, especially urease[13] and AMO,[14] the fertilizing capacity of urea is strongly compromised, this fact giving rise to serious agronomic, environmental and economic problems. Once urea is deposited in the soil, it quickly undergoes several reactions, which interfere with the nitrogen cycle, thus exacerbating the greenhouse effect (Fig.1).

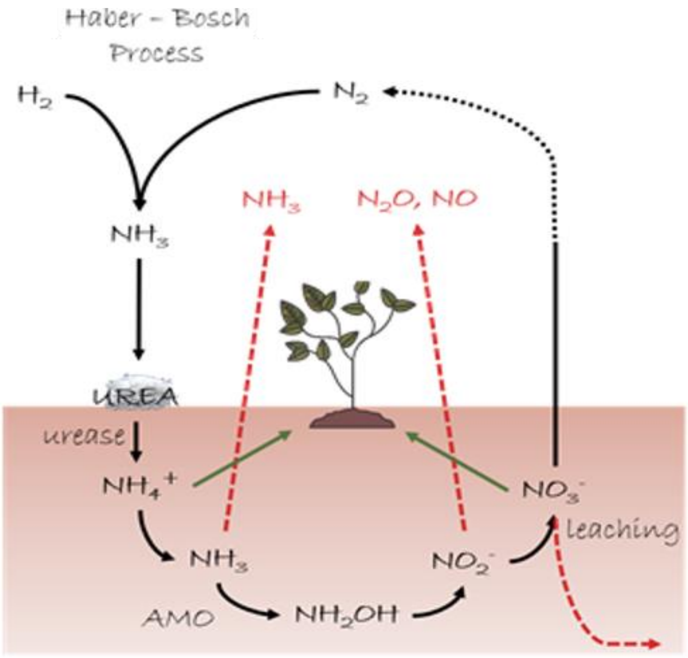

*Fig.1***.** Schematic representation of the N cycle (black arrows). Loss pathways of the reactive N are shown with red arrows, while green arrows indicate the N species available for plants.

From ammonia production to the actual use of urea, it was found that the processes behind the agricultural field are environmentally hazardous. Since it has been estimated that the world population will reach 9 billion by the year 2050, with a concomitant expansion in global agricultural production of about 70−100% [15] and an annual production of urea projected to reach 226 million tons only in 2021,[16] decisive actions in favor of a sustainable agriculture are needed.[17] The second objective of the UN program states to *end hunger, achieve food security, improve nutrition and promote sustainable agriculture*.[18] In order to pursue these goals, different approaches have been followed, ranging from the development of new cultivation methods, such as vertical farming,[19] to an improvement of the actual urea-based fertilizers.

In the last few years, the traditional nitrogen fertilizers have been replaced with new formulations based on urea and substances able to improve the effectiveness of urea itself. The importance of these new formulations is stressed in a recent regulation of the European Union:

"*Certain products are being used in combination with fertilisers for the purpose of improving nutrition efficiency, with the beneficial effect of reducing the amount of fertilisers used and hence their environmental impact. In order to facilitate their free movement on the internal market, not only fertilisers, i.e. products intended to provide plants with nutrient, but also products intended to improve plants' nutrition efficiency, should be covered by the harmonisation"* (June 2019).[20] This regulation is extremely important because, by placing the fertilizer and such substances on an equal legal and commercial level, it not only legitimizes the use of these substances but it also aims to equalize their use to that of the fertilizers.

These substances can improve the stability of urea in moist soils by acting substantially in two ways, either by limiting the dissolution rate/water solubility of urea or by inhibiting the activity of the enzymes in the soil, mainly urease and AMO. The first approach is essentially based on the coating[21] or encapsulation[22] of urea granules. The second approach consists in the improvement of urea-based fertilizers via addition of inhibitors, which are typically applied via liquid formulation with N containing liquid fertilizers, such as urea-ammonium nitrate (UAN) solution, or sprayed onto solid urea granules.

The aim of this research project is the design and development of innovative materials, capable to reconcile both the above-mentioned aspects, i.e. improve the chemical-physical properties of urea - by reducing its water solubility/dissolution rate - and manifest an inhibition activity towards the enzymes urease and/or AMO.

To this end, crystal engineering represents a powerful tool for the design of such systems. Through the solid-state modification of urea, it is in fact possible to obtain urea-based co-crystals, which perfectly fulfill the dual purpose of this research project, as will be shown in the next chapters.

2.2 Urea co-crystals

Urea, $CO(NH_2)$, is a molecule of primary interest in chemical practice and industry: besides its fertilizing activity, urea plays a major role also in pharmaceutical, cosmetic and technological fields.[23]

Given the key-role of such molecule in these primary sectors, the behavior of urea has been extensively investigated by crystal engineering scientists,[24] for a better understanding of its solid-state molecular self-assembly. Such investigation resulted in a huge implementation of urea-based crystalline structures such as co-crystals,[25] salts[26,27] and clathrates:[28] the CSD database gathers 768 crystalline structures to the present day (December 2020).

In pure crystalline urea two NH protons act as hydrogen bond donors towards the O atom [N-H···O 2.977 Å], thus resulting in the formation of a robust one-dimensional hydrogen-bonded chain (Fig.2a).[29] The NH hydrogens not involved in the bifurcated interactions play a bridging function, by bonding the near perpendicular chains [N-H···O 2.051 Å]: the overall crystal packing results in a channel-like structure (Fig.2b).

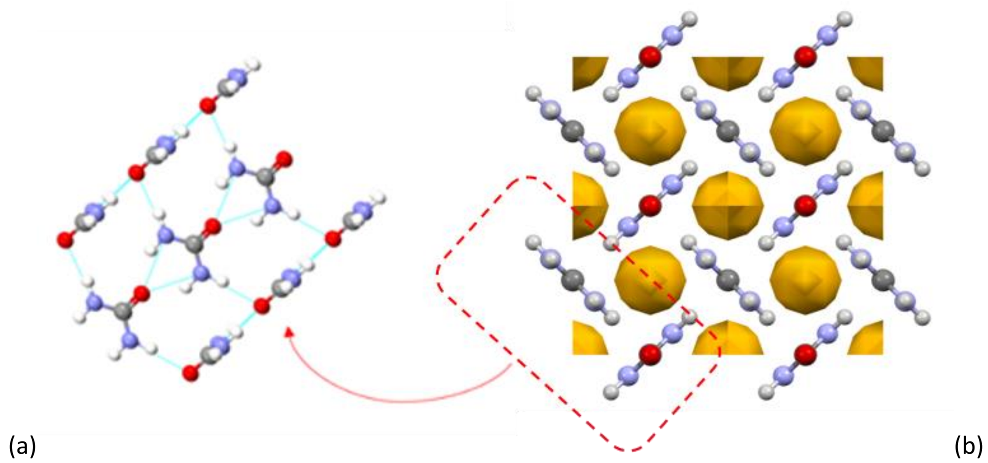

*Fig.2***.** Main crystalline packing of (a) urea and (b) its crystal arrangement along *c*-axis.

Given the voids (in yellow in Fig.2b) arising from such crystal arrangement, the urea structure is quite susceptible to high pressure, which causes channel voids collapsing and N-H···O hydrogen bonds being broken (and differently restored).[30] As shown in Fig.3, the high-pressure condition can induce the conversion of the main form of urea - referred as phase I ($P4\text{-}2_1m$) - into the form phase III ($P2_12_12_1$) or phase IV ($P2_12_12$), depending on the experimental conditions.[31] To the present day, these are the only known polymorphs of urea, with phase I being the crystalline form we routinely deal with.

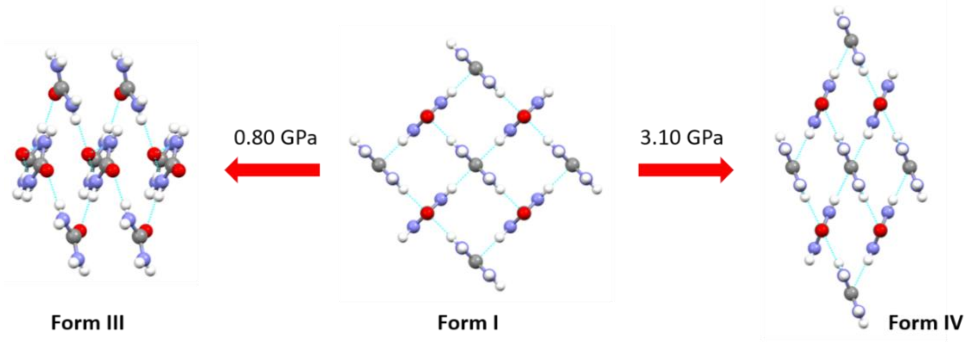

*Fig.3***.** urea polymorphs at different pressures.

Interestingly, none of the hydrogen bonds contained in phases I, III and IV are of the type most frequently encountered in urea co-crystals. By running the ‘motif search’ module on the program Mercury,[32] it was found out that ca 42% of the urea-containing structures in CSD database rely on a homosynthon-based dimer: the O atom acts as hydrogen bond acceptor towards one of the N-H group on a complementary urea molecule (Fig.4).

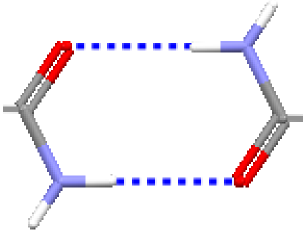

Fig.4. urea main motif in co-crystals: homosynthon-based dimer.

With such crystal arrangement, the interaction of urea with other components can be dramatically expanded: the oxygen can act as hydrogen bond acceptor or as a partner of a cation-dipole interaction (just one lone pair on the O is involved in the dimer) while the free NH protons can bond neutral and ionic hydrogen bond acceptors. It follows that urea is an extremely versatile compound to co-crystallize with several kind of co-formers, both neutral and ionic.

For strategic co-crystal preparation, the CSD database can play a key-role in the design of a co-crystallization experiment, helping in making assumptions about the crystal arrangement of a potential co-crystal. Given the starting materials, it is in fact possible to perform a statistical analysis on the structures containing such materials - or similar ones - thus getting a first clue about a possible outcome of the co-crystallization.

In this research project urea has been co-crystallized with co-formers of agrochemical interest, mainly through mechanochemical methods. Given the novelty of the topic, our first attempt concerned the synthesis and characterization of a binary co-crystal based on urea and a urease inhibitor. The second step consisted in a development of such system through the inclusion of soil nutrients, thus resulting in a ternary co-crystal. Finally, the last system successfully synthesized was still a ternary co-crystal, but with an AMO inhibitor as a co-former.

In the next paragraphs, each system will be presented in detail: an overview about the corresponding agrochemical part will be followed by the link to the published manuscript and the experimental data from the supporting information.

2.3 Urease and urease inhibitors

Urease is a nickel-dependent enzyme which can be found in plants, algae, fungi as well as in the soil, where it operates within the global nitrogen cycle.

Once urea is dissolved in the soil, it is hydrolyzed into hydrogen carbonate (HCO_3^-) and ammonium (NH_4^+), at a rate 10^{15} times faster than in the non-catalyzed reaction (Scheme 1).[33] The rapid pH increase upon urea hydrolysis causes the loss of the unassimilated ammonium as gaseous NH_3, which is then released to the atmosphere, thus exacerbating the greenhouse effect and contributing to the formation of fine inorganic particulate matter (PM 2.5).[34,35,36]

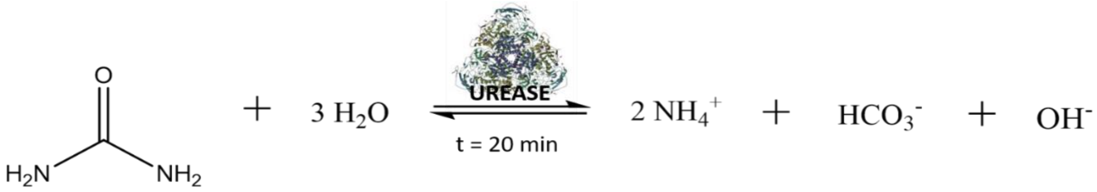

Scheme 1: Overall urea hydrolysis catalyzed by urease.

Apart from being an object of agrochemical interest, urease is a key enzyme in the medical field, since it is the main virulence factor of many human pathogens, such as Helicobacter Pylori,[37] a bacterium usually found in the stomach of people with chronic gastritis and gastric ulcers.

Given the fact that a control on urease activity would be extremely important for environmental and medical applications, the scientific research has been oriented for decades in the understanding of the hydrolysis mechanism.

Urease holds a record in the field of biological chemistry since it was the first enzyme ever crystallized and proven to be proteinaceous,[38] the discovery paving the way for a better understanding of enzymatic structures. Additional studies, performed using both crystallographic techniques and X-ray absorption spectroscopy, revealed then the native structure of urease, which was found to be a nickel-dependent enzyme.[39] The active site is based on two Ni^{2+} spaced 3.5 Å with a bridging hydroxide, with Ni1 coordinatively unsaturated, Ni2 in an octahedral coordination and both the Ni cations bound to a water molecule (Fig.5).

The acquired knowledge on the urease structure was instrumental in the understanding of the catalytic mechanism and, consequently, the development of new and efficient chemicals able to inhibit urease.

Over the last 40 years several mechanisms have been proposed, but all agreed on the first step, whereby urea binds to the unsaturated nickel through its oxygen.[40] As a result, it was found out that urease inhibition could be activated by chemicals that target the nickel ion and prevent urea from entering the active site. Such chemicals fall into the category of reversible inhibitors, which comprises phosphates, diamidophosphates, thiols, sulfites, fluorides, as well as hydroxamic, citric and boric acids.

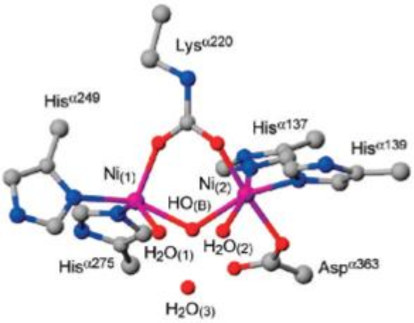

Fig.5: schematic representation of the urease active site (ref.37)

Concerning the second catalytic step, urea undergoes a nucleophilic attack through a process for which three main mechanisms have been proposed (Fig.6). According to the first hypothesis, water bound to Ni2 acts as a nucleophile towards the carbon atom of urea, which is coordinated to Ni1 in a monodentate mode.[41] The second hypothesis holds urea in the monodentate coordination mode, but proposes the OH bridge as a nucleophile.[42–44] Finally, the last hypothesis - which was proven to be the effective one - preserves the OH bridge as a nucleophile, but states that both Ni^{2+} cations are involved in the coordination of urea.[45]

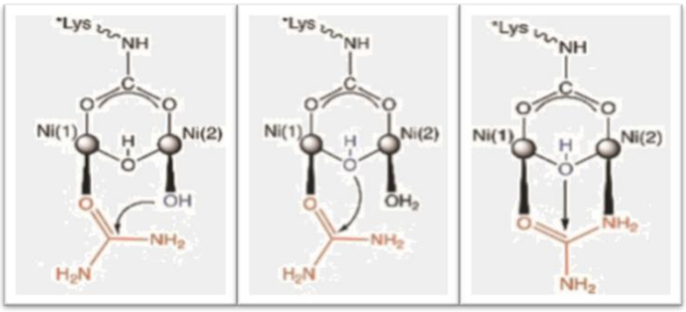

Fig.6: comparison between the different nucleophilic attacks: water (left), OH monodentate (middle), OH bidentate (right).

The mechanism concerning this last step is elucidated in Scheme 2: the bidentate mode is assisted by a mobile flap, whose histidine residue - marked in red - drives the entrance of the substrate into the active site cavity along with the flap closure. The comprehension of this catalytic step paved the way for a novel class of inhibitors, such as catechols and quinones, which act by blocking irreversibly the flap in an open conformation, so that it is no longer able to assist the urea coordination.[46]

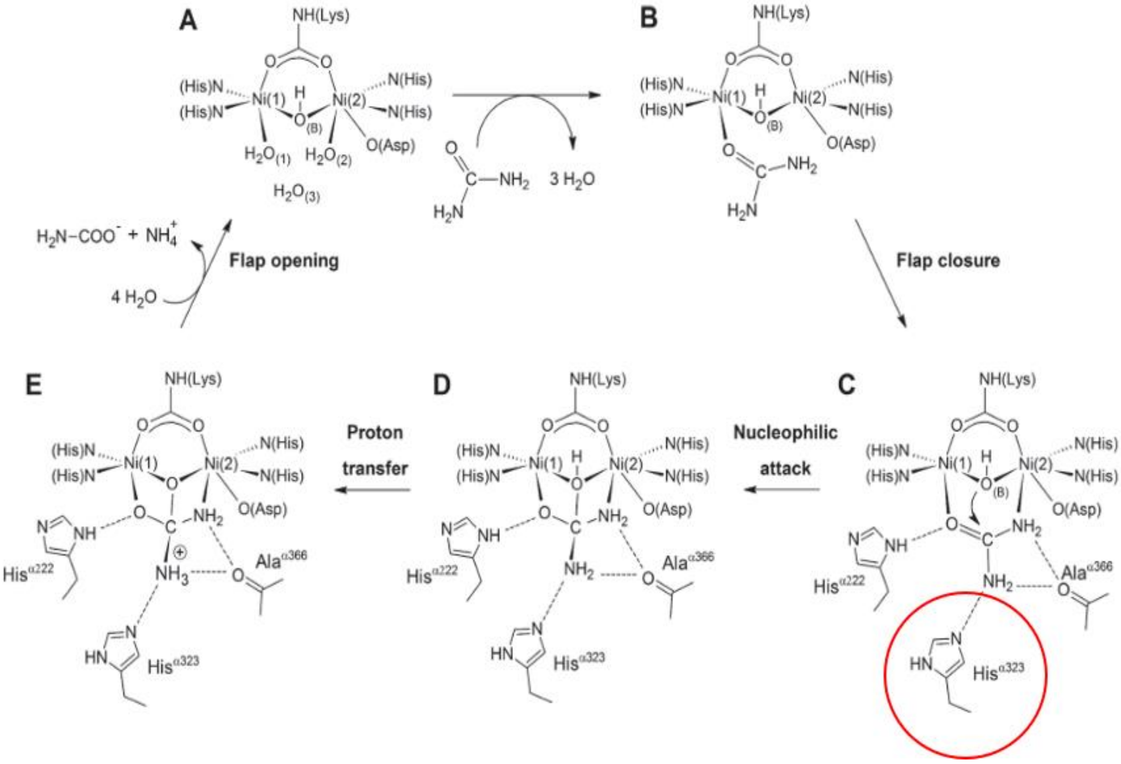

Scheme 2: mechanism of urea hydrolysis (ref.40)

The first attempt at urea co-crystallization was performed with these inhibitors. Since the molecular details of the irreversible inactivation have been recently elucidated,[47] the use of such compounds for agrochemical applications is quite recent, thus the designed co-crystals are even more pioneering fertilizers.

After multiple attempts, catechol was found to be a good co-former (Fig.6). The successful outcome of the crystallization process met the expectations: according to crystal engineering principles, the complementarity between the hydroxyl groups on catechol and the carbonyl groups on urea is likely to provide a strong hydrogen bonded network.

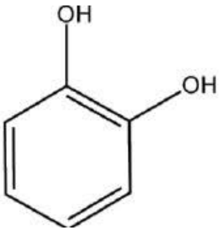

Fig.6: scheme of catechol.

2.3.1. URCAT

The urea-catechol co-crystal - URCAT (Fig7) - was succesfully synthesized through the mechanochemical method (crystalline powder) and from a EtOH solution of the reagents (single crystals).

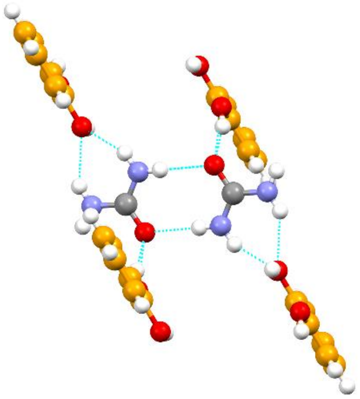

Fig.7: crystalline motif of URCAT.

The methods and techniques used for the characterization of the solid-state product were the following:

- Single Crystal X-ray Diffraction (SCXRD) for structure determination.
- X-ray Powder Diffraction (XRPD) to determine whether the change of the phase took place, i.e. wheter there were new peaks different from those of the starting materials.
- Differential Scanning Calorimetry (DSC) for the detection of eventual phase changes (dehydration/desolvation, polymorphic transition, melting).
- Thermogravimetric Analysis (TGA) to estimate the mass loss of the sample.

- Solubility test to determine the maximum quantity of urea in URCAT capable of dissolving in a given amount of water.
- Stability test to compare the stability of the co-crystal and of the physical mixture of the reagents in a chamber at controlled humidity.

The tests on the inhibition activity towards urease were performed by the research group of prof. Stefano Ciurli.

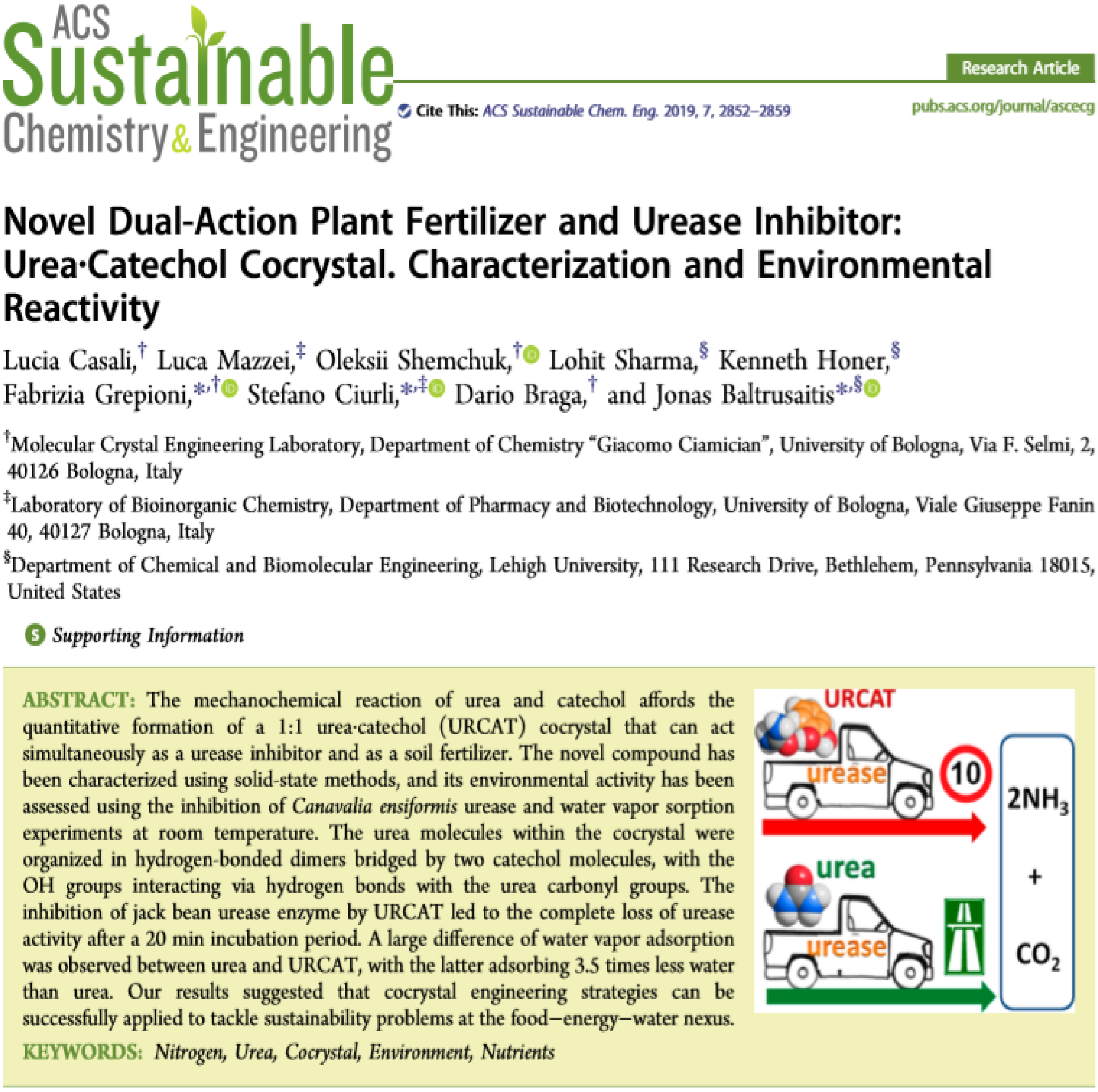

ACS Sustainable Chemistry & Engineering

Research Article

Cite This: ACS Sustainable Chem. Eng. 2019, 7, 2852−2859

pubs.acs.org/journal/ascecg

Novel Dual-Action Plant Fertilizer and Urease Inhibitor: Urea·Catechol Cocrystal. Characterization and Environmental Reactivity

Lucia Casali,[†] Luca Mazzei,[‡] Oleksii Shemchuk,[†] Lohit Sharma,[§] Kenneth Honer,[§] Fabrizia Grepioni,*[,†] Stefano Ciurli,*[,‡] Dario Braga,[†] and Jonas Baltrusaitis*[,§]

[†]Molecular Crystal Engineering Laboratory, Department of Chemistry “Giacomo Ciamician”, University of Bologna, Via F. Selmi, 2, 40126 Bologna, Italy

[‡]Laboratory of Bioinorganic Chemistry, Department of Pharmacy and Biotechnology, University of Bologna, Viale Giuseppe Fanin 40, 40127 Bologna, Italy

[§]Department of Chemical and Biomolecular Engineering, Lehigh University, 111 Research Drive, Bethlehem, Pennsylvania 18015, United States

Supporting Information

ABSTRACT: The mechanochemical reaction of urea and catechol affords the quantitative formation of a 1:1 urea·catechol (URCAT) cocrystal that can act simultaneously as a urease inhibitor and as a soil fertilizer. The novel compound has been characterized using solid-state methods, and its environmental activity has been assessed using the inhibition of *Canavalia ensiformis* urease and water vapor sorption experiments at room temperature. The urea molecules within the cocrystal were organized in hydrogen-bonded dimers bridged by two catechol molecules, with the OH groups interacting via hydrogen bonds with the urea carbonyl groups. The inhibition of jack bean urease enzyme by URCAT led to the complete loss of urease activity after a 20 min incubation period. A large difference of water vapor adsorption was observed between urea and URCAT, with the latter adsorbing 3.5 times less water than urea. Our results suggested that cocrystal engineering strategies can be successfully applied to tackle sustainability problems at the food−energy−water nexus.

KEYWORDS: *Nitrogen, Urea, Cocrystal, Environment, Nutrients*

For copyright reasons only the link to the original article is reported here:

https://doi.org/10.1021/acssuschemeng.8b06293

2.3.2. Supporting Information

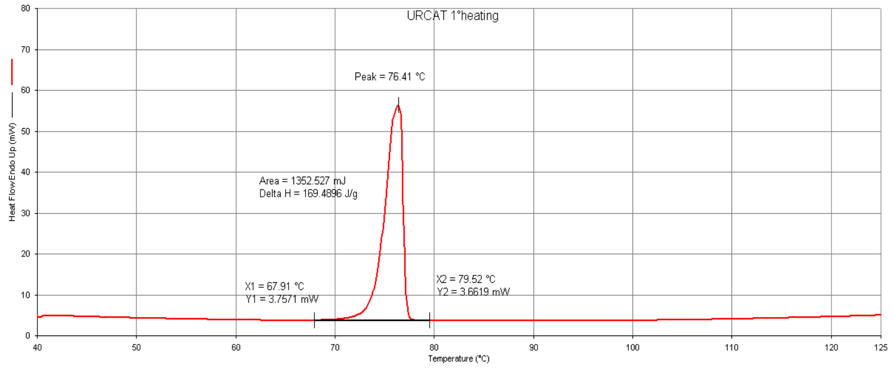

Fig. SI-1: DSC trace for URCAT (1st heating).

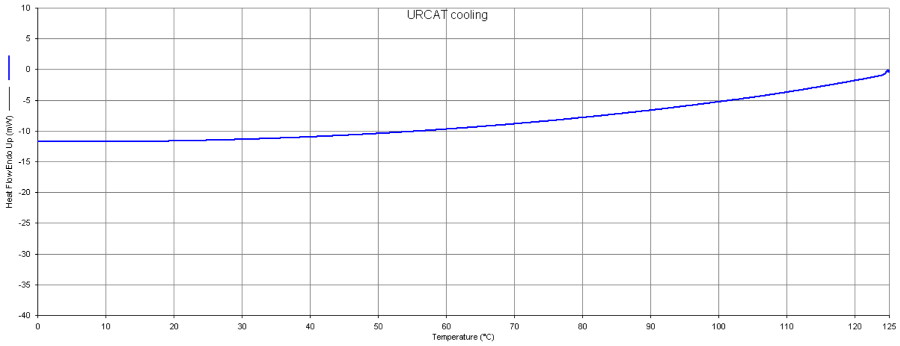

Fig. SI-2: DSC trace for the urea·catechol co-crystal (URCAT, 1st cooling).

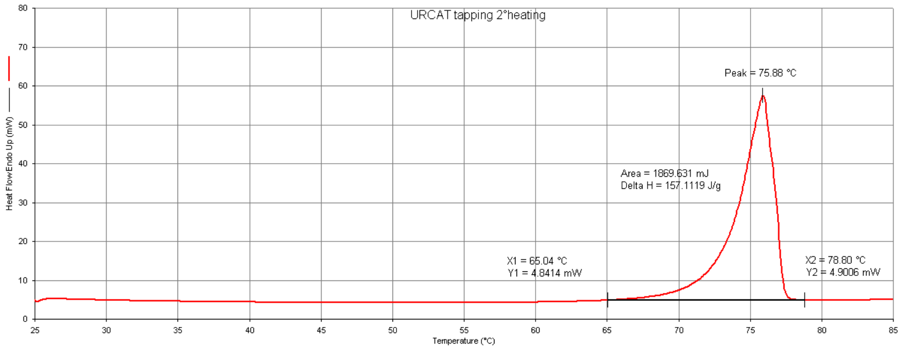

Fig. SI-3: DSC trace for URCAT (2nd heating). The melting point corresponds to the one observed for URCAT.

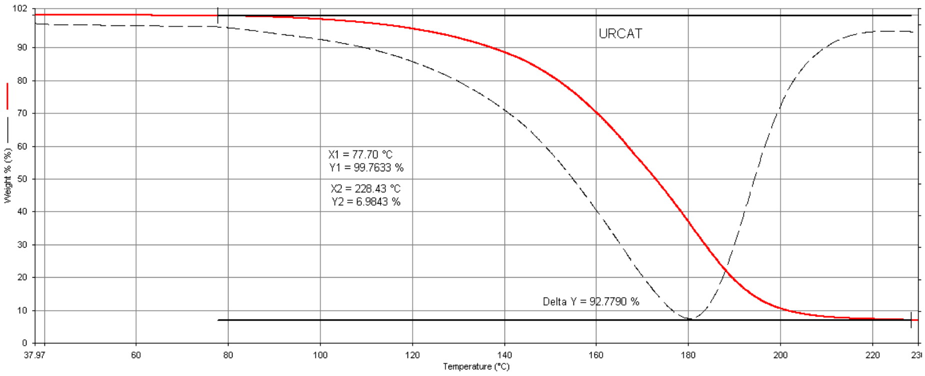

Fig.SI-4: TGA trace for URCAT.

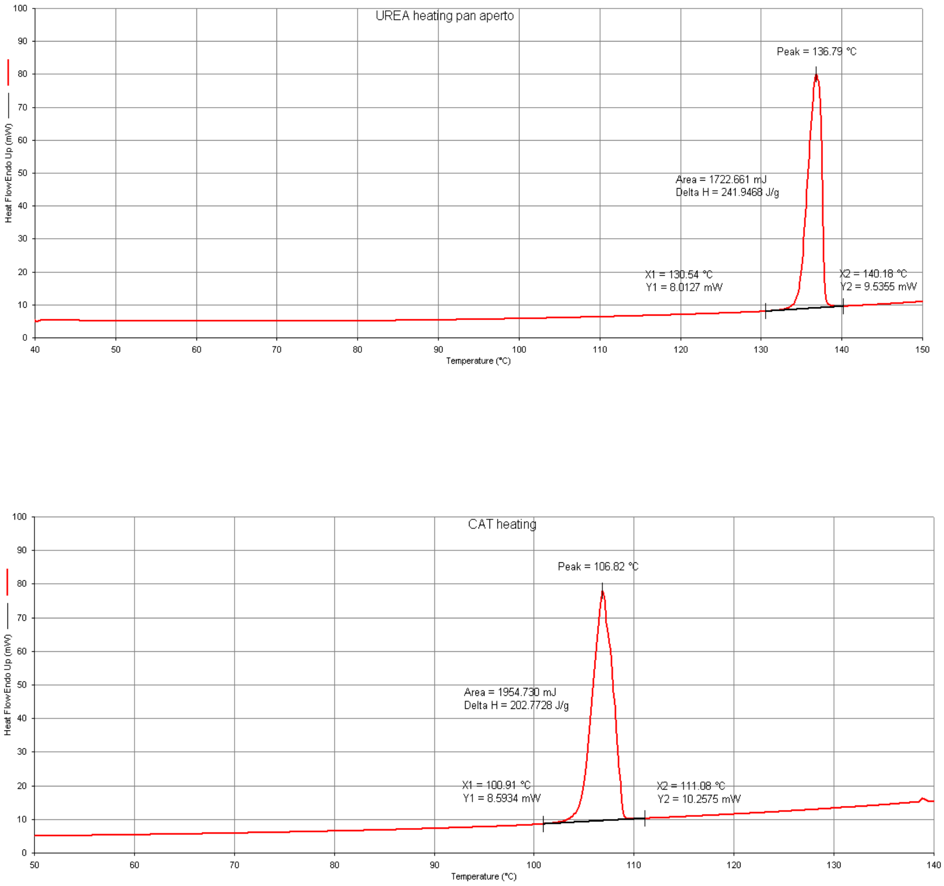

Fig. SI-5: DSC traces for urea (top) and catechol (bottom) used for the synthesis of URCAT.

Table SI-1. Crystal data and details of measurement for URCAT.

Chemical formula	$CH_4N_2O \cdot C_6H_6O_2$
M_r, g mol^{-1}	170.17
T / K	293 (2)
Morphology, colour	Plate, colourless
Crystal system	Monoclinic
Space group	$P2_1/c$
a / Å	7.1751 (4)
b / Å	6.2509 (4)
c / Å	19.2212 (16)
α / °	90
β / °	97.888 (7)
γ / °	90
V / Å^3	853.93 (10)
Z	4
d / g cm^{-3}	1.324
μ / mm^{-1}	0.11
Measd reflns	3897
Indep reflns	1976
Reflns with I > 2σ(I)	1255
R_{int}	0.028
$R [F^2 > 2\sigma(F^2)]$	0.062
$wR (F^2)$	0.182

Crystal data can be obtained free of charge from the Cambridge Crystallographic Data Centre via https://www.ccdc.cam.ac.uk and have been allocated the accession number CCDC 1880413.

2.4 Beyond nitrogen: the role of several elements in plant nutrition

Nitrogen-based fertilizers are the most used fertilizers, especially with regard to urea. Along with nitrogen, also potassium and phosphorus play a pivotal role in the nutrition of the plants:[48] these are the three main nutrients for the plants - hence the NPK fertilizers[49] - and fall into the category of macronutrients.

Phosphorous based fertilizers origin from mined ore, which is converted into a water-soluble salt thanks to a chemical extraction with an acid.[50] Potassium based fertilizers, instead, rely on potash (physical mixture of potassium salts) extracted from mined rock. Since potash is water-soluble, the production method is mainly based on a purification process of the potassium rocks.[51] Overall, the production of such fertilizers is less energy demanding compared to the nitrogen-based ones and the dependence on natural gas is definitely lower.

Depending on factors such as crop types, soil characteristics and climatic conditions, the application of NPK fertilizers can vary from country to country, resulting that Asia agriculture is strongly nitrogen-based while South America is mainly potassium and phosphorous dependent.[52] Nitrogen-based fertilizers still represent more than 2/3 of the total use of NPK fertilizers, but the use of potassium and phosphorous fertilizers is increasing at global level on an annual basis by around 2%.[53,54]

In addition to macronutrients, other elements are essential to the plants in small concentrations, i.e. the micronutrients - such as iron (Fe), manganese (Mn), zinc (Zn), copper (Cu), boron (B), molybdenum (Mo), chloride (Cl) and nickel (Ni) -[55] which have to be delivered with fertilizers. Micronutrient deficiencies affect plant growth by impairing physiological processes related to seed formation, synthesis of carbohydrates, biological N fixation and resistance to biotic and abiotic diseases. Moreover, the lack of micronutrients leads to a less efficient use of other essential plant nutrients, resulting in greater nitrogen losses to the environment, and reduces the plant’s ability to absorb water.[56]

Micronutrient deficiencies in soils and plants were also found to directly cause micronutrient deficiencies in humans, with awful consequences for human health. More than 2 billion people suffer from micronutrient malnutrition, sometimes referred to as “hidden hunger”:[57] according to a report of the World Health Organization on the risk factors responsible for the development of illnesses and diseases, Zn and Fe deficiencies rank 5th and 6th among the 10 most important factors in low-income countries.[58] Given the importance of the problem, it has been introduced the agronomic biofortification,[59,60] i.e. the enrichment of food crops with micronutrient, aimed to minimize the extent of micronutrient deficiencies.

A further improvement in the formulation of urea-based co-crystals was then pursued by inclusion of the above-mentioned elements. Among the micronutrients, zinc is also an irreversible inhibitor towards the enzyme urease,[61] thus contributing to the reduction of the greenhouse effect and all the urea-use related problems.

In the CSD database there are currently more than 300 organic-inorganic urea-based structures, as proof that urea is a well-suited building block for the ionic co-crystallization: the oxygen atom is generally involved in ion-dipole interactions with cations while the NH_2 groups point towards anions.

2.4.1. ZnKU

Urea was successfully co-crystallized with $ZnCl_2$ and KCl, with formation of $K[Zn(urea)Cl_3]$ (ZnKU). Interestingly, the presence of Zn is instrumental in the inclusion of the K^+ cation in the crystalline edifice, resulting in one of the few structures in the CSD database involving both urea and potassium.[62]

Two different crystalline forms in a monotropic relationship were obtained, but all the analyses were performed on the thermodynamically stable form (Fig.8), which was prepared via all the main crystallization methods – mechanochemistry, slurry and precipitation, from a water solution of the reagents, at room temperature.

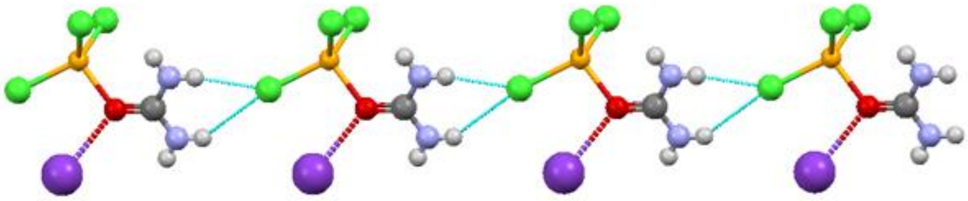

Fig.8: crystalline motif of ZnKU.

The methods and techniques used for the characterization of the solid-state products were the following:

- Single Crystal X-ray Diffraction (SCXRD) for structure determination.
- X-ray Powder Diffraction (XRPD) to determine whether the change of the phase took place, i.e. wheter there were new peaks different from those of the starting materials.

- Differential Scanning Calorimetry (DSC) for the detection of phase changes (dehydration/desolvation, polymorphic transition, melting) and for the assesment of the polymorphic relationship between the two forms.
- Thermogravimetric Analysis (TGA) to estimate the mass loss of the sample.
- Solubility test. This technique was used to determine the maximum quantity of urea in ZnKU capable of dissolving in a given amount of water.
- Stability test. This technique was emplyed to evaluate the stability of ZnKU with respect to a physical mixture of the reagents in a chamber at controlled humidity.

Also in this case, the inhibition of the enzymatic activity of urease was tested in the research group of prof. Stefano Ciurli.

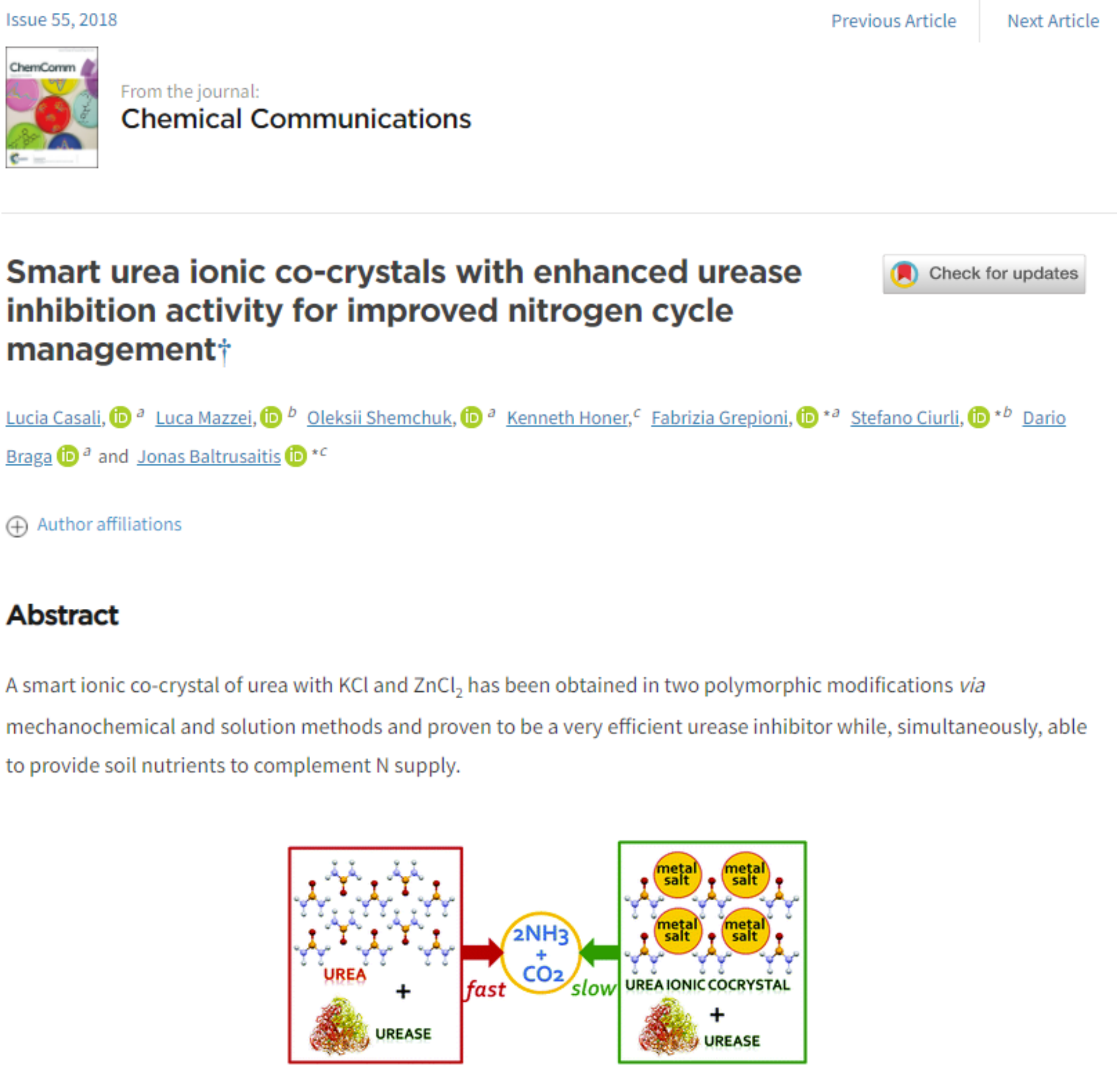

Issue 55, 2018

Previous Article | Next Article

From the journal:
Chemical Communications

Smart urea ionic co-crystals with enhanced urease inhibition activity for improved nitrogen cycle management†

Check for updates

Lucia Casali, [a] Luca Mazzei, [b] Oleksii Shemchuk, [a] Kenneth Honer, [c] Fabrizia Grepioni, *[a] Stefano Ciurli, *[b] Dario Braga [a] and Jonas Baltrusaitis *[c]

Author affiliations

Abstract

A smart ionic co-crystal of urea with KCl and $ZnCl_2$ has been obtained in two polymorphic modifications *via* mechanochemical and solution methods and proven to be a very efficient urease inhibitor while, simultaneously, able to provide soil nutrients to complement N supply.

For copyright reasons only the link to the original article is reported here:

https://doi.org/10.1039/C8CC03777A

2.4.2 Supporting Information

Experimental Procedures

All reagents were purchased from Sigma-Aldrich or Alfa Aesar and used without further purification.

Solution Synthesis. Equimolar quantities of the starting materials (urea, $ZnCl_2$ and KCl) were dissolved in 5 mL of water at room temperature. The solution was divided in two portions: metastable form 1 was obtained by heating the solution to 80°C and leaving the solvent to evaporate at this temperature, while stable form 2 was obtained by slow solvent evaporation at room temperature.

Solid state synthesis. Pure form 2 was obtained by ball-milling urea (1 mmol) with $ZnCl_2$ (1 mmol) and KCl (1 mmol) in an agate jar for 60 min in dry conditions or with the addition of a drop of water. Form 2 was also obtained during pellets preparation of form 1, i.e. under hydrostatic pressure.

Slurry. Slurry experiments were performed in water at room temperature for 10 days. Form 2 appeared to be the only stable phase in the suspension, regardless of the of Urea:$ZnCl_2$:KCl stoichiometric ratio (1:1:1, 1:1:2 and 2:1:1) or the initial presence of only pure form 1.

Solubility tests. A qualitative analysis was performed for urea and ZnKU as described in the following. Solubility of urea at room temperature ranges from 1 to 1.2 g mL^{-1},[63] therefore a control experiment was conducted in which 1 g of urea was added to a vial and dissolved in 1mL of bidistilled water. In a second vial an amount of ZnKU form 2 (4.5 g) containing 1 g of urea and 1 mL of bidistilled water were then added: the dissolution was not complete, as can be seen in Figure ESI-1a.

The solid not dissolved was filtered and weighed, resulting in ca. 900 mg of powder material, which corresponds to a reduction in the solubility of urea in ZnKU with respect to pure urea of ca. 20%. The undissolved powder was analyzed via X-ray powder diffraction (see below in the X-ray powder diffraction section) and found to be ZnKU form 2. The experiment was repeated three times and, in all cases, the same behavior and amount of undissolved substance was observed. In a fourth experiment, the addition of 1 mL of bidistilled water to the vial containing the undissolved form 2 caused complete dissolution of the solid residue (see Figure ESI-1b).

Thermogravimetric analysis. TGA measurements were performed with a PerkinElmer TGA7 in the temperature range 30-300 ºC and 30-450°C for urea and ZnKU, respectively, under N_2 gas flow at a heating rate of 5.00 ºC min^{-1}.

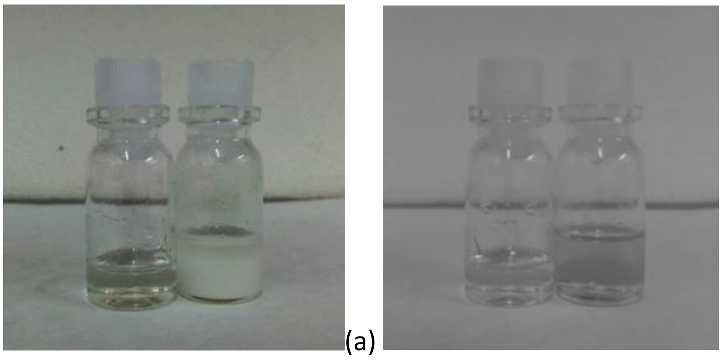

(a) (b)

Fig. ESI-1. Dissolution of the same quantity (1g) of urea as pure substance (left vial) and in ZnKU (right vial), added to 1 (a) and 2 (b) mL of water.

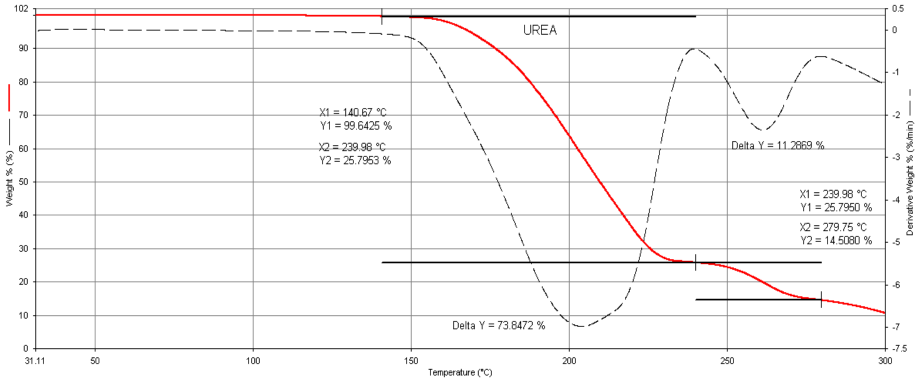

Fig. ESI-2. TGA trace for the solid urea used in all experiments.

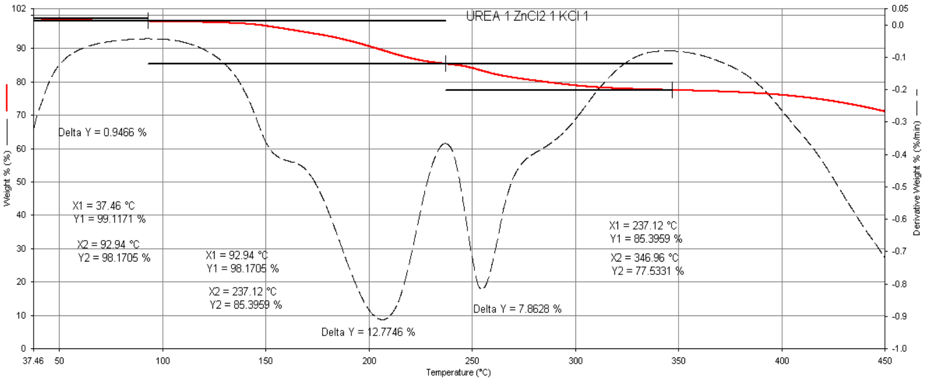

Fig. ESI-3. TGA trace for ZnKU form 1.

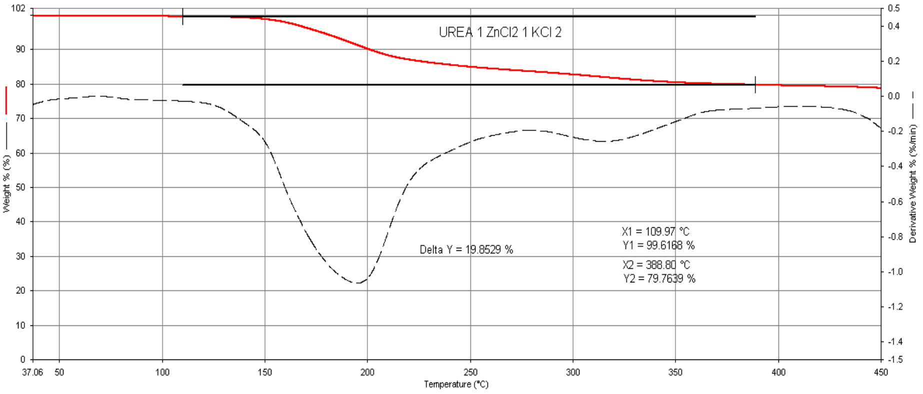

Fig. ESI-4. TGA trace for ZnKU form 2.

Differential Scanning Calorimetry. DSC traces were recorded using a Perkin-Elmer Diamond. The samples (1-3 mg range) were placed in open Al-pans. All measurements were conducted in the ranges 40-150/160/170 °C (for urea, ZnKU form 1 and ZnKU form 2, respectively), at a heating rate of 5ºC min^{-1}. Melting points for urea, ZnKU form 1 and ZnKU form 2 are 137, 135 and 142 °C, respectively (peak temperatures).

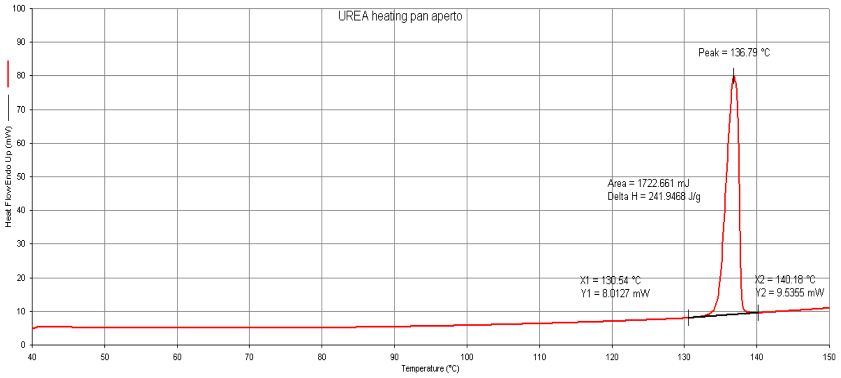

Fig. ESI-5. DSC trace for the solid urea used in all experiments.

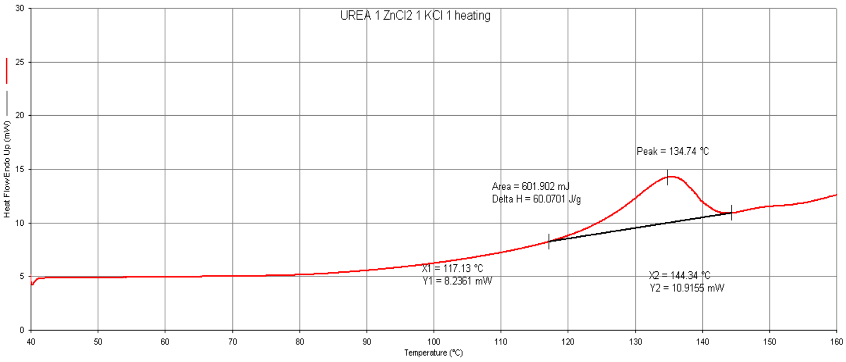

Fig. ESI-6. DSC trace for ZnKU form 1.

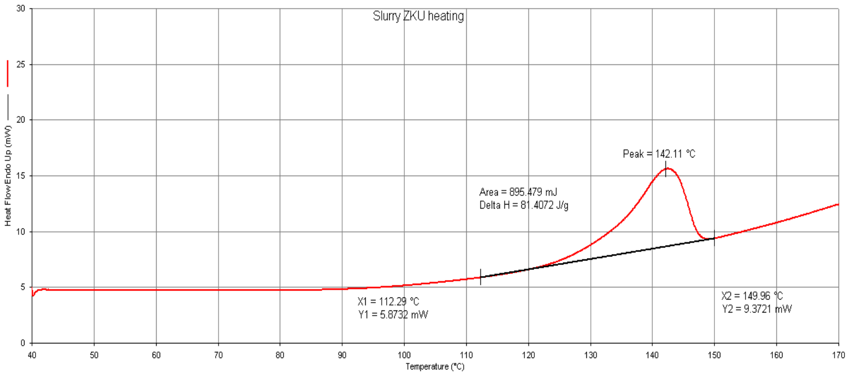

Fig. ESI-7. DSC trace for ZnKU form 2.

1.7 E-T diagram. Energy vs. Temperature (E-T) diagram for the dimorphic system ZnKU form 1 / ZnKU form 2. Form 2 has the higher melting point and the higher heat of fusion ($\Delta_m H_2$ 60 J/g vs. $\Delta_m H_1$ 81 J/g, for form 2 and form 1, respectively). According to the heat-of-fusion rule of Burger-Ramberger,[64] therefore, the system is monotropic.

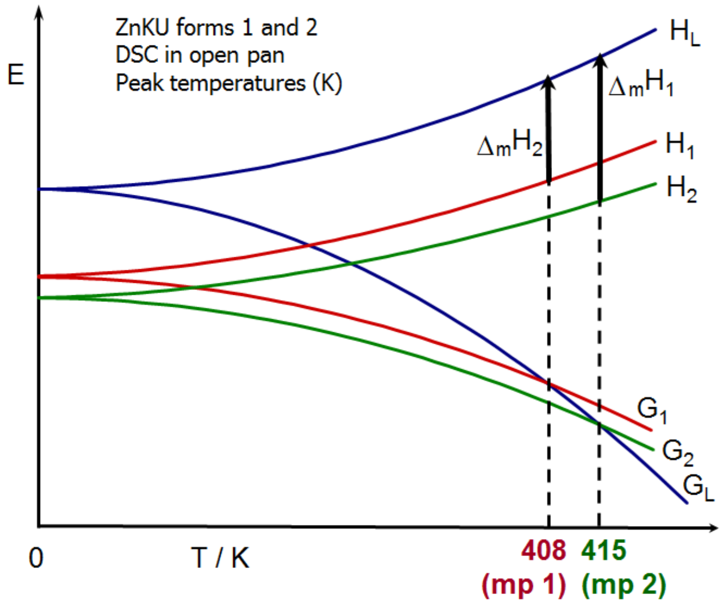

Fig. ESI-8. E-T diagram for the dimorphic system ZnKU form1 and ZnKU form 2.

X-ray diffraction analysis

Single Crystal X-ray Diffraction. Single Crystal data were collected at room temperature with an Oxford Diffraction X´Calibur equipped with a graphite monochromator and a CCD detector. Mo-Kα radiation (λ=0.71073 Å) was used. Unit cell parameters for all compounds discussed herein are reported in Table ESI-1. The structure was solved by the Intrinsic Phasing methods and refined by least squares methods again F^2 using SHELXT-2014[65] and SHELXL-2014[66] with OLEX 2 interface.[67] Non-hydrogen atoms were refined anisotropically. Hydrogen atoms bound to nitrogen atoms were either located from a Fourier map or added in calculated positions, and their position was refined riding on their N atoms. In ZnKU form 1 the NH_2 moieties of urea are disordered over two equivalent positions, referred by a crystallographic mirror plane. The software Mercury 3.10.1[68] was used for graphical representations and to simulate the powder patterns based on single crystal data.

Table ESI-1. Crystal data and details of measurements for ZnKU form 1 and form 2.

	ZnKU form1	**ZnKU form2**
Chemical formula	$CH_4Cl_3KN_2O$ Zn	$CH_4Cl_3KN_2O$ Zn
M_r, g*mol^{-1}	270.88	270.88
T / K	293 (2)	293 (2)
Morphology, colour	Block, colourless	Prism, colourless
Crystal system	Monoclinic	Monoclinic
Space group	$P\ 2_1/m$	$P\ 2_1/n$
a / Å	6.8599(10)	7.4220(6)
b / Å	7.3530(12)	13.5530(10)
c / Å	8.4999(11)	8.4219(5)
α / °	90	90
β / °	99.069(13)	92.089(7)
γ / °	90	90
V / Å^3	423.38(11)	846.60(11)
Z	2	4
d / mg.cm^{-3}	2.125	2.125
μ / mm^{-1}	4.266	4.266
Reflections collected/unique	1624/804	9911/1867
R_{int}	0.0521	0.0301
Threshold expression	$> 2\sigma(I)$	$> 2\sigma(I)$
R_1 (obs)	0.0589	0.0305
wR_2 (all)	0.1006	0.0834

X-ray Diffraction from Powder. For phase identification purposes X-ray powder diffraction (XRPD) patterns were collected on a PANalytical X´Pert Pro Automated diffractometer equipped with an X´celerator detector in Bragg-Brentano geometry, using Cu-Kα radiation (γ=1.5418 Å) without monochromator in 2θ range between 3º and 50º (step size 0.033º; time/step: 20 s; Soller slit 0,04 rad, antiscatter slit: ½, divergence slit: ¼ ; 40 mA*40kV).

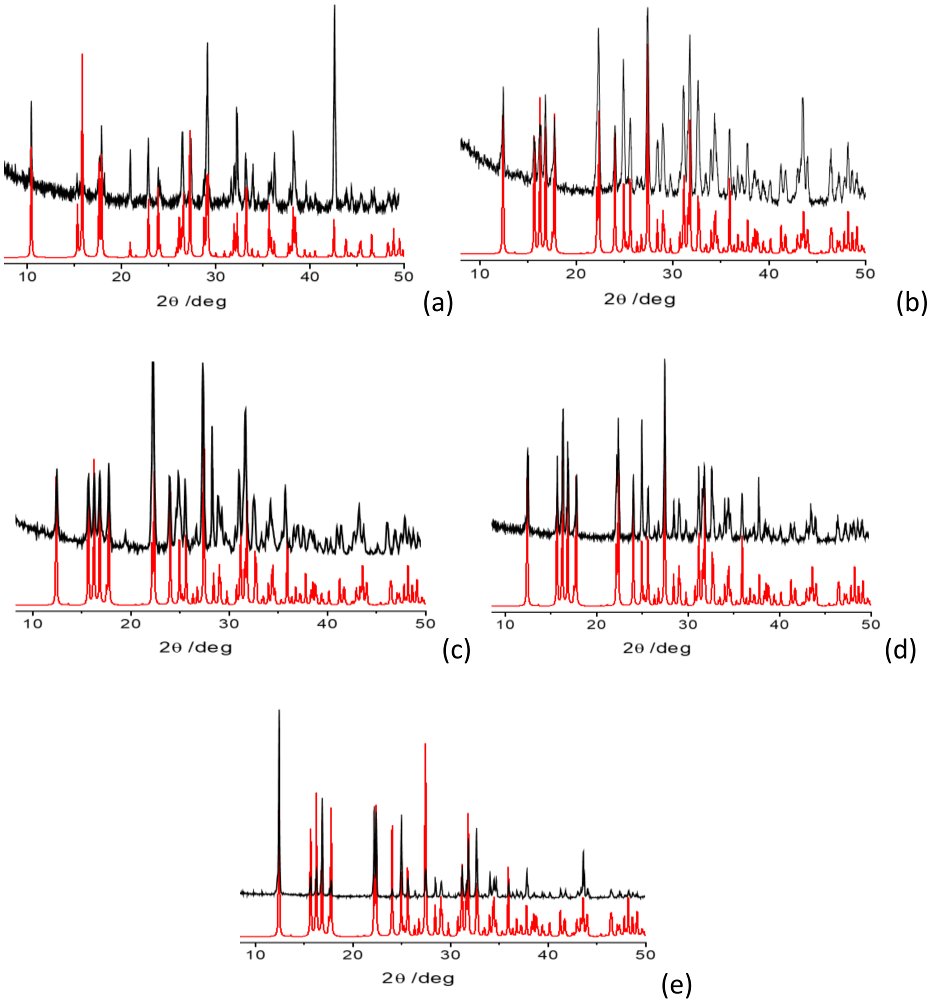

Fig. ESI-9 (a) Comparison of the experimental XRPD pattern for ZnKU form 1, as obtained from solution at 80°C, and the pattern calculated on the basis of single crystal data; (b) Comparison of the experimental XRPD pattern for ZnKU form 2, as obtained from solution, and the pattern calculated on the basis of single crystal data; (c) Comparison of the experimental XRPD pattern for ZnKU form 2, as obtained via ball milling, and the pattern calculated on the basis of single crystal data. (d) Comparison of the experimental XRPD pattern for the product of the 10 days slurry of ZnKU from 1; (e) Comparison of the experimental XRPD pattern for the residual, undissolved solid obtained in the solubility test, and the pattern calculated on the basis of single crystal data for ZnKU form 2. Black lines experimental, red lines calculated XRPD patterns.

Enzymatic assay using the pH-STAT method.

Urease activity was determined in triplicate using the pH-STAT method, as described by Blakeley et al.[39] In particular, a T1 pH-meter equipped with a 50-14 T electrode (Crison Instruments, SA), was used to record, every 0.5 min and for a 3 min reaction time, the volume of a 100 mmol L^{-1} HCl solution necessary to maintain the 10 mL solution containing urease and its substrate urea at the fixed pH value of 7.5. The measurement started 0.5 min after urea addition in order to allow time to reach uniform substrate concentration in the sample volume. One unit of enzyme is defined as the amount of urease required to hydrolyze 1 µmol urea $\min^{-1}$ of reaction.

Determination of the kinetic parameters for urea hydrolysis by urease.

The 10 mL reaction mixture was composed of 9.9 mL of 2 mmol L^{-1} 4-(2-hydroxyethyl)-1-piperazineethanesulfonic acid (HEPES) buffer at pH 7.5, containing increasing concentrations of urea in the range 1 - 64 mM. The reaction was started upon the addition of a concentrated solution (0.1 mL) of urease from *Canavalia ensiformis* (Jack Bean urease, JBU) (Sigma-Aldrich) to the reaction mixture. The resulting values for the enzyme activity measured at each concentration of urea were plotted as a function of substrate concentration and fitted by using the Michaelis-Menten equation (Equation S1) in order to derive the maximal velocity (V_{max}) for the enzymatic hydrolysis of urea, as well as the Michaelis constant (K_M) for the urease - urea couple.

$$reaction\ rate = \frac{V_{max}[S]}{K_M+[S]} \qquad \textbf{Eq. S1}$$

Determination of urease inhibition by ZnKU. The inhibition strengths of ZnKU form 1 and form 2 on urease were determined with the same experimental protocol of that described above for the enzyme in the absence of ZnKU. In this case, the reaction mixture consisted of 9.9 mL of 2 mM HEPES buffer at pH 7.50, also containing 64 mM of urea and increasing concentrations of ZnKU (0.54, 1.08 and 2.16 µg mL^{-1} in the case of ZnKU form 1, 0.69, 1.38 and 2.76 µg mL^{-1} in the case of ZnKU form 2). The slightly dissimilar concentrations used for the two ZnKU forms reflect the different stoichiometry of Zn(II) inside the two crystal forms and have been chosen in order to work at the same Zn^{2+} concentration. The experimental results were normalized with respect to the activity measured in the same conditions in the absence of ZnKU (control experiment) and plotted, as a percentage, as a function of the amount of inhibitor tested.

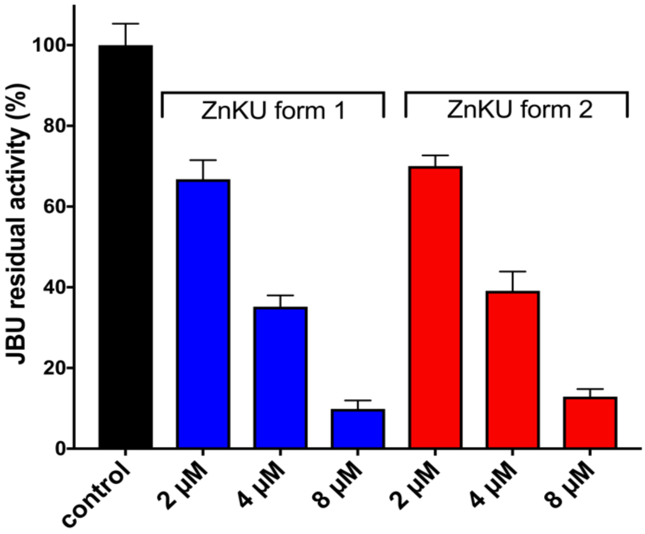

Fig. ESI-S10: Residual percentage activity of jack bean urease (JBU), referred to 100% (control, black bar) in the presence of increasing concentrations of the two polymorphic ZnKU compounds, at pH 7.5. The blue bars represent the residual activity of urease in the presence of 2, 4 and 8 µM of ZnKU form 1, while the red bars represent the residual activity of urease in the presence of the same concentrations of ZnKU form 2, as already described in the main text.

2.5 AMO and AMO inhibitors

Along with urease, another enzyme contained in the soil plays a key role in the nitrogen cycle, i.e. the copper-dependent enzyme ammonia monooxygenase (AMO):[69] it catalyzes the oxidation of ammonia into hydroxylamine (NH_2OH), precursor of several species responsible for the greenhouse effect.

AMO is produced in the ammonia oxidizing bacteria (AOB) together with the enzymes hydroxylamine oxidoreductase (HAO) and nitric oxide reductase (NOR), which finalize the nitrification process.[70] HAO catalyzes the conversion of NH_2OH into nitrite (NO_2^-), which is then transformed to gaseous forms of N such as nitric oxide (NO) and nitrous oxide (N_2O) - a greenhouse gas with 300 times the heat-trapping capacity of CO_2.[71] When nitrite is not involved in these processes, it is converted by NOR into nitrate (NO_3^-), which can be taken up by plant roots, leached into groundwater or involved in an anaerobic denitrification route.[72]

Since the most employed inhibitors are addressed towards the first step of nitrification, the enzyme target is mainly AMO.[73] However, the search for AMO inhibitors is complicated by the lack of information concerning its chemical structure: purified preparations of AMO with strong activity are not yet available, so much of the knowledge about AMO is deduced from experiments with intact cell or cell extracts.[74] Given the similarity between AMO and particulate methane monooxygenase (pMMO) from a catalytic, structural and genetic point of view, also the acquired knowledge on pMMO helps in the understanding of AMO.[75] To the present day, the studies support a model for the enzyme which consists of three subunits and metal centres of copper and iron (Fig.9).[76,78]

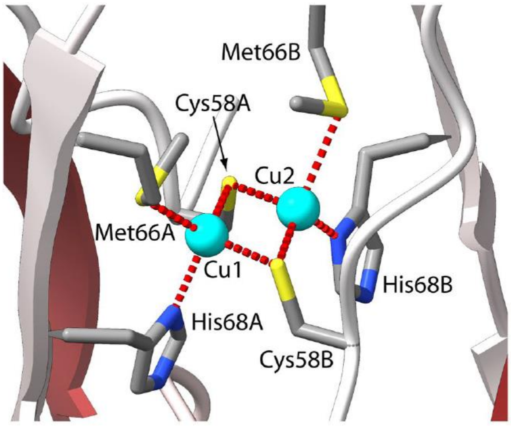

Fig.9: Detail of the copper-binding site (ref.78)

The limited knowledge about AMO structure leads to serious problems in the understanding of the inhibition mechanism, thus complicating the research of new inhibitors. At present, the broadening of this class of inhibitors is carried on through the synergic action of theoretical and experimental work, with the experimental data helping in the rationalisation of the mechanism.

The last urea-based co-crystal synthesized and characterized during my PhD research activity displays an inhibition activity towards the enzyme AMO - thanks to the co-former thiourea (Fig.11) - in addition to the inhibition activity towards urease.

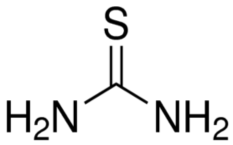

Fig.11: scheme of thiourea.

2.5.1. ZnTU

The co-crystal ZnTU has been successfully prepared through the co-crystallization of urea with thiourea and zinc chloride (Fig.12). The presence of Zn was found to be instrumental in the presence of both urea and thiourea in the same crystal: there are no crystal structures containing urea and thiourea in the CSD database.

Fig.12: scheme of thiourea.

Also in this case, co-crystallization was a powerful method to modulate the chemical-physical properties of urea as well as to provide important elements to the soil, i.e. nutrients and enzymatic inhibitors.

The methods and techniques used for the characterization of the solid-state products were the following:

- Single Crystal X-ray Diffraction (SCXRD) for structure determination.
- X-ray Powder Diffraction (XRPD) to determine whether the change of the phase took place, i.e. wheter there were new peaks different from those of the starting materials.
- Differential Scanning Calorimetry (DSC) for the detection of phase changes (dehydration/desolvation, polymorphic transition, melting).
- Thermogravimetric Analysis (TGA) to estimate the mass loss of the sample.
- Solubility test. This technique was used to determine the maximum quantity of urea in ZnTU capable of dissolving in a given amount of solvent.
- Stability test. This technique was emplyed to evaluate the stability of ZnTU with respect to the binary co-crystals $Zn[(urea)_2Cl_2]$ (ZnU) and $Zn[(thiourea)_2Cl_2]$ (ZnT) in a chamber at controlled humidity.

The inhibition of the enzymatic activity of both the enzymes, urease and AMO, was tested in the research group of prof. Stefano Ciurli.

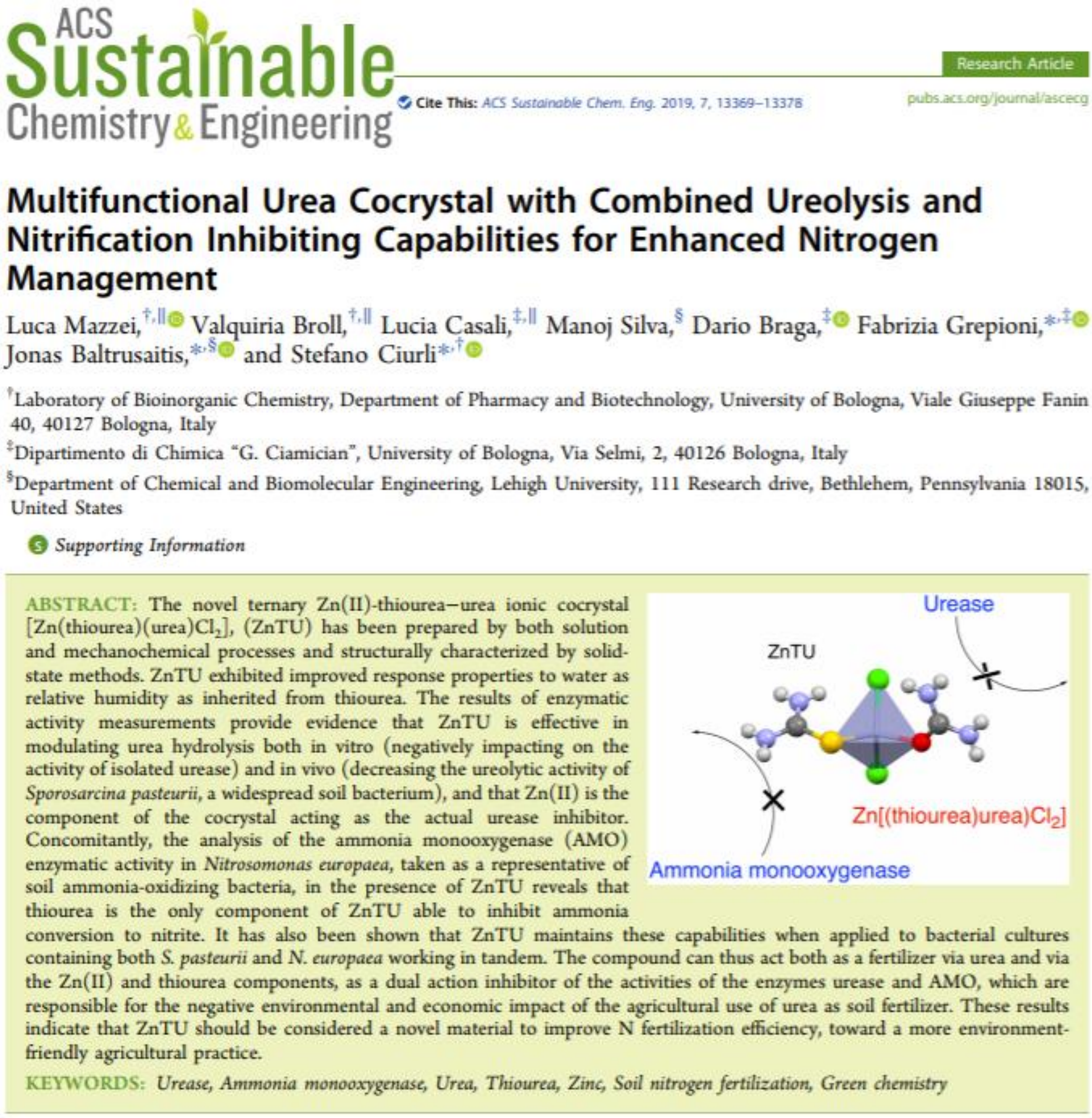

ACS Sustainable Chemistry & Engineering

Research Article

Cite This: ACS Sustainable Chem. Eng. 2019, 7, 13369−13378

pubs.acs.org/journal/ascecg

Multifunctional Urea Cocrystal with Combined Ureolysis and Nitrification Inhibiting Capabilities for Enhanced Nitrogen Management

Luca Mazzei,[†,∥] Valquiria Broll,[†,∥] Lucia Casali,[‡,∥] Manoj Silva,[§] Dario Braga,[‡] Fabrizia Grepioni,*[,‡] Jonas Baltrusaitis,*[,§] and Stefano Ciurli*[,†]

[†] Laboratory of Bioinorganic Chemistry, Department of Pharmacy and Biotechnology, University of Bologna, Viale Giuseppe Fanin 40, 40127 Bologna, Italy

[‡] Dipartimento di Chimica "G. Ciamician", University of Bologna, Via Selmi, 2, 40126 Bologna, Italy

[§] Department of Chemical and Biomolecular Engineering, Lehigh University, 111 Research drive, Bethlehem, Pennsylvania 18015, United States

Supporting Information

ABSTRACT: The novel ternary Zn(II)-thiourea−urea ionic cocrystal [Zn(thiourea)(urea)Cl_2], (ZnTU) has been prepared by both solution and mechanochemical processes and structurally characterized by solid-state methods. ZnTU exhibited improved response properties to water as relative humidity as inherited from thiourea. The results of enzymatic activity measurements provide evidence that ZnTU is effective in modulating urea hydrolysis both in vitro (negatively impacting on the activity of isolated urease) and in vivo (decreasing the ureolytic activity of *Sporosarcina pasteurii*, a widespread soil bacterium), and that Zn(II) is the component of the cocrystal acting as the actual urease inhibitor. Concomitantly, the analysis of the ammonia monooxygenase (AMO) enzymatic activity in *Nitrosomonas europaea*, taken as a representative of soil ammonia-oxidizing bacteria, in the presence of ZnTU reveals that thiourea is the only component of ZnTU able to inhibit ammonia conversion to nitrite. It has also been shown that ZnTU maintains these capabilities when applied to bacterial cultures containing both *S. pasteurii* and *N. europaea* working in tandem. The compound can thus act both as a fertilizer via urea and via the Zn(II) and thiourea components, as a dual action inhibitor of the activities of the enzymes urease and AMO, which are responsible for the negative environmental and economic impact of the agricultural use of urea as soil fertilizer. These results indicate that ZnTU should be considered a novel material to improve N fertilization efficiency, toward a more environment-friendly agricultural practice.

KEYWORDS: *Urease, Ammonia monooxygenase, Urea, Thiourea, Zinc, Soil nitrogen fertilization, Green chemistry*

For copyright reasons only the link to the original article is reported here:

https://doi.org/10.1021/acssuschemeng.9b02607

2.5.2 Supporting Information

Crystallographic data and details of measurements for ZnTU.

	ZnTU
Chemical formula	$C_2H_8Cl_2N_4OSZn$
M_r, g mol^{-1}	272.47
T / K	293 (2)
Morphology, colour	Block, colourless
Crystal system	Monoclinic
Space group	$P\ 2_1/c$
a / Å	11.7246(10)
b / Å	6.8740(5)
c / Å	11.9092(8)
α / °	90
β / °	97.013(7)
γ / °	90
V / Å^3	952.6(1)
Z	4
d / mg cm^{-3}	1.900
μ / mm^{-1}	3.312
Reflections collected/unique	7014/2256
R_{int}	0.0382
Threshold expression	$> 2\sigma(I)$
R_1 (obs)	0.0543
wR_2 (all)	0.1465

Figure 1-SI. DSC traces for (top to bottom) urea, thiourea, ZnU, ZnT, and ZnTU.

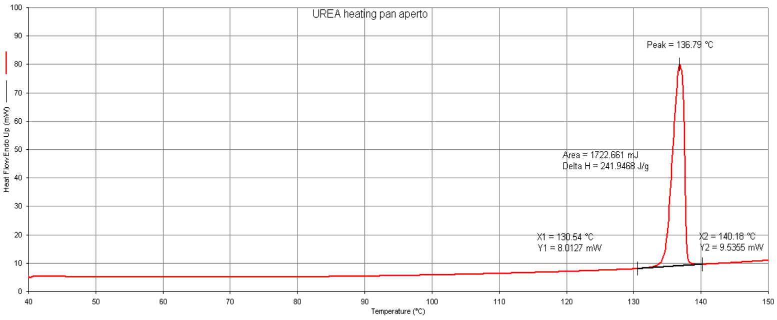

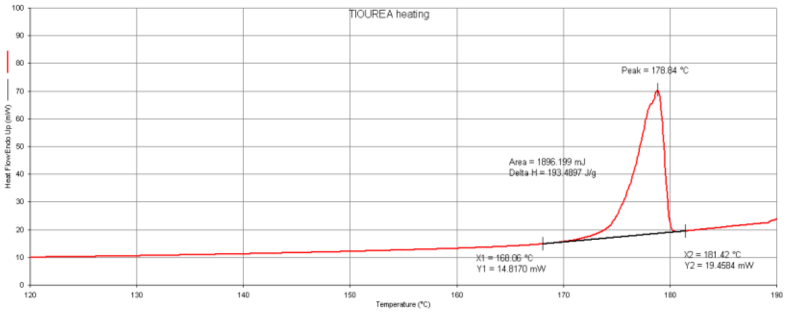
TIOUREA heating
Peak = 178.84 °C
Area = 1896.199 mJ
Delta H = 193.4897 J/g
X1 = 168.06 °C
Y1 = 14.8170 mW
X2 = 181.42 °C
Y2 = 19.4584 mW
Heat Flow Endo Up (mW)
Temperature (°C)
0
10
20
30
40
50
60
70
80
90
100
120
130
140
150
160
170
180
190

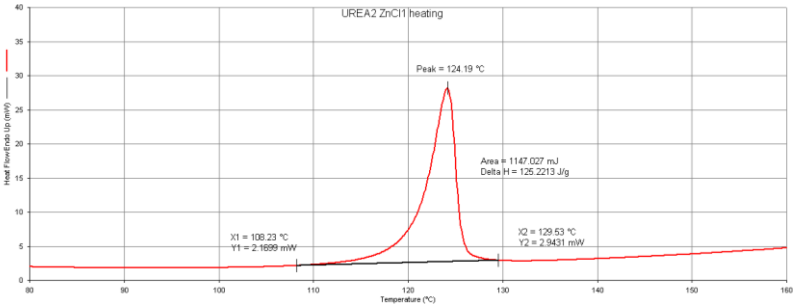
UREA2 ZnCl1 heating
Peak = 124.19 °C
Area = 1147.027 mJ
Delta H = 125.2213 J/g
X1 = 108.23 °C
Y1 = 2.1899 mW
X2 = 129.53 °C
Y2 = 2.9431 mW
Heat Flow Endo Up (mW)
Temperature (°C)
0
5
10
15
20
25
30
35
40
80
90
100
110
120
130
140
150
160

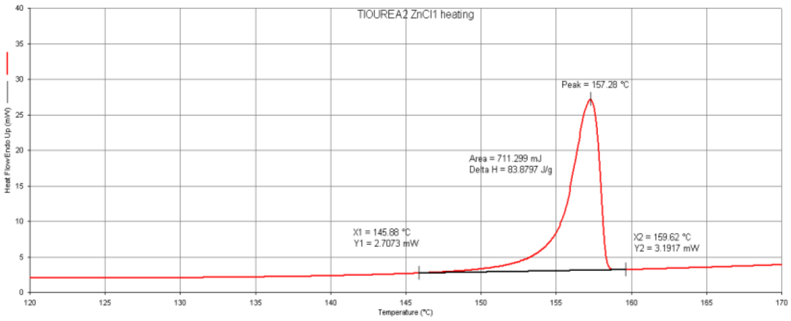
TIOUREA2 ZnCl1 heating
Peak = 157.28 °C
Area = 711.299 mJ
Delta H = 83.8797 J/g
X1 = 145.88 °C
Y1 = 2.7073 mW
X2 = 159.62 °C
Y2 = 3.1917 mW
Heat Flow Endo Up (mW)
Temperature (°C)
0
5
10
15
20
25
30
35
40
120
125
130
135
140
145
150
155
160
165
170

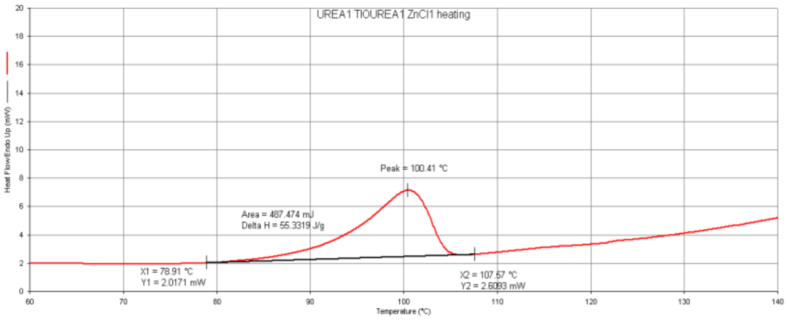
UREA1 TIOUREA1 ZnCl1 heating
Peak = 100.41 °C
Area = 487.474 mJ
Delta H = 55.3319 J/g
X1 = 78.91 °C
Y1 = 2.0171 mW
X2 = 107.57 °C
Y2 = 2.6093 mW
Heat Flow Endo Up (mW)
Temperature (°C)
0
2
4
6
8
10
12
14
16
18
20
60
70
80
90
100
110
120
130
140

Figure 2-SI. TGA traces for (top to bottom) urea, thiourea, ZnU, ZnT, and ZnTU.

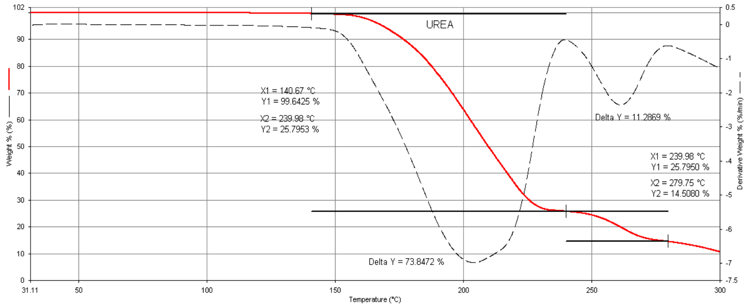

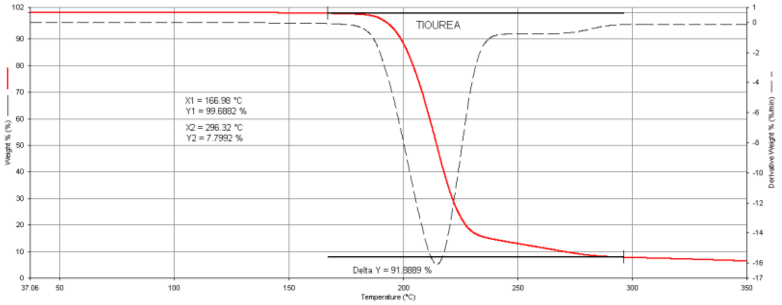

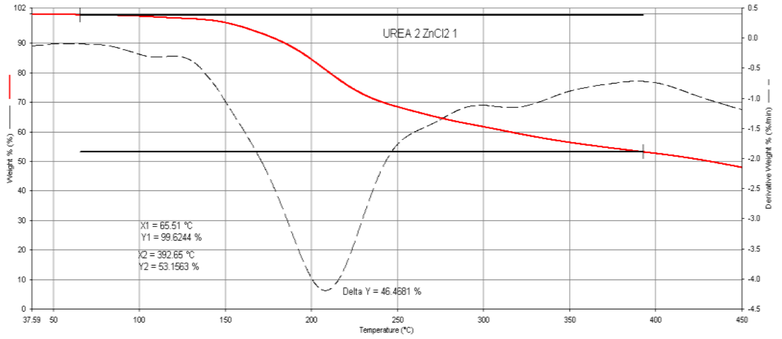

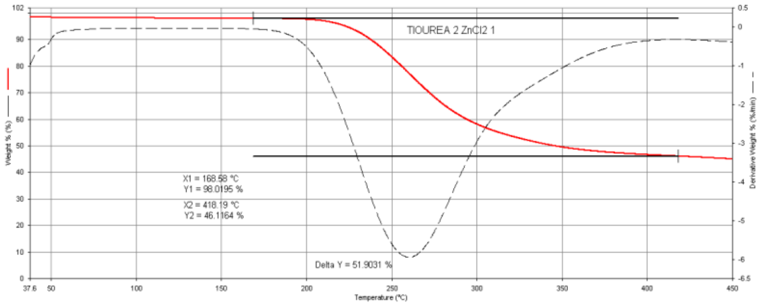

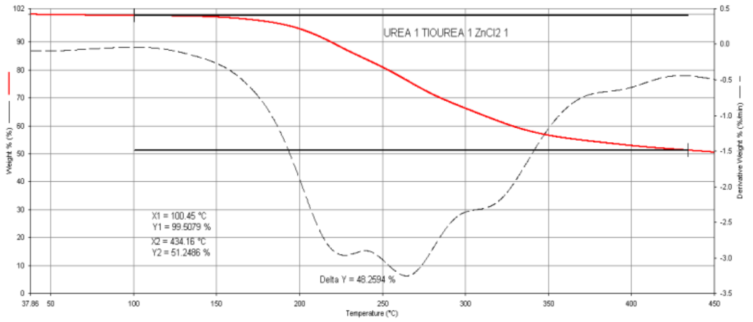

Figure 3-SI Representative raw data diagram showing the amount of oxygen consumed over time during *N. europaea* reactions. The experimental conditions are described in the material and methods section.

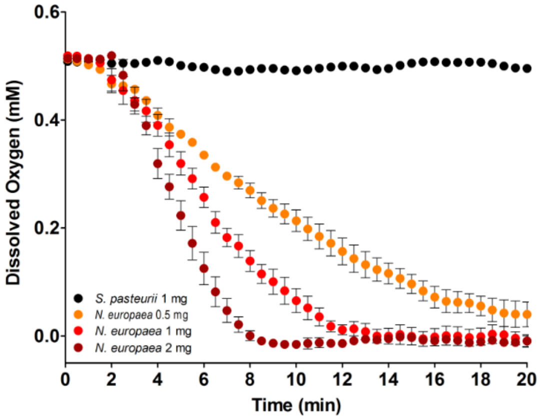

Figure 4-SI X-ray powder pattern (black line) of the residual solid (2.82 g) obtained upon addition of 4.53 g of ZnTU (containing 1 g of urea) to 1 mL of water. It can be appreciated that the residual solid is a mixture of ZnTU (red line) and ZnT (blue line).

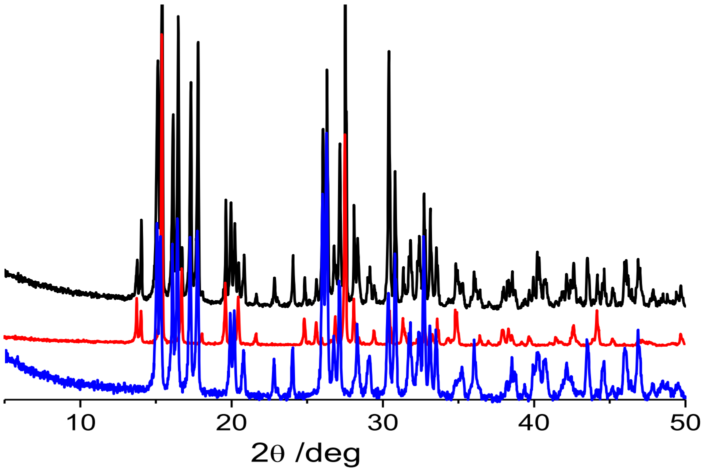

Figure 5-SI Comparison of the experimental powder patterns measured on a freshly prepared sample (black line) of ZnTU and on the same sample stored for 6-months (red line) at ambient conditions in an open flask.

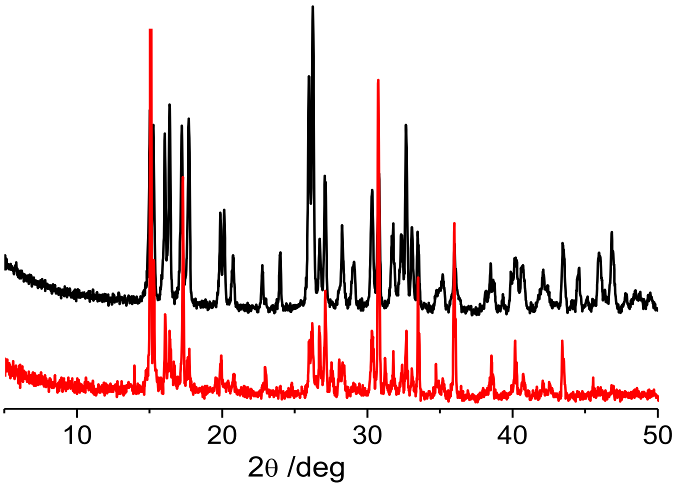

Figure 6-SI. ZnTU, ZnU and ZnT as prepared (t = 0) and after three days in a chamber at controlled humidity (82 % RH). It is evident that, while ZnU has absorbed water and turned into an aqueous solution, ZnTU shows the same behavior as ZnT (still a dry powder), suggesting that urea in ZnTU is stabilized with respect to urea in ZnU.

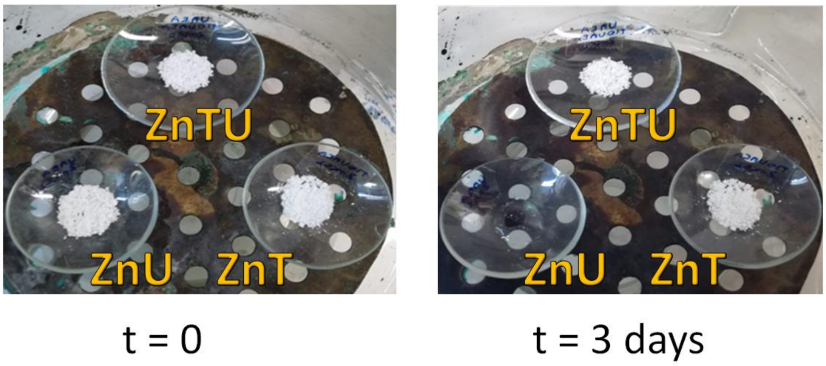

Figure 7-SI. Adsorption/desorption branches of RH on urea, ZnU, thiourea, and ZnT

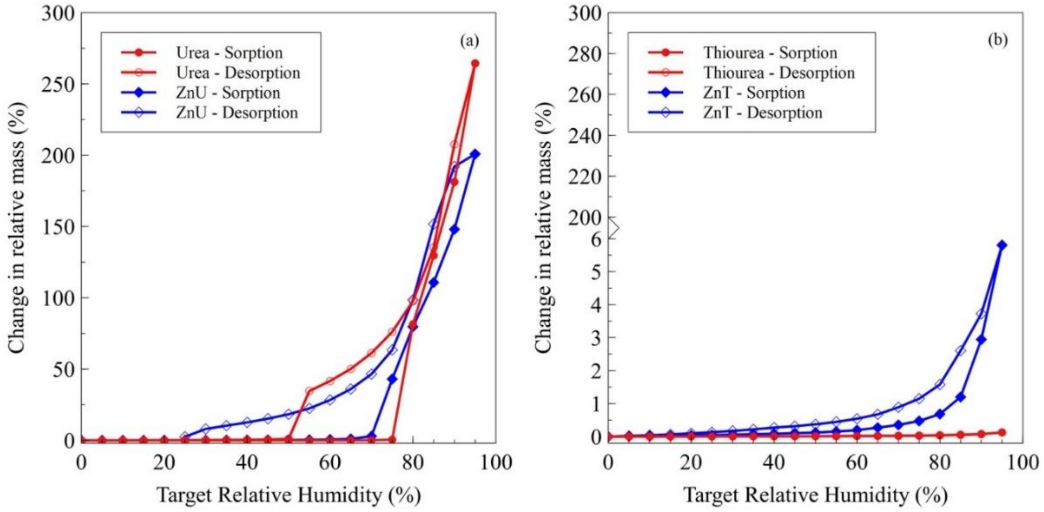

2.6. Conclusions

Urea is projected to reach an annual production of 226 million tons in the next years therefore the quest for sustainable urea-based fertilizers is today more important than ever. Indeed, only 47% of the total N delivered to the soil with urea-based fertilizers is effectively utilized by plants, with serious economic, agronomic and environmental implications. The N-loss is mainly related to the presence in the soil of the enzymes urease and AMO, which are responsible of the fast hydrolysis of urea and of the subsequent production of greenhouse species.

To the present day, two main methods have been employed to tackle this problem, i.e. the coating/encapsulation of urea or the amendment of urea-based fertilizers with AMO inhibitors: the first approach is aimed to reduce the water solubility/dissolution rate of urea while the other one directly affects the enzymatic activity of urease and AMO.

Part of my PhD research activity addressed the design and development of urea-based co-crystals as a novel class of crystalline fertilizers. The design of urea co-crystals for agrochemical applications had already been suggested,[77] but the novelty of the systems here presented lies in the ability to reconcile both the above-mentioned aspects, i.e. improve the chemical-physical properties of urea - by reducing its water solubility/dissolution rate - and explicit an inhibition activity towards the enzymes urease and/or AMO. The research project was developed in three steps, starting with a binary co-crystal as prototype up to a more performing ternary co-crystal.

Urea-catechol was the first system succesfully synthesized and characterized. The dual objective of improving the chemical-physical properties of urea and inhibiting the enzyme urease was completely fullfilled: the water solubility and hygroscopicity of urea were reduced, while the inhibition activity carried out by catechol was likely improved. The next step in the development of innovative crystalline fertilizers resulted in the obtainment of ZnKU ($ZnCl_2$-KCl-urea based co-crystal): compared to urcat, this system has the added benefit of supplying to the soil other essential elements for the plants, i.e. macronutrients and micronutrients. Finally, the ternary co-crystal ZnTU ($ZnCl_2$-thiourea-urea based co-crystal) represented the final step of this research project, whereby urea has been co-crystallized with inhibitors of both urease and AMO.

Along with the already mentioned advantages, it is worth pointing out that these systems are extremely advantageous also from a manufacturing point of view. Indeed, all the co-crystals were synthsized through a solvent-free mechanochemical method, which provided pure products quickly and quantitavely.

In the light of the results obtained in this research, the co-crystallization method was proven to be a powerful tool for the design of novel crystalline fertilizers. A future work could be addressed to the investigation of new possible co-formers to co-crystallize urea with, thus expanding the class of these novel urea-based fertilizers.

References

1. Steffen, W., Crutzen, P. J. & McNeill, J. R. Week 1-Steffen et al (2007) http://dx.doi.org/10.1579/0044-7447(2007)36[614:TAAHNO]2.0.CO;2. *AMBIO A J. Hum. Environ.* **36,** 614–621 (2007).
2. Wahlström, M., Sommer, M., Kocyba, P., de Vydt, M., De Moor, J., Davies, S., Wouters, R., Wennerhag, M., van Stekelenburg, J., Uba, K., Saunders, C., Rucht, D., Mickecz, D., Zamponi, L., Lorenzini, J., Kołczyńska, M., Haunss, S., Giugni, M., Gaidyte, T., Doherty, B. & Buzogany, A. Protest for a future: Composition, mobilization and motives of the participants in Fridays For Future climate protests on 15 March, 2019 in 13 European cities. *Keele Univ.* (2019).
3. United Nations. The sustainable development goals report 2019. *United Nations Publ. issued by Dep. Econ. Soc. Aff.* 64 (2019).
4. Lewis, S. L. & Maslin, M. A. Defining the Anthropocene. *Nature* **519,** 171–180 (2015).
5. Zalasiewicz, J., Waters, C., Summerhayes, C. & Williams, M. The Anthropocene. *Geol. Today* **34,** 177–181 (2018).
6. Zalasiewicz, J., Waters, C. N., Williams, M., Barnosky, A. D., Cearreta, A., Crutzen, P., Ellis, E., Ellis, M. A., Fairchild, I. J., Grinevald, J., Haff, P. K., Hajdas, I., Leinfelder, R., McNeill, J., Odada, E. O., Poirier, C., Richter, D., Steffen, W., Summerhayes, C., Syvitski, J. P. M., Vidas, D., Wagreich, M., Wing, S. L., Wolfe, A. P., An, Z. & Oreskes, N. When did the Anthropocene begin? A mid-twentieth century boundary level is stratigraphically optimal. *Quat. Int.* **383,** 196–203 (2015).
7. Biermann, F., Bai, X., Bondre, N., Broadgate, W., Arthur Chen, C. T., Dube, O. P., Erisman, J. W., Glaser, M., van der Hel, S., Lemos, M. C., Seitzinger, S. & Seto, K. C. Down to Earth: Contextualizing the Anthropocene. *Glob. Environ. Chang.* **39,** 341–350 (2016).
8. Erisman, J. W., Sutton, M. A., Galloway, J., Klimont, Z. & Winiwarter, W. How a century of ammonia synthesis changed the world. *Nat. Geosci.* **1,** 636–639 (2008).
9. GALLOWAY, J. N., ABER, J. D., ERISMAN, J. W., SEITZINGER, S. P., HOWARTH, R. W., COWLING, E. B. & COSBY, B. J. The Nitrogen Cascade. *Bioscience* **53,** 341 (2003).
10. Baltrusaitis, J. Sustainable Ammonia Production. *ACS Sustain. Chem. Eng.* **5,** 9527 (2017).
11. Vojvodic, A., Medford, A. J., Studt, F., Abild-Pedersen, F., Khan, T. S., Bligaard, T. & Nørskov, J. K. Exploring the limits: A low-pressure, low-temperature Haber-Bosch process. *Chem. Phys. Lett.* **598,** 108–112 (2014).
12. Krase, N. W. & Gaddy, V. L. Synthesis of Urea from Ammonia and Carbon Dioxide. *Ind. Eng. Chem.* **14,** 611–615 (1922).
13. Krupa, S. V. Effects of atmospheric ammonia (NH3) on terrestrial vegetation: A review. *Environ.*

Pollut. **124,** 179–221 (2003).

14. Van Kessel, M. A. H. J., Speth, D. R., Albertsen, M., Nielsen, P. H., Op Den Camp, H. J. M., Kartal, B., Jetten, M. S. M. & Lücker, S. Complete nitrification by a single microorganism. *Nature* **528,** 555–559 (2015).
15. Evans, A. The Feeding of the Nine Billion. *Chatham House Rep.* 1–59 (2009). at <www.chathamhouse.org.uk>
16. IFA. Fertilizer Outlook 2014-2018. *82nd IFA Annu. Conf. Sydney* 1–7 (2014).
17. Prosekov, A. Y. & Ivanova, S. A. Food security: The challenge of the present. *Geoforum* **91,** 73–77 (2018).
18. Johnston, R. B. Arsenic and the 2030 Agenda for sustainable development. *Arsen. Res. Glob. Sustain. - Proc. 6th Int. Congr. Arsen. Environ. AS 2016* 12–14 (2016). doi:10.1201/b20466-7
19. Banerjee, C. & Adenaeuer, L. Up, Up and Away! The Economics of Vertical Farming. *J. Agric. Stud.* **2,** 40 (2014).
20. Regulation (EU) 2019/1009. Regulation (EU) 2019/1009 of the European Parliament and of the Council of 5 June 2019, laying down rules on the making available on the market of EU fertilising products and amending Regulations (EC) No 1069/2009 and (EC) No 1107/2009 and repealing Regul. *Off. J. Eur. Union* **2019,** 1–114 (2019).
21. Timilsena, Y. P., Adhikari, R., Casey, P., Muster, T., Gill, H. & Adhikari, B. Enhanced efficiency fertilisers: A review of formulation and nutrient release patterns. *J. Sci. Food Agric.* **95,** 1131–1142 (2015).
22. Mazzei, L., Broll, V. & Ciurli, S. An Evaluation of Maleic-Itaconic Copolymers as Urease Inhibitors. *Soil Sci. Soc. Am. J.* **82,** 994–1003 (2018).
23. City, S. L. & Simmons, P. E. U . S . Patent Jun . 24 , 1986. (1981).
24. Becker, K.; Jancke, W. Z. No Title. *Phys. Chem.* **99,** 242–274 (1921).
25. Powell, K. A., Bartolini, G., Wittering, K. E., Saleemi, A. N., Wilson, C. C., Rielly, C. D. & Nagy, Z. K. Toward Continuous Crystallization of Urea-Barbituric Acid: A Polymorphic Co-Crystal System. *Cryst. Growth Des.* **15,** 4821–4836 (2015).
26. Nelyubina, Y. V., Lyssenko, K. A., Golovanov, D. G. & Antipin, M. Y. NO3-···NO3- and NO 3-···π interactions in the crystal of urea nitrate. *CrystEngComm* **9,** 991–996 (2007).
27. Parkin, A., Harte, S. M., Goeta, A. E. & Wilson, C. C. Imaging proton migration from X-rays and neutrons. *New J. Chem.* **28,** 718–721 (2004).
28. Lee, R., Mason, S. A., Mossou, E., Lamming, G., Probert, M. R. & Steed, J. W. Neutron Diffraction Studies on Guest-Induced Distortions in Urea Inclusion Compounds. *Cryst. Growth Des.* **16,** 7175–7185 (2016).
29. Mullen, D. Electron-density distribution in urea. A multipolar expansion. *Acta Crystallogr. Sect. B Struct. Crystallogr. Cryst. Chem.* **36,** 1610–1615 (1980).
30. Roszak, K. & Katrusiak, A. Giant anomalous strain between high-pressure phases and the

mesomers of urea. *J. Phys. Chem. C* **121,** 778–784 (2017).

31. Olejniczak, A., Ostrowska, K. & Katrusiak, A. H-bond breaking in high-pressure urea. *J. Phys. Chem. C* **113,** 15761–15767 (2009).

32. Macrae, C. F., Bruno, I. J., Chisholm, J. A., Edgington, P. R., McCabe, P., Pidcock, E., Rodriguez-Monge, L., Taylor, R., Van De Streek, J. & Wood, P. A. Mercury CSD 2.0 - New features for the visualization and investigation of crystal structures. *J. Appl. Crystallogr.* **41,** 466–470 (2008).

33. Maroney, M. J. & Ciurli, S. Nonredox nickel enzymes. *Chem. Rev.* **114,** 4206–4228 (2014).

34. Hand, J. L., Schichtel, B. A., Pitchford, M., Malm, W. C. & Frank, N. H. Seasonal composition of remote and urban fine particulate matter in the United States. *J. Geophys. Res. Atmos.* **117,** 1–22 (2012).

35. Paulot, F. & Jacob, D. J. Hidden cost of U.S. agricultural exports: Particulate matter from ammonia emissions. *Environ. Sci. Technol.* **48,** 903–908 (2014).

36. Hristov, A. N. Technical note: Contribution of ammonia emitted from livestock to atmospheric fine particulate matter (PM2.5) in the United States. *J. Dairy Sci.* **94,** 3130–3136 (2011).

37. Biagi, F., Musiani, F. & Ciurli, S. Structure of the UreD-UreF-UreG-UreE complex in Helicobacter pylori: A model study. *J. Biol. Inorg. Chem.* **18,** 571–577 (2013).

38. Sumner, J. B. Enzyme Urease. *J. Biol. Chem.* **69,** 435–441 (1926).

39. Blakeley, R. L., Webb, E. C. & Zerner, B. Jack Bean Urease (EC 3.5.1.5). A New Purification and Reliable Rate Assay. *Biochemistry* **8,** 1984–1990 (1969).

40. Zambelli, B., Musiani, F., Benini, S. & Ciurli, S. Chemistry of Ni 2. *Acc. Chem. Res.* **44,** 520–530 (2011).

41. Dixon, N. E., Riddles, P. W., Gazzola, C., Blakeley, R. L. & Zerner, B. Jack bean urease (EC 3.5.1.5). V. On the mechanism of action of urease on urea, formamide, acetamide, N-methylurea, and related compounds. *Can. J. Biochem.* **58,** 1335–1344 (1980).

42. Karplus, P. A., Pearson, M. A. & Hausinger, R. P. 70 Years of Crystalline Urease: What Have We Learned? *Acc. Chem. Res.* **30,** 330–337 (1997).

43. Pearson, M. A., Park, I. S., Schaller, R. A., Michel, L. O., Karplus, P. A. & Hausinger, R. P. Kinetic and structural characterization of urease active site variants. *Biochemistry* **39,** 8575–8584 (2000).

44. Todd, M. J. & Hausinger, R. P. Fluoride inhibition of Klebsiella aerogenes urease: Mechanistic implications of a pseudo-uncompetitive, slow-binding inhibitor. *Biochemistry* **39,** 5389–5396 (2000).

45. Mazzei, L., Cianci, M., Benini, S. & Ciurli, S. The Structure of the Elusive Urease–Urea Complex Unveils the Mechanism of a Paradigmatic Nickel-Dependent Enzyme. *Angew. Chemie - Int. Ed.* **58,** 7415–7419 (2019).

46. Mazzei, L., Cianci, M., Musiani, F., Lente, G., Palombo, M. & Ciurli, S. Inactivation of urease by catechol: Kinetics and structure. *J. Inorg. Biochem.* **166,** 182–189 (2017).

47. Mazzei, L., Cianci, M., Musiani, F. & Ciurli, S. Inactivation of urease by 1,4-benzoquinone:

Chemistry at the protein surface. *Dalt. Trans.* **45,** 5455–5459 (2016).

48. Carvalhais, L. C., Dennis, P. G., Fedoseyenko, D., Hajirezaei, M. R., Borriss, R. & Von Wirén, N. Root exudation of sugars, amino acids, and organic acids by maize as affected by nitrogen, phosphorus, potassium, and iron deficiency. *J. Plant Nutr. Soil Sci.* **174,** 3–11 (2011).
49. Jarosiewicz, A. & Tomaszewska, M. Controlled-release NPK fertilizer encapsulated by polymeric membranes. *J. Agric. Food Chem.* **51,** 413–417 (2003).
50. Chien, S. H. Solubility assessment for fertilizer containing phosphate rock. *Fertil. Res.* **35,** 93–99 (1993).
51. Associatioll, P. C. Published 1965 32. 400–412 (1965).
52. GLOBAL Vision – Values – Culture of Excellence NOTE TO THE IFA. (2019).
53. International Fertilizer Association. Short-Term Fertilizer Outlook 2019 – 2020. 1–8 (2019).
54. European Commission. Fertilisers in the EU Prices, trade and use. 5 (2019). at <http://ec.europa.eu/agriculture/markets-and-prices/market-briefs/index_en.htm%0Ahttps://ec.europa.eu/info/sites/info/files/food-farming-fisheries/farming/documents/market-brief-fertilisers_june2019_en.pdf>
55. Römheld, V. & Marschner, H. Function of Micronutrients in Plants. 297–328 (2018). doi:10.2136/sssabookser4.2ed.c9
56. MICRONUTRIENTS. (2019).
57. Gödecke, T., Stein, A. J. & Qaim, M. The global burden of chronic and hidden hunger: Trends and determinants. *Glob. Food Sec.* **17,** 21–29 (2018).
58. Willett, L. J., Hashim, S. A. F., Tompson, R. V. & Loyalka, S. K. Effect of surface heterogeneities on condensation on an aerosol particle. *J. Aerosol Sci.* **30,** 569–585 (1999).
59. Cakmak, I. & Kutman, U. B. Agronomic biofortification of cereals with zinc: a review. *Eur. J. Soil Sci.* **69,** 172–180 (2018).
60. Kutman, U. B., Yildiz, B., Ozturk, L. & Cakmak, I. Biofortification of durum wheat with zinc through soil and foliar applications of nitrogen. *Cereal Chem.* **87,** 1–9 (2010).
61. Yang, Z. X., Liu, S. Q., Zheng, D. W. & Feng, S. D. Effects of cadium, zinc and lead on soil enzyme activities. *J. Environ. Sci. (China)* **18,** 1135–1141 (2006).
62. Bebga, G., Ndassa, I. M., Ndong, P. R., Misse, P. R. N. & Fokwa, B. P. T. Crystal structure of potassium trans-diaquabis[oxalato- κ2O,O] chromate(III) urea disolvate, K[Cr(C2O 4)2(H2O)2]•2CO(NH 2)2, C6H12CrKN4O 12. *Zeitschrift fur Krist. - New Cryst. Struct.* **228,** 175–176 (2013).
63. Pinck, L. A. & Kelly, M. A. The Solubility of Urea in Water. *J. Am. Chem. Soc.* **47,** 2170–2172 (1925).
64. Bernstein, J. *Polymorphism in Molecular Crystals*. (Oxford University Press, 2002).
65. Sheldrick, G. M. SHELXT - Integrated space-group and crystal-structure determination. *Acta Crystallogr. Sect. A Found. Crystallogr.* **71,** 3–8 (2015).
66. Sheldrick, G. M. Crystal structure refinement with SHELXL. *Acta Crystallogr. Sect. C Struct. Chem.*

71, 3–8 (2015).

67. Dolomanov, O. V., Bourhis, L. J., Gildea, R. J., Howard, J. A. K. & Puschmann, H. OLEX2: A complete structure solution, refinement and analysis program. *J. Appl. Crystallogr.* **42,** 339–341 (2009).

68. MacRae, C. F., Sovago, I., Cottrell, S. J., Galek, P. T. A., McCabe, P., Pidcock, E., Platings, M., Shields, G. P., Stevens, J. S., Towler, M. & Wood, P. A. Mercury 4.0: From visualization to analysis, design and prediction. *J. Appl. Crystallogr.* **53,** 226–235 (2020).

69. Stein, L. Y. & Klotz, M. G. The nitrogen cycle. *Curr. Biol.* **26,** R94–R98 (2016).

70. Beeckman, F., Motte, H. & Beeckman, T. Nitrification in agricultural soils: impact, actors and mitigation. *Curr. Opin. Biotechnol.* **50,** 166–173 (2018).

71. Coskun, D., Britto, D. T., Shi, W. & Kronzucker, H. J. Nitrogen transformations in modern agriculture and the role of biological nitrification inhibition. *Nat. Plants* **3,** 1–10 (2017).

72. Arp, D. J. & Stein, L. Y. Metabolism of Inorganic N Compounds by Ammonia-Oxidizing Bacteria. *Crit. Rev. Biochem. Mol. Biol.* **38,** 471–495 (2003).

73. Byrne, M. P., Tobin, J. T., Forrestal, P. J., Danaher, M., Nkwonta, C. G., Richards, K., Cummins, E., Hogan, S. A. & O'Callaghan, T. F. Urease and nitrification inhibitors-As mitigation tools for greenhouse gas emissions in sustainable dairy systems: A review. *Sustain.* **12,** 1–35 (2020).

74. Fisher, O. S., Kenney, G. E., Ross, M. O., Ro, S. Y., Lemma, B. E., Batelu, S., Thomas, P. M., Sosnowski, V. C., DeHart, C. J., Kelleher, N. L., Stemmler, T. L., Hoffman, B. M. & Rosenzweig, A. C. Characterization of a long overlooked copper protein from methane- and ammonia-oxidizing bacteria. *Nat. Commun.* **9,** 1–12 (2018).

75. Norton, J. M., Alzerreca, J. J., Suwa, Y. & Klotz, M. G. Diversity of ammonia monooxygenase operon in autotrophic ammonia-oxidizing bacteria. *Arch. Microbiol.* **177,** 139–149 (2002).

76. Arp, D. J., Chain, P. S. G. & Klotz, M. G. The impact of genome analyses on our understanding of ammonia-oxidizing bacteria. *Annu. Rev. Microbiol.* **61,** 503–528 (2007).

77. Honer, K., Kalfaoglu, E., Pico, C., McCann, J. & Baltrusaitis, J. Mechanosynthesis of Magnesium and Calcium Salt-Urea Ionic Cocrystal Fertilizer Materials for Improved Nitrogen Management. *ACS Sustain. Chem. Eng.* **5,** 8546–8550 (2017).

78. Musiani, F., Broll, V., Evangelisti, E. & Ciurli, S. The model structure of the copper-dependent ammonia monooxygenase. *J. Biol. Inorg. Chem.* **25,** 995–1007 (2020).

CHAPTER 3

CRYSTALLINE MATERIALS OF AGROCHEMICAL INTEREST

PART II

CRYSTALLINE MATERIALS BASED ON AMO INHIBITORS

In this chapter, the results of the thorough solid-state investigation of crystalline materials based on AMO inhibitors will be presented. The experimental work was initiated at the University of Bologna and has continued at the research institute BAM (Bundesanstalt für Materialforschung und -prüfung) in Berlin, where I am currently (December 2020) spending a research period as visiting PhD student. Since several experiments are still in progress, I report here promising - but still preliminary - results.

3.1 Exploring the solid-state reactivity of AMO and urease inhibitors: co-crystallization of DCD with copper(II) inorganic salts

In recent years, the search for eco-sustainable methods has become increasingly urgent, given the economic and environmental impact of traditional industrial processes.[1] In fact, the latter are generally based on a massive use of solvents environmentally problematic, hazardous and energy-demanding during the production, purification and recycling steps. Moreover, solvent-related problems such as solubility and solvolysis often occur, hindering the successful outcome of several syntheses.[2]

Among the eco-sustainable methods stands out the mechanochemical synthesis,[3] a synthetic approach promoted by the input of mechanical energy in the absence (grinding)[4] or with a minimum amount (kneading)[5] of solvent. The mechanochemical method can provide a wide spectrum of materials,[6,7] ranging from metal-organic complexes[8] to novel organic molecules, regardless of the relative solubilities of the starting components.

In this work, we investigate the mechanochemical synthesis of metal-organic complexes through in-situ techniques, i.e. time-resolved X-ray diffraction (XRD) and Raman spectroscopy, which provide real-time information about the solid-state transformations occurring during the milling process. [17,9,10] With the purpose of highlighting the advantages/peculiarities of the solid-state method, the synthesis of these compounds was also performed via slurry in water and from an aqueous solution of the reagents.

The investigated complexes were based on copper(II) and dicyandiamide (DCD), two species extensively used in the agrochemical field. Copper(II) serves the dual purpose of micronutrient[11] and inhibitor towards urease,[12,13] while DCD is supplied to the soil with the aim of inhibiting AMO (see Chapter 2). Co-crystallization of copper and DCD would result in the formation of novel crystalline materials, possibly with combined inhibition activity, and improved stability, solubility and inhibition activity with respect to the free components. In the previous chapter, we have shown that co-crystals of urea mechanochemically synthesized could represent a novel class of fertilizers,[14–16] proving that co-crystallization can be a new promising route for the delivery of agrochemicals.

We selected from CSD database two coordination complexes based on DCD and copper salts, i.e. $[Cu(DCD)2(OH2)2(NO3)2]\cdot 2H_2O$ (refcode DIVWAG) and $[Cu(DCD)_2(OH_2)_2Cl_2]$ (refcode AQCYCU), as models for testing the solid-state processes. The choice fell on these compounds given the lack of information on their synthesis: the paper related to DIVWAG (M. J. Begley, P. Hubberstey, C. H. M. Moore, *J. Chem. Res.* 1985, 378, 4001) is not available, while in the one on AQCYCU there is no reference at all to the synthesis.[17] Moreover, the efficacy of in-situ Raman spectroscopy in monitoring the mechanochemical synthesis of DCD-based coordination compounds has already been proven.[18] To this end, we have attempted the co-crystallization of DCD and copper salts through several methods, as detailed in the next paragraphs. Novel crystalline forms, i.e. $[Cu(DCD)_2(OH2)_2(NO_3)_2]$ and $[Cu(DCD)_2(OH_2)Cl_2]\cdot H_2O$ were synthesized and structurally characterized via solid-state methods: even if such methods do not provide the precise structural information usually obtained from single-crystal X-ray diffraction, here we proved that the integration of several solid-state analysis enables a successful solvent-free methodology.

1

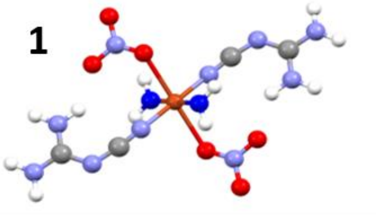

$[Cu(DCD)_2(OH_2)_2(NO_3)_2]$

2

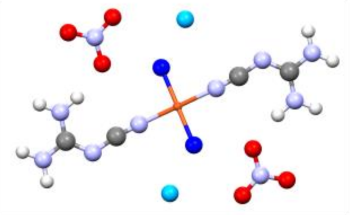

$[Cu(DCD)_2(OH_2)_2][NO_3]_2\cdot 2H_2O$

3

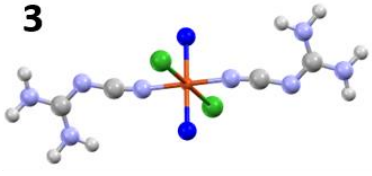

$[Cu(DCD)_2(OH_2)_2Cl_2]$

4

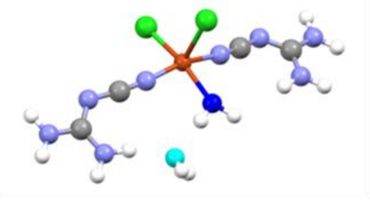

$[Cu(DCD)_2(OH_2)Cl_2]\cdot H_2O$

Compound	Code	Reference	Structure
$[Cu(DCD)_2(OH_2)_2(NO_3)_2]$	**1**	our work	XRPD
$[Cu(DCD)_2(OH2)_2][NO_3]_2·2H_2O$	**2**	DIVWAG	SCXRD
$[Cu(DCD)_2(OH_2)_2Cl_2]$	**3**	AQCYCU	SCXRD
$[Cu(DCD)_2(OH_2)Cl_2]·H_2O$	**4**	our work	XRPD

3.1.1. Materials and methods

Materials. All reagents were purchased from Sigma-Aldrich and used without further purification.

Solid-State Synthesis. Crystalline **2** was synthesized by ball milling in a 2:1 stoichiometry DCD (32.83 mg, 0.40 mmol) and $Cu(NO_3)_2·3H_2O$ (47.17 mg, 0.20 mmol), with the addition of a drop of water, in an agate jar for 60 min at 20 Hz. The same procedure was adopted for the synthesis of the co-crystals **3** (39.73 mg of DCD and 40.27 mg of $CuCl_2·2H_2O$).

Solution Synthesis. Crystalline **2** was obtained through evaporation of a water solution of the reagents DCD (32.83 mg, 0.40 mmol) and $Cu(NO_3)_2·3H_2O$ (47.17 mg, 0.20 mmol). The same procedure was adopted for the synthesis of the co-crystals **3** (39.73 mg of DCD and 40.27 mg of $CuCl_2·2H_2O$).

Slurry Method. Water (ca. 1 mL) was added dropwise to a physical mixture of DCD (0.41 g) and $Cu(NO_3)_2·3H_2O$ (0.58 g) in a 2:1 stoichiometry. When a suspension that could be easily stirred was obtained, the addition of water was interrupted, and the suspension was stirred for 3 days at ambient conditions. Finally, the suspension was filtered and dried, resulting in the compound **1**. The same procedure was employed to prepare **4** starting from a 2:1 physical mixture of DCD and $CuCl_2$ (0.49 g and 0.51 g, respectively).

X-ray Diffraction from Powder. *For phase identification purposes.* X-ray powder diffraction (XRPD) patterns on **1**, **2**, **3** and **4** were collected on a PANalytical X'Pert Pro Automated diffractometer equipped with an X'celerator detector in Bragg−Brentano geometry, using the Cu− Kα radiation (λ = 1.5418 Å) without monochromator in the 5−50° 2θ range (step size 0.033°; time/step: 20 s; Soller slit 0.04 rad, antiscatter slit: 1/2, divergence slit: 1/4 ; 40 mA·40 kV). *For crystal structure resolution from powder diffraction data*. Room temperature X-ray powder diffraction (XRPD) patterns of **1** and **4** were collected on a PANalytical X'Pert PRO automated diffractometer with transmission geometry equipped with Focusing mirror and Pixcel detector in the 2θ range 3–70° (step size 0.0130°, time/step 118.32 s, VxA 40kV x 40mA). Data analyses were carried out using the PANalytical X'Pert Highscore Plus program. The identity of the bulk materials obtained via solid-state processes was always verified by comparing calculated and observed powder diffraction patterns. *Variable temperature X-ray diffraction.* X-ray powder diffractograms in the 2θ range between 3° and 50° were collected on a PANalytical X'Pert PRO automated diffractometer equipped with an X'Celerator detector and an Anton Paar TTK 450 system for measurements at controlled temperature. Data were collected in open air in Bragg–Brentano geometry using Cu-Kα radiation without a monochromator. Thermal programs were selected on the basis of thermogravimetric measurement results.

Structural Characterization from Powder Data. Powder diffraction data for **1** and **4** were analyzed with the software PANalytical X'Pert HighScore Plus. Unit cell parameters were found using DICVOL4 algorithm. Both structures were solved via simulated annealing, performed with EXPO2014 (**1** in the space group P-1 and **4** in the space group $P2_1/c$). Ten runs for simulated annealing trials were set, and a cooling rate (defined as the ratio Tn/Tn-1) of 0.95 was used. In both cases the best solution was chosen for Rietveld refinement, which was performed with the software TOPAS5.0. A shifted Chebyshev function with 8 parameters and a Pseudo-Voigt function were used to fit background and peak shape, respectively. All the hydrogen atoms were fixed in calculated positions with the software Mercury. Rietveld refinements for both the structures are collected in the Supporting Information.

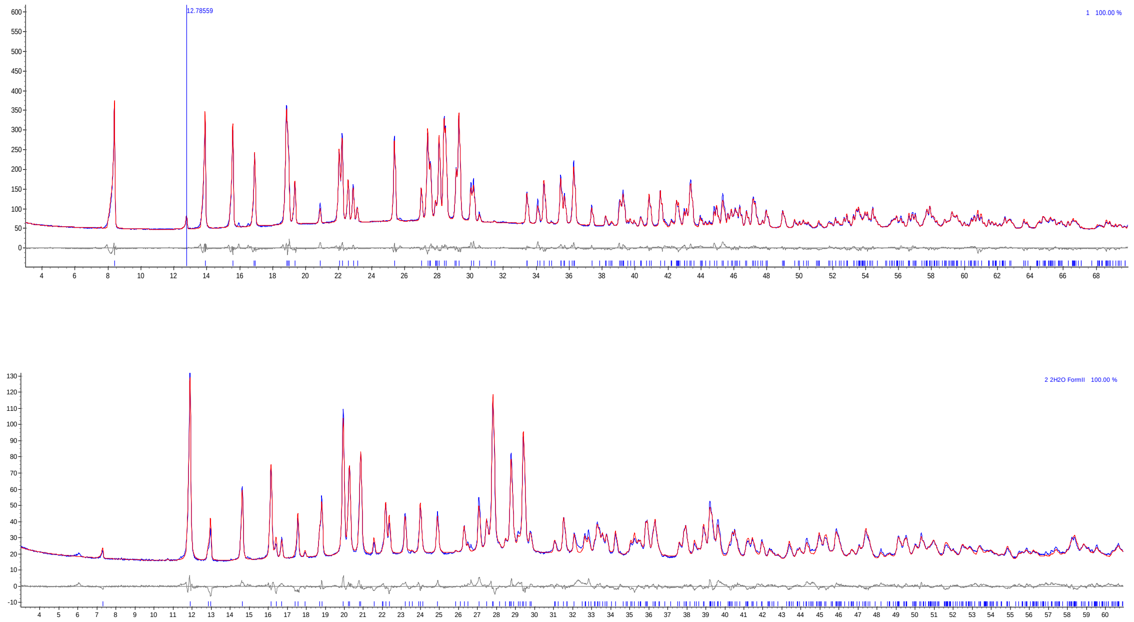

Experimental (blue curve), calculated (red curve) and difference (grey curve) powder patterns for **1** (up) and **4** (bottom). The peak marked in blue is due to an excess of DCD.

	1	**4**
a (Å)	10.822(1)	13.138(3)
b (Å)	6.931(7)	9.424(8)
c (Å)	5.156(1)	10.967(7)
α (°)	67.235(1)	90
β (°)	102.797(1)	113.063(1)
γ (°)	99.693(1)	90
V(Å^3)	346.32	1249.54
S.G.	P-1	P2$_1$/c
Rwp	7.14%	6.4%
Rp	5.44%	8.3%

Table: cell parameters for **1** and **4**

Differential Scanning Calorimetry (DSC). DSC traces were recorded with a PerkinElmer Diamond differential scanning calorimeter. All samples (ca. 10 mg of DCD, **1**, **2**, **3** and **4**) were placed in open Al-pans. All measurements were conducted in the 40−200 °C temperature range, at a heating rate of 5.00 °C min^{-1}.

Thermogravimetric Analysis (TGA). TGA measurements for all samples (ca. 10 mg of DCD, **1**, **2**, **3** and **4**) were performed using a PerkinElmer TGA7 thermogravimetric analyzer, in the 30−300 °C temperature range, under a N_2 gas flow at a heating rate of 5.00 °C min^{-1}.

In situ Raman spectroscopy. Raman measurements were performed on a Raman RXN1TM analyzer (Kaiser Optical systems, France). A non-contact probe head with a working distance of 6 cm (spot size = 1 mm) and an excitation wavelength of λ = 785 nm was used for the collection of Raman spectra every 30 s. For every measurement, five spectra with an acquisition time of 5 s were accumulated.

In situ Synchrotron X-ray diffraction. In situ X-ray diffraction measurements were performed every 30 s at the µSpot beamline (BESSY II, Helmholtz Centre Berlin for Materials and Energy). The experiments were conducted with a wavelength of 1 Å using a double crystal monochromator (Si 111).[9] The obtained scattering images were processed via an algorithm of the program FIT2D.[19] The resulting X-ray diffraction patterns (2θ vs intensity) with λ = 1 Å were corrected for background and plotted using EVA (Bruker AXS, Karlsruhe Germany).

3.1.2. Results and discussions

The co-crystallization of DCD with $Cu(NO_3)_2{\cdot}3H_2O$. Through the simultaneous combination of in-situ time-resolved X-ray diffraction (XRD) and Raman spectroscopy, we monitored the mechanochemical co-crystallization of DCD and $Cu(NO_3)_2{\cdot}3H_2O$ at the molecular and crystalline level. As shown in fig.1, the peaks attributable to the reagents are nearly undetectable and the standard compound **2** (DIVWAG) is already formed at the time 0. Interestingly, after 30 minutes appears a new crystalline phase, and the transformation is completed after 1 hour.

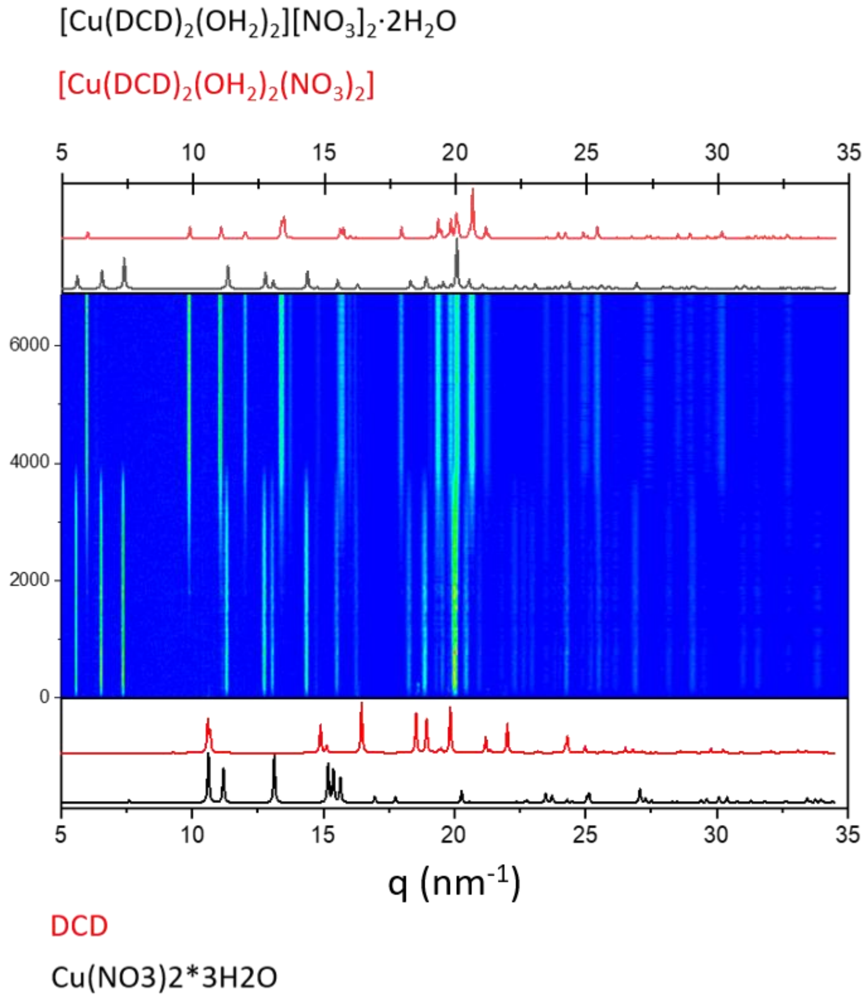

Fig.1: 2D plot of the recorded diffractograms *vs* time (s).

The course of the mechanochemical reaction is also well detectable through in-situ Raman spectroscopy, by following the changes on the frequency of N-C≡N asymmetric stretching of DCD (Fig.2).[20] After a few seconds, the bands of pure DCD (2160 cm^{-1}) and DIVWAG (2220 cm^{-1}

and 2280 cm^{-1}) are active, then the band of pure DCD disappears simultaneously with the increase in the intensities of DIVWAG bands. Finally, the appearance of the new crystalline phase occurs with a new band at 2250 cm^{-1}, whose intensity increases during the reaction.

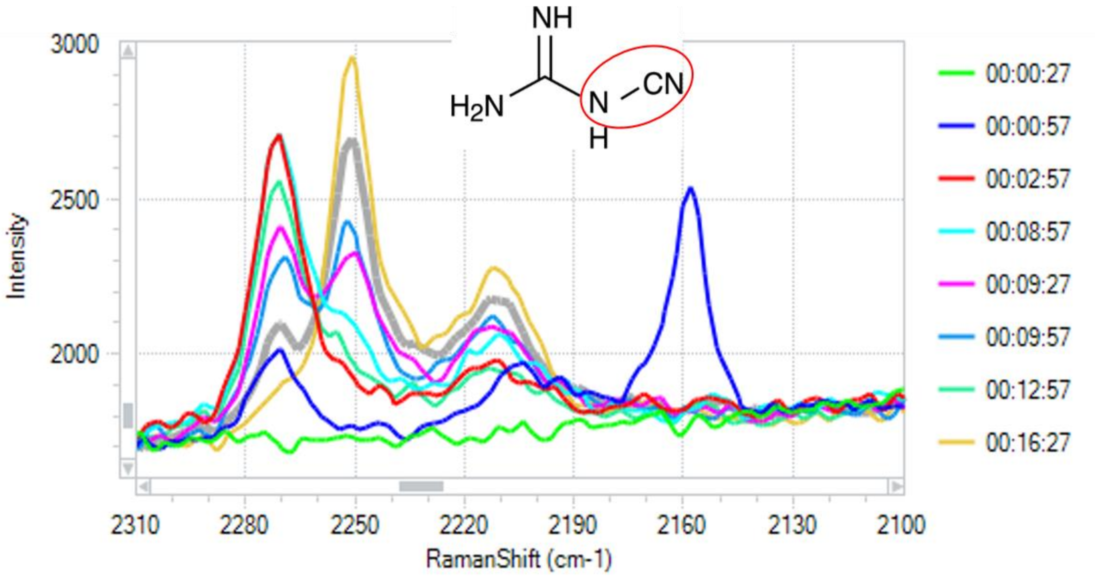

Fig.2: recorded Raman spectra over time.

A further solid-state investigation led to a full understanding of the relationship between the two crystalline phases, which helped in the crystal structure resolution of the new phase from powder diffraction data.

Figure 3a shows the main packing feature of crystalline **2** (refcode DIVWAG): the copper ion is in a square planar geometry, with two water molecules and the N$_{imino}$ atoms belonging to DCD molecules at opposite vertices of the square. DCD is organized in hydrogen bonded dimers, which are bridged by two coplanar nitrate groups involved in bifurcated interactions of N-H$_{DCD}$···O^{-} type. When comparing the crystal packing of **2** with that of DCD (refcode CYAMPD02), it can be seen that in pure DCD all molecules form hydrogen bonded dimers, resulting in each dimer interacting with four dimers arranged perpendicularly to the dimer plane (Fig.3b). The main difference arises then from the mutual orientation of the DCD dimers, which lie in the same plane for the compound **2**, resulting in the formation of a flat layer: the overall crystal packing can be described as a layered structure, with the parallel layers connected to each other via hydrogen bonds between the water molecules (Fig.4). The crystal packing of this compound was found to rely on the second coordination sphere interactions, which are typically weak, but can have significant effects on the crystal arrangement.

By heating the sample up to 80 °C, the removal of the two non-coordinated water molecules deeply affects the crystal structure, resulting in the formation of a new crystalline phase - the same that occurred during the mechanochemical synthesis: the dihydrated compound **1** (Fig.5). The TGA trace for **2** (Fig.6a) reveals such event, showing two weight losses, one between 60-80 °C and the second between 100-120 °C: it confirms the stepwise nature of the dehydration process, involving first the water molecules on the second coordination sphere, then the water molecules coordinated to the copper cation. TGA trace of **1**, on the contrary, shows just one event attributable to the loss of the coordinated water molecules, confirming the dihydrated nature of the compound (Fig.6b).

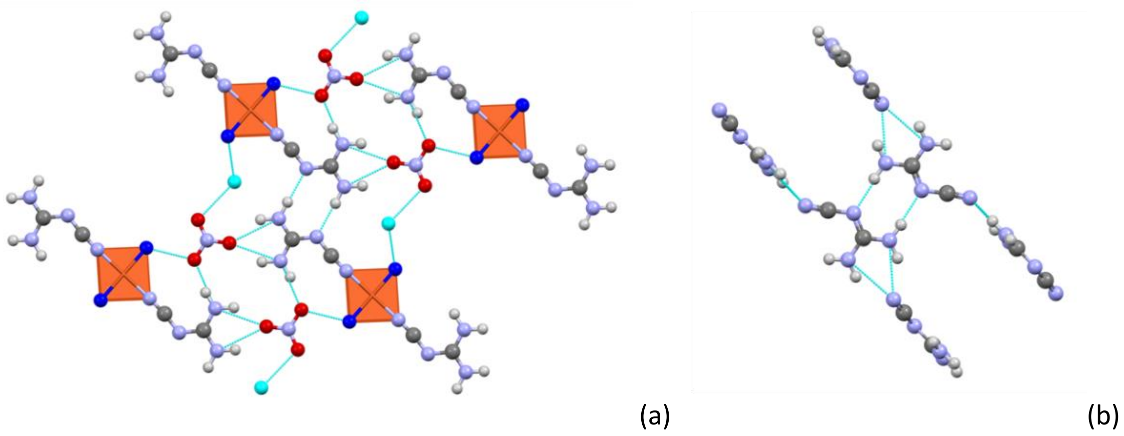

Fig.3: (a) The main packing feature in crystalline **2**: dicyandiamide is organized in hydrogen-bonded dimers (left) – (b) as in its pure crystal (right) - which are bridged by nitrate groups.
[C atoms in grey, N atoms in light blue, H atoms in light grey, O atoms in nitrate in red, O atoms in the first coordination sphere in blue and O atoms in the second coordination sphere in cyan].

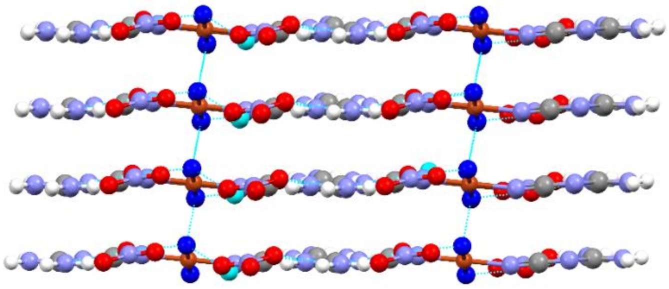

Fig.4: layered structure of **2**.

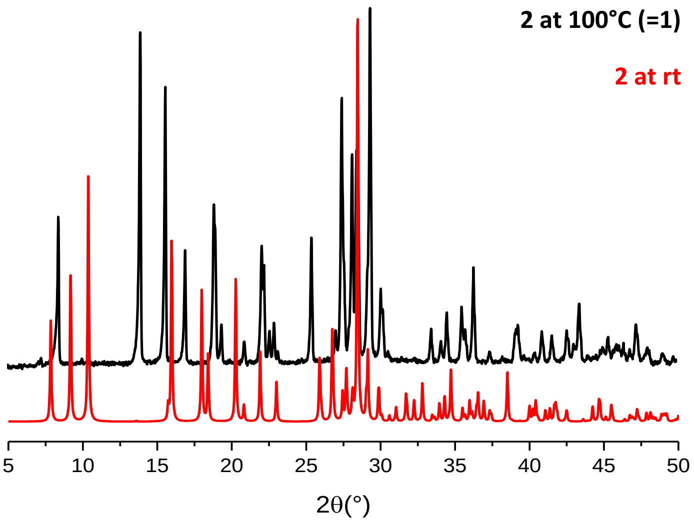

*Fig.5***:** comparison between DIVWAG at 100°C (**1**, black line) and DIVWAG a rt (**2**, red line).

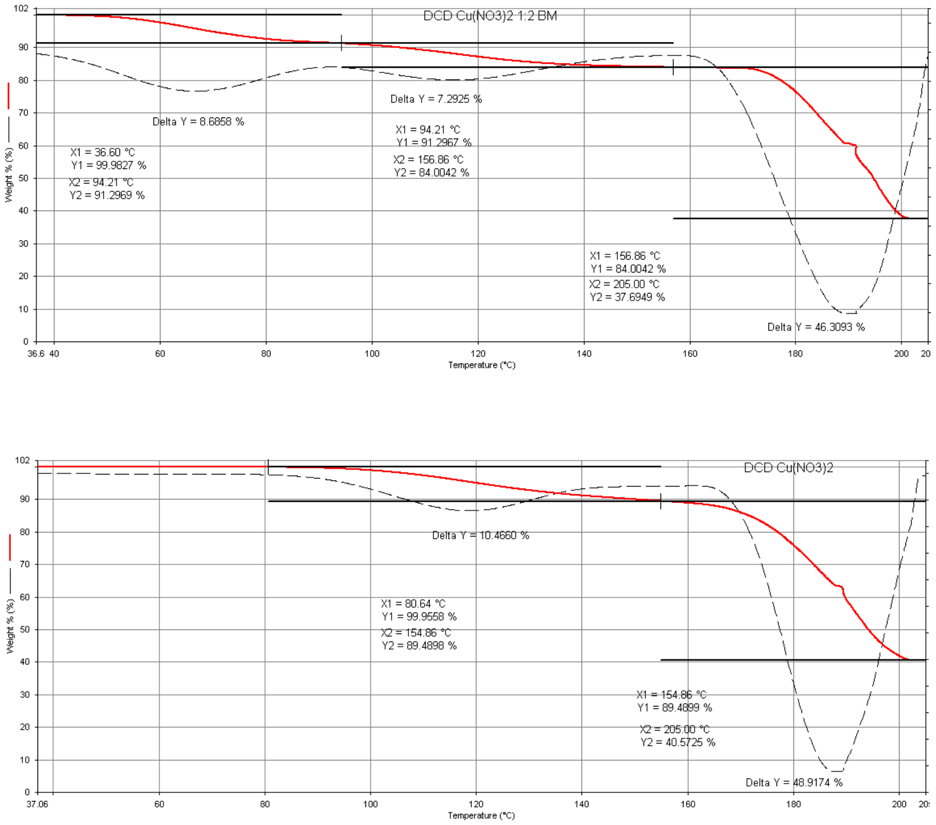

Fig.6: TGA for (up) **2** and (bottom) **1.**

As shown in Fig.7a, in the new crystalline phase the copper ion switched from being tetra-coordinated to be hexa-coordinated, with the nitrate groups entering in the first coordination sphere: copper(II) is in a tetragonally elongated octahedral geometry, typical of Jahn-Teller distorted d^9 systems, with strongly bonded N-donor [Cu-N$_{DCD}$ 1.909 Å] and O-donor [Cu-O$_{water}$ 2.021 Å] ligands in the equatorial sites and weakly bonded nitrates [Cu-N$_{nitrate}$ 2.486 Å] in the axial sites. Contrary to what was previously observed, DCD is still organized in hydrogen bonded dimers, but with the nitrate anions, which act as hydrogen bond acceptors of the double N-H$_{DCD}$ donor [N-H$_{DCD}$···O^{-} 2.924 Å and 3.068 Å]. Such crystal arrangement is consistent with data in the CSD database: among the 7 structures containing DCD and nitrate, only DIVWAG does not display this kind of interaction. Similar to **2**, such arrangement results in the formation of parallel layers of the dimers, connected to each other via the water molecules [C-N$_{DCD}$···H-O$_{water}$ 2.839 Å and N-O$^{-}_{nitrate}$···H-O$_{water}$ 2.815 Å]. However, given the octahedral distorted geometry of the bridging copper ion, the overall crystal packing is best described as a ribbon-like structure (Fig.7b).

The structural identity between the experimental product and the calculated crystal structure was verified by comparing the experimental X-ray powder diffraction pattern (XRPD) and the calculated one (Fig.8), which confirmed the reliability of the model.

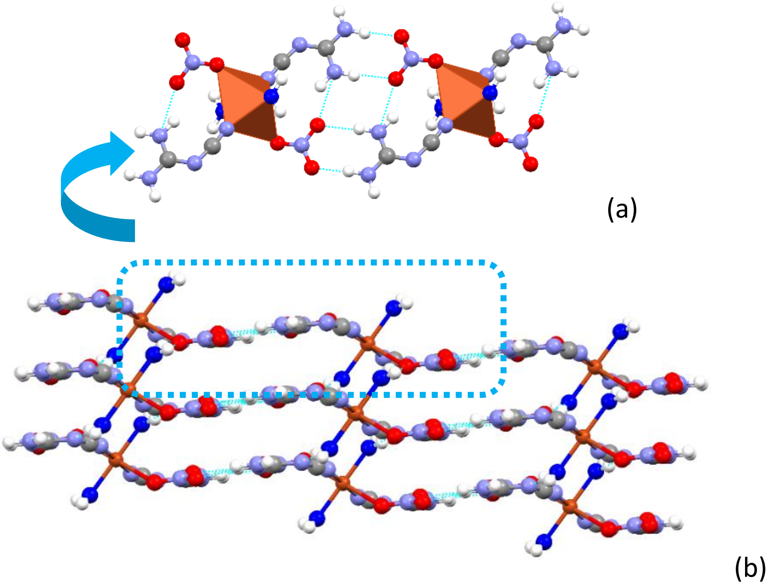

Fig.7: (a) bridging intermolecular dimer and (b) layered crystal packing for **1.**

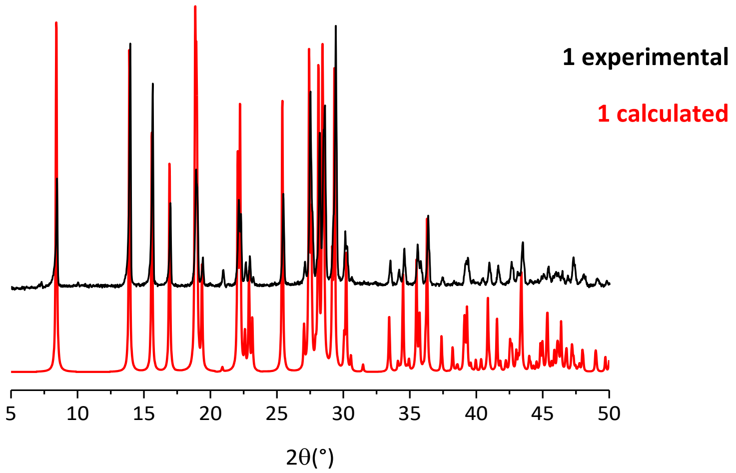

Fig.8: Comparison between experimental (black line) and calculated (red line) diffractrograms for **1**.

To get a better understanding of the relative stability of these two compounds, we performed further mechanochemical syntheses by changing parameters such as the water content or the milling frequency. Preliminary results - here not reported - show that the pure phase **1** is generally obtained through the intermediate **2**, with a kinetic that depends on the water amount. Moreover, it seems possible to direct the reaction towards the pure phase **2** using an excess of water.

Form **1** was obtained by slurry, while the synthesis from solution predominantly yielded the phase **2.** All these data may suggest that the dihydrated form is the most stable one - but further experimental investigation is needed, possibly assisted by computational calculations.

The co-crystallization of DCD with $CuCl_2 \cdot 2H_2O$. The mechanochemical synthesis of the tabulated compound AQCYCU was monitored through in-situ time-resolved X-ray diffraction (XRD) and Raman spectroscopy. Fig.9 shows that the formation of the expected compound is quite fast - it is not even possible to detect the peaks attributable to the reagents. Interestingly, also a second crystalline phase seems to concomitantly occur in the first seconds.

With regard to the in-situ Raman spectroscopy, it was not possible to follow the reaction: data should be recorded again with a shorter acquisition time. However, it is possible to unambiguously assign the bands at 2250 cm^{-1} and 2220 cm^{-1} to the asymmetric stretching of N-C≡N of the coordinated DCD molecules, as previously seen for **1**.

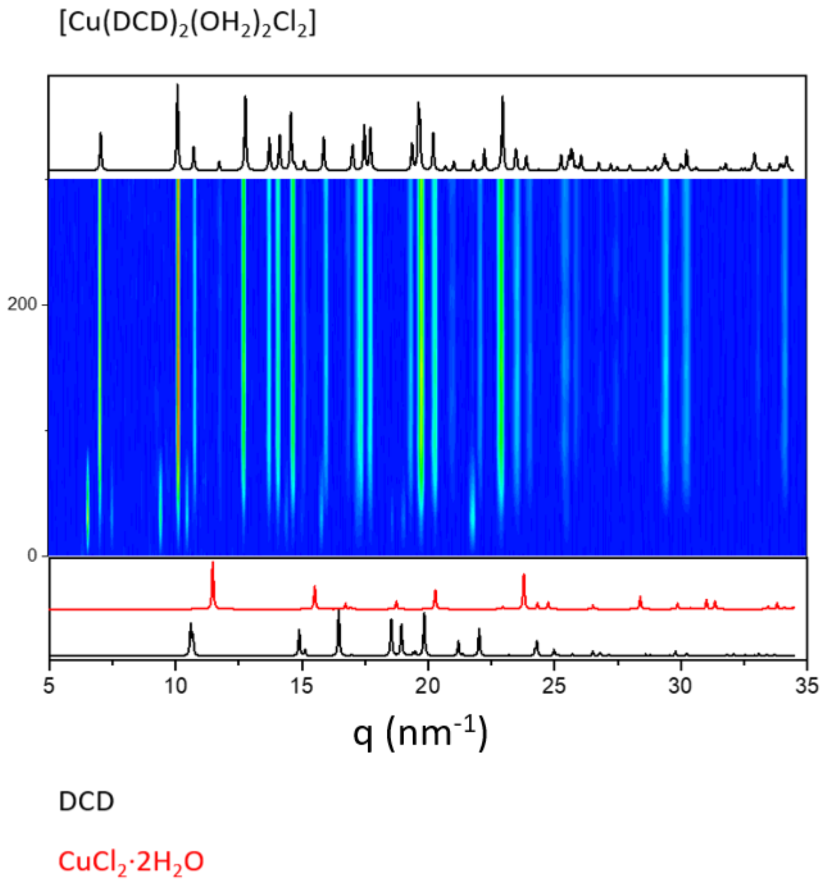

Fig.9: 2D plot of the recorded diffractograms *vs* time (s).

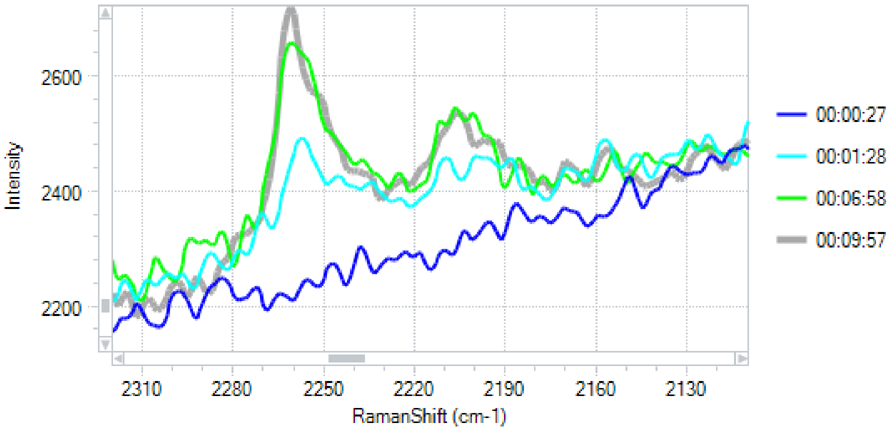

Fig.10: recorded Raman spectra over time.

Co-crystallization of DCD with $CuCl_2·2H_2O$ was then conducted from a water solution of the reagents: a physical mixture of both the phases - AQCYCU and the intermediate compound - were obtained (Fig.11). However, single crystals of the intermediate compound did not grow, therefore it was not possible to determine its crystal structure through single crystal X-ray diffraction (*the crystal structure resolution from powder diffraction data is in progress*).

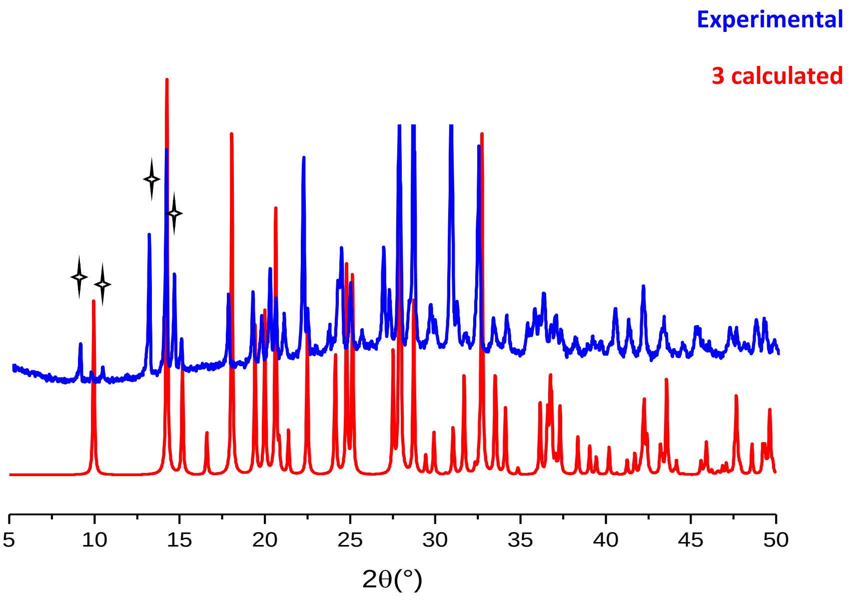

Fig.11: Comparison between experimental (solution product, blue line) and calculated (red line) for **3** (AQCYCU). The extra-peaks are attributable to the unexpected compound.

Finally, it was performed the synthesis from slurry, which surprisingly provided another different phase - a polymorph of AQCYCU. The polymorphic relationship between the two structures was confirmed by thermal analysis: TGA and DSC profiles pointed out that in both the cases the systems loss two water molecules starting from 60°C (Fig.12 and Fig.13). By heating the samples up to 80 °C, they convert into the same anhydrous phase (Fig.14), which then degrades starting from 160 °C.

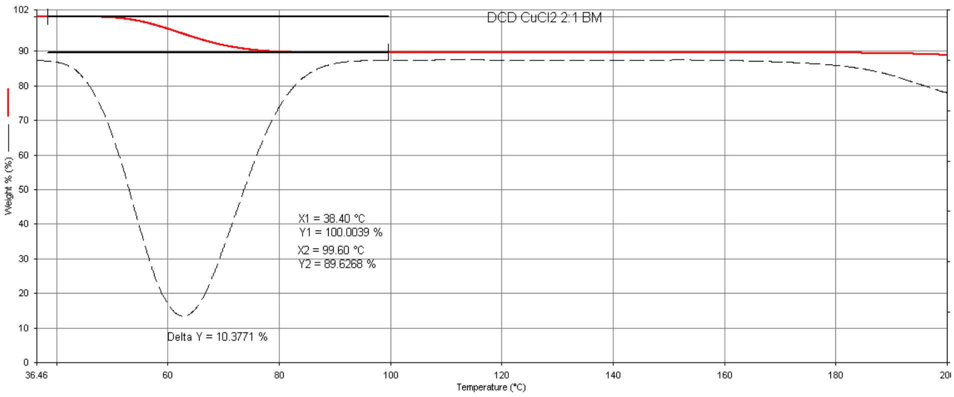

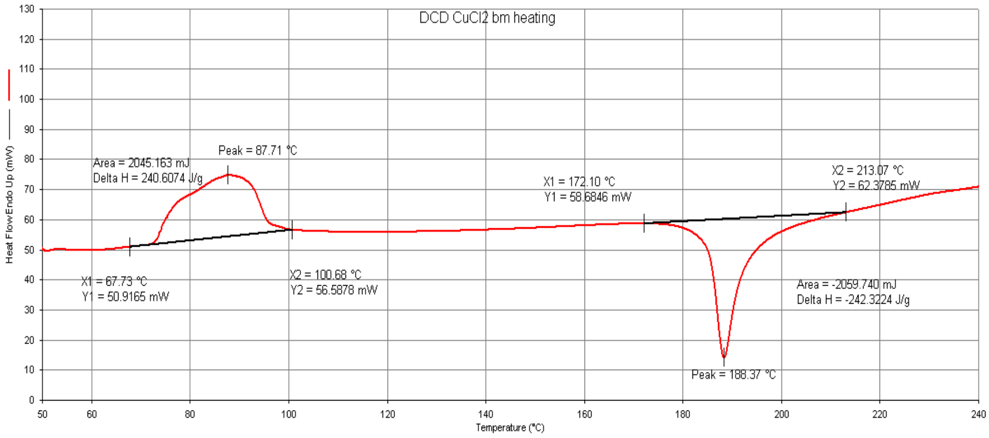

Fig.12: TGA (up) and DSC (bottom) traces for **3.**

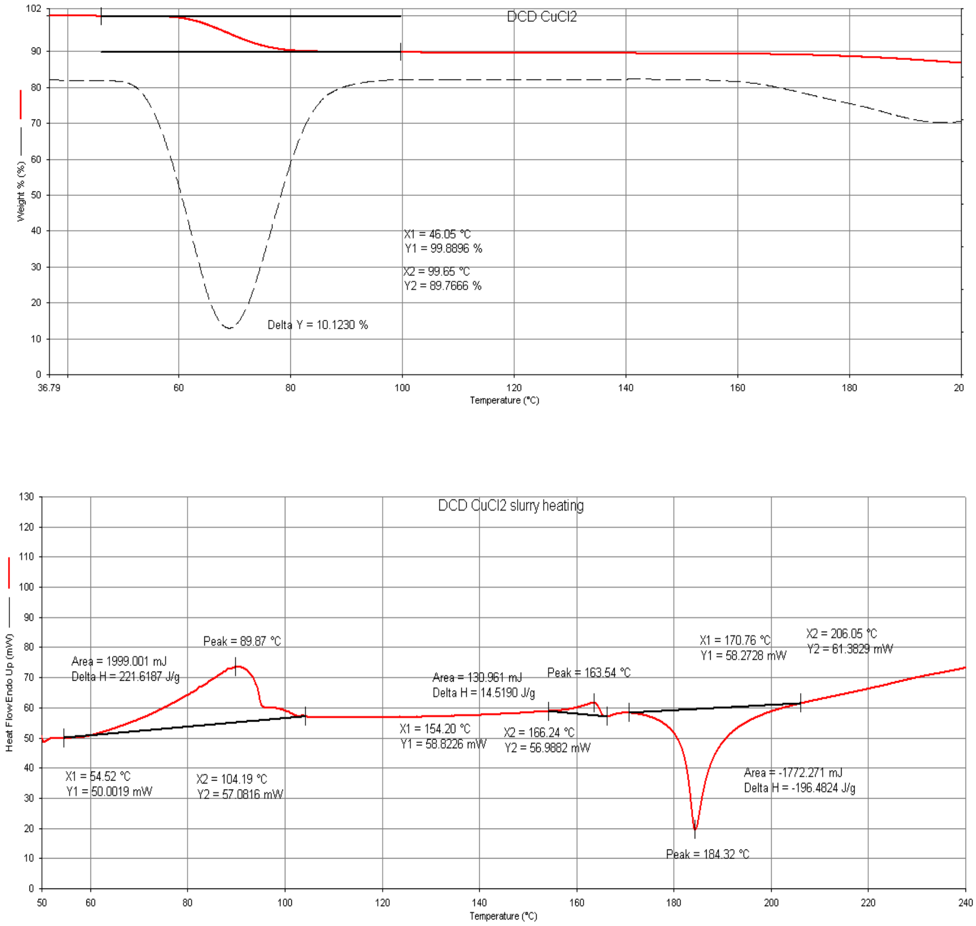

Fig.ESI 9: TGA (up) and DSC (bottom) traces for **4.** The latter present an extra peak due to an impurity.

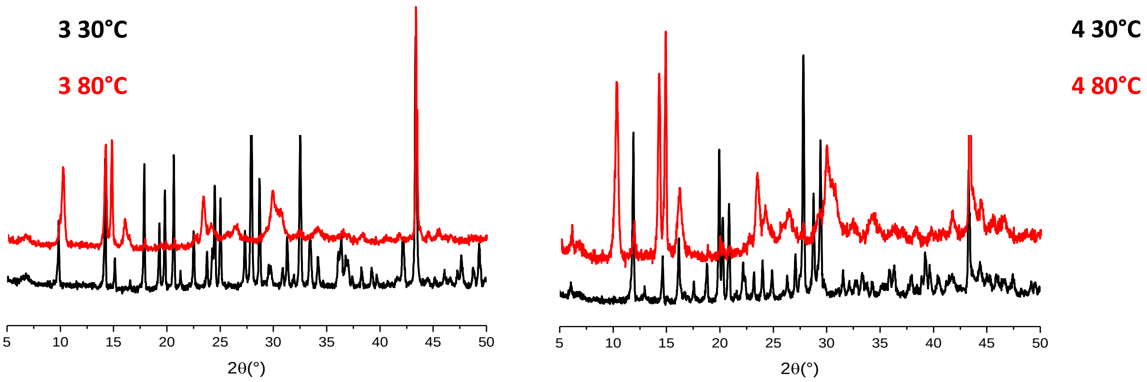

Fig.14: diffractograms recorded at room temperature (black line) and 80 °C (red line) for **3** (left) and **4** (right).

In **3** (refcode AQCYCU), the coordination geometry of the copper atom, which is located on an inversion centre, is that typical of Jahn-Teller distorted octahedral systems, as previously observed for **1**: copper is surrounded equatorially by two monodentate DCD molecules and two water molecules, and axially by two chloride anions. Contrary to what seen above, the main packing feature of **3** relies on the charge-assisted hydrogen bonds between the chloride anions and the NH groups on DCD molecules, resulting in the formation of alternating layers of DCD molecules and copper ions (Fig.15).

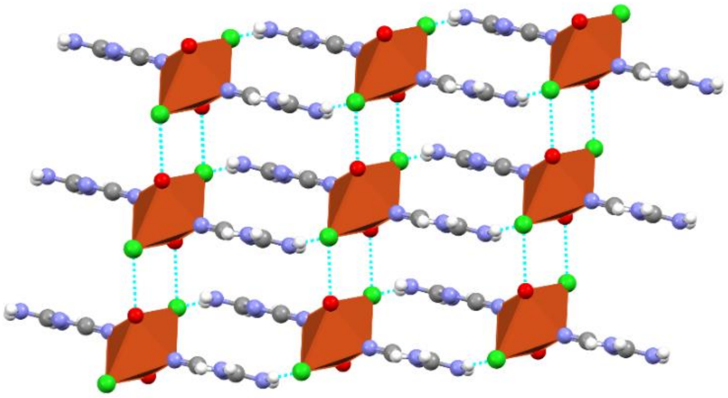

Fig.15: Crystal packing for compound **3.**

[C atoms in grey, N atoms in light blue, H atoms in white, O atoms in red and Cl atoms in green].

The main difference between the structures of the two polymorphs resides in the coordination geometry around the Cu^{2+} cation, which changes from octahedral in the triclinic phase **3** to square pyramidal in the monoclinic phase **4**.

In **4**, copper is coordinated by two DCD ligands, one water molecule and a chloride anion, while axially by a second chloride anion. The asymmetric unit contains also a second water molecule, which is not coordinated to the copper ion (Fig.16a) The crystallographically independent DCD molecules are involved in different hydrogen bond networks: one of the molecules is hydrogen bond acceptor of the non-coordinated water [$C\text{-}N_{DCD}\cdots H\text{-}O_{water}$ 2.783 Å], while the second molecule is hydrogen bond donor toward the non-coordinated water molecule [$N\text{-}H_{DCD}\cdots O_{water}$ 2.928 Å] and two chloride anions in equatorial position [$N\text{-}H_{DCD}\cdots Cl^-$ 3.211 Å and 3.257 Å]. The chloride anion in the axial position is instead the hydrogen bond acceptor of the coordinated water molecule [$O\text{-}H_{water}\cdots Cl^-$ 3.211 Å]. All these interactions result in the formation hydrogen bonded wavy chains, which are held together by hydrogen bonds between the axial chloride anions and the coordinated water molecule, giving rise to a ribbon-like structure (Fig.16b).

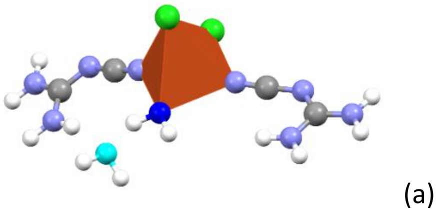

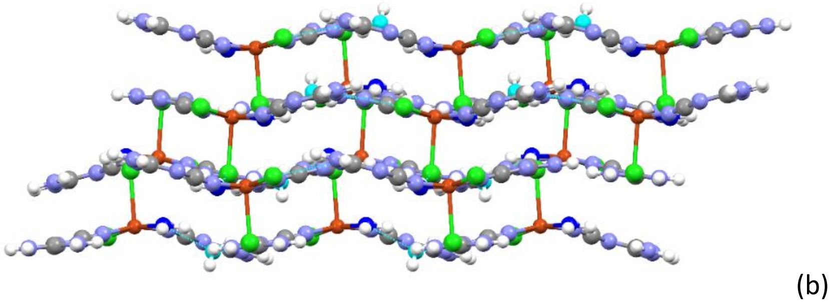

Fig.16: Crystal packing of **4** via hydrogen bonded zig-zag chains.

[C atoms in grey, N atoms in light blue, H atoms in white, O atoms in cyan and Cl atoms in green].

The X-ray powder diffractogram calculated on the basis of the powder diffraction data corresponds to the experimental one (Fig.17), suggesting that the model is correct.

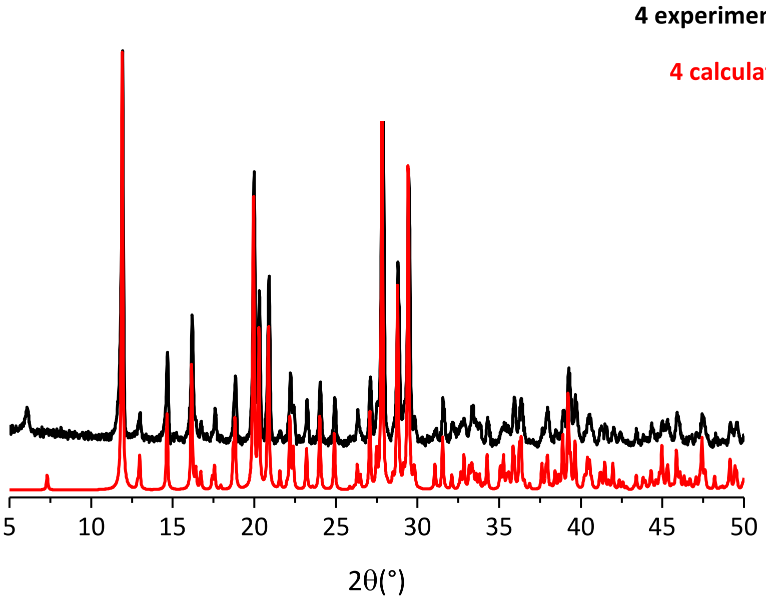

Fig.17: comparison between the experimental diffractogram (black line) and the calculated diffractogram (red line) for **4.**

Further investigation on the mechanochemical reaction between DCD and $CuCl_2$ - *currently in progress* - could represent an additional step in the understanding of the solid-state reactivity of these compounds. The variation of the milling conditions, such as water amount or frequency, may in fact drive to the appearance of one crystalline phase over the others or to more phases concomitantly. These experiments, along with computational calculations, could provide more information about the thermodynamic stability of these compounds.

3.2 β-CD-nitrapyrin: a novel prototype of AMO inhibitors

With the global agricultural production ever-expanding, the quest for a sustainable soil fertilization and crop productivity is all the more necessary.[21] In fact, at the present day approximately 50% of nitrogen fertilizer applied to the soil is lost to the environment instead of being utilized by the plants. The N loss is mainly due to the activity of the enzymes contained in the soil, such as ammonia monooxygenase (AMO), which is responsible for the oxidation of NH_4^+ to hydroxylamine (NH_2OH), a key process in the production of greenhouse gases such as NH_3, NO, N_2O.[22] Given the awful economic, agronomic and environmental consequences arising from the oxidation process, the current agrochemical formulations are aimed to increase N use efficiency by suppling AMO inhibitors to the soil.[23]

Nitrapyrin (NP) (Fig.1) is an AMO inhibitor extremely effective, which acts even at the nM range. However, it is characterized by a high vapor pressure, so it is generally incorporated into the soil via injection - at a depth of at least 5 to 10 cm - and preferably in cold-climate countries.[24] NP presents then a pretty low versatility, which dramatically limits its use and potential.

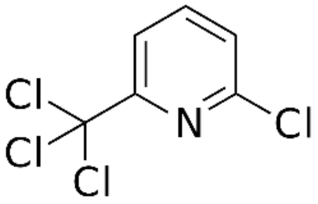

Fig.1: nitrapyrin

In this work, we attempted the stabilization of NP through crystal engineering methods. NP turned out to be a low-reactive molecule, therefore any co-crystallization/salification effort was unsuccessful. Given the hydrophobicity of such compound, we decided to test its reactivity with β-CD, which is known to form inclusion complexes mainly by exploiting the hydrophobic effect,[25] while being at the same time unharmful for health and environment and not expensive.

β-CD belongs to the family of cyclodextrins, cyclic oligosaccharides with glucose units - 6 (α-cyclodextrins), 7 (β-cyclodextrins) or 8 (γ-cyclodextrins) - bonded via α-1,4 glycosidic bonds (Fig.2). They possess a hydrophobic cavity - able to include apolar guests - and a hydrophilic surface, which makes them/the included compounds soluble in water.[26] Through the preparation of β-CD inclusion complexes is then possible to (1) improve the water solubility/stability of the guest molecules, (2) perform a controlled release of the included molecules and (3) increase the bio- and eco-compatibility of the guest molecules. As a result of these properties, β-CD has been widely employed as drug carrier in the pharmaceutical field,[27] as well as in food industry and in the environmental sciences. Interestingly, although the preparation of β-CD inclusion complexes with agrochemicals is already reported,[28] there are no studies concerning the stabilization of AMO inhibitors by inclusion into β-CD cavity.

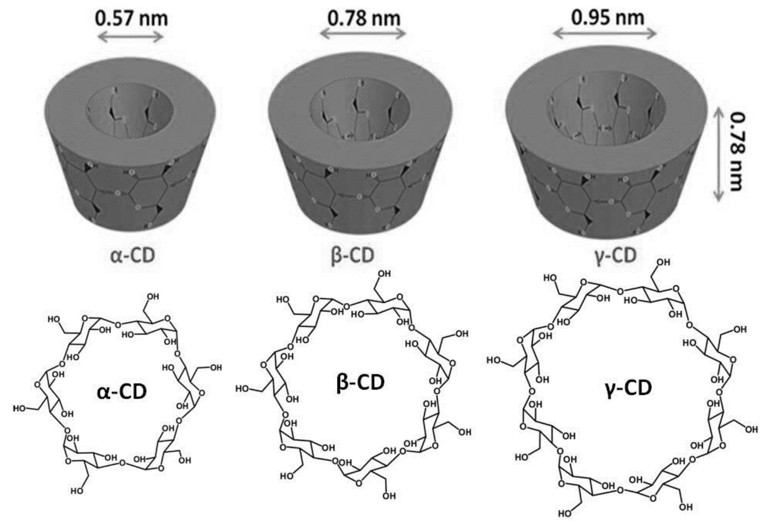

Fig.2: scheme of α, β, γ cyclodextrins.

In this work we investigated the mechanochemical synthesis of the inclusion complex β-CD-NP. The compound was then characterized by a combination of techniques, including X-ray diffraction (XRD), thermogravimetric analysis (TGA) and solution NMR. *Further analyses - such as solid-state NMR, Raman spectroscopy and crystal structure resolution from powder diffraction data - are still in progress (at BAM research centre) and are not reported here.* Along with the complex, also pure NP was characterized in the solid-state.

Finally, the inhibition activity of the complex was evaluated - thanks to the collaboration with the research group of prof. Stefano Ciurli at the University of Bologna- and found to be as effective as that of the unprotected molecules. Moreover, since the current methodologies for the evaluation of the inhibition activity are all water-based, the utilization of β-CD inclusion complexes is even more revolutionary: the included molecules are now water-soluble, therefore also the apolar compounds can be investigated.

3.2.1 Experimental conditions

Materials. All reagents were purchased from Sigma–Aldrich and used without further purification. Double distilled water and reagent grade solvents were used. All solid materials were preliminarily screened for chemical and crystal phase purity via XRPD analysis.

Synthesis. The inclusion complex B-CD-NP was obtained by ball milling β -CD·8H_2O (89.44 mg, 0.068 mmol) and NP (10.55 mg, 0.034 mmol), with the addition of a few drops of water, for 120 min at 20 Hz in an agate jar.

X-ray Diffraction. *Single Crystal X-ray diffraction*. Single-crystal data for pure NP were collected at RT with an Oxford XCalibur S CCD diffractometer equipped with a graphite monochromator (Mo-Kα radiation, λ = 0.71073 Å). The structure was solved by intrinsic phasing with SHELXT[5] and refined on F^2 by full-matrix least squares refinement with SHELXL implemented in the Olex2 software.[6] All non-hydrogen atoms were refined anisotropically. The program Mercury[29] was used to calculate the powder patterns from single crystal data and for molecular graphics.

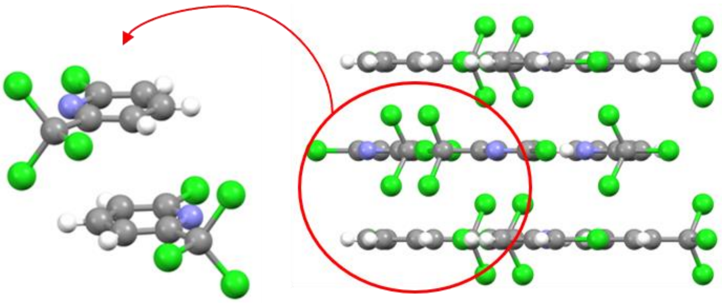

S.G.	a (Å)	b (Å)	c (Å)	β (°)	V (Å)^3
P21/m	9.0327(4)	7.2075(6)	13.7485(6)	102.079(4)	875.25(9)

Powder X-ray diffraction for phase identification purposes. XRPD pattern of B-CD-NP was collected on a PANalytical X´Pert Pro Automated diffractometer equipped with an X´celerator detector in Bragg-Brentano geometry, using Cu-Kα radiation (λ = 1.5418 Å) without monochromator in the 3-40° 2θ range (step size 0.033º; time/step: 20 s; soller-slit 0.04 rad, antiscatter slit: ½, divergence slit: ¼ ; 40 mA, 40kV). The program Mercury[29] was used for simulation of XRPD patterns on the basis of single crystal data retrieved from the CSD.[30] Chemical and structural identity between bulk materials and single crystals was always verified by comparing experimental and simulated powder diffraction patterns. For Pawley refinement purposes, XRPD patterns were collected on a PANalytical X'Pert PRO automated diffractometer with transmission geometry, equipped with Focusing Mirror and Pixcel detector, in the 2θ range 3–70° (step size 0.02608, time/step 200 s, 0.02 rad soller; 40 kV, 40 mA). Powder diffraction data were analysed with the software TOPAS4.1.[31] A shifted Chebyshev function with 8 parameters was used to fit the background.

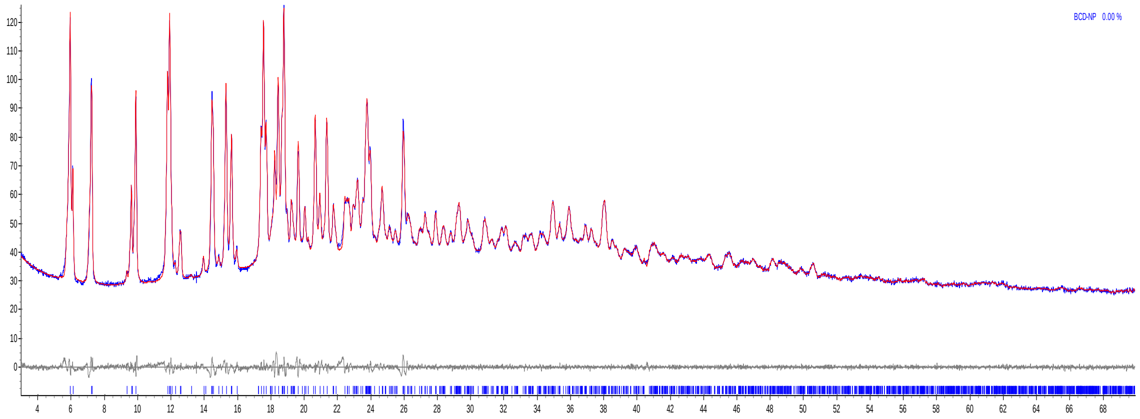

S.G.	a (Å)	b (Å)	c (Å)	β (°)	V (Å)^3	**Rwp**
C2	19.0117	24.4573	15.7788	110.2143	6884.93	**3.387**

In situ Synchrotron X-ray diffraction. In situ X-ray diffraction measurements were performed every 30 s at the µSpot beamline (BESSY II, Helmholtz Centre Berlin for Materials and Energy). The experiments were conducted with a wavelength of 1 Å using a double crystal monochromator (Si 111).[9] For processing of the obtained scattering images an algorithm of the program FIT2D was used.[19] The resulting X-ray diffraction patterns (2θ vs intensity) with λ = 1 Å were background corrected and plotted using EVA (Bruker AXS, Karlsruhe Germany).

^{1}H-NMR Spectroscopy

^{1}H-NMR spectra were recorded on a Varian INOVA 400 (400MHz) spectrometer; the solvent used was D_2O, bought from Sigma-Aldrich. The solution was prepared with the sample mechanochemically synthesized. Chemical shifts are reported in ppm, with tetramethylsilane as internal reference standard.

Thermogravimetric analysis (TGA)

TGA measurements on all samples were performed with a PerkinElmer TGA7 thermogravimetric analyzer, in the 30-400 °C temperature range, under an N_2 gas flow and at the heating rate of 5.00 °C min^{-1}.

Differential scanning calorimetry (DSC)

DSC traces were recorded using a Perkin-Elmer Diamond differential scanning calorimeter. All samples [10 mg of β-CD, NP, β-CD-NP] were placed in open Al-pans. All measurements were conducted in the 40-200 °C temperature range, at the heating rate of 5.00 °C min^{-1}.

3.2.2 Results and discussion

The mechanochemical reaction between β -CD and NP kneaded in a 1:1 stoichiometric ratio was monitored through time-resolved in-situ x-ray diffraction. Fig.2 shows that the formation of a new phase occurs in the first minutes, but that the total conversion of the reagents into the final product takes at least 15 minutes.

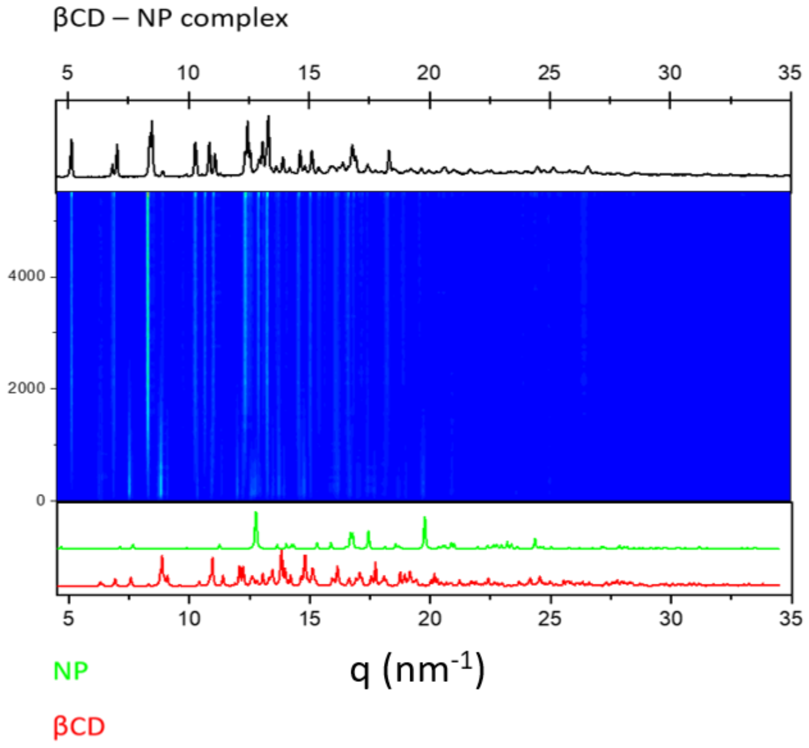

Fig.2: 2D plot of the recorder diffractograms vs time (s) for the mechanochemical reactions between B-CD and NP.

In accordance with the principle of isostructurality stated by Mino Caira,[32] β-CD inclusion complexes crystallize in isostructural series, each with the same packing arrangement and unit cell parameters (see Chapter 4). The experimental PXRD pattern was thus compared with a set of reference patterns for all the isostructural series and found to fall in the C2 isostructural series (see experimental section), which is characterized by a channel-like arrangement of the β-CD molecules.

Proton NMR spectroscopy turned out to be a powerful technique to validate the formation of β-CD inclusion complexes. The NMR spectrum recorded in D_2O reveals the presence of NP, which is soluble in water once inside the β-CD hydrophobic cavity. Moreover, the 1 to 1 stoichiometry of the complex is confirmed, thanks to the intrinsic quantitative character of NMR (Fig.3).

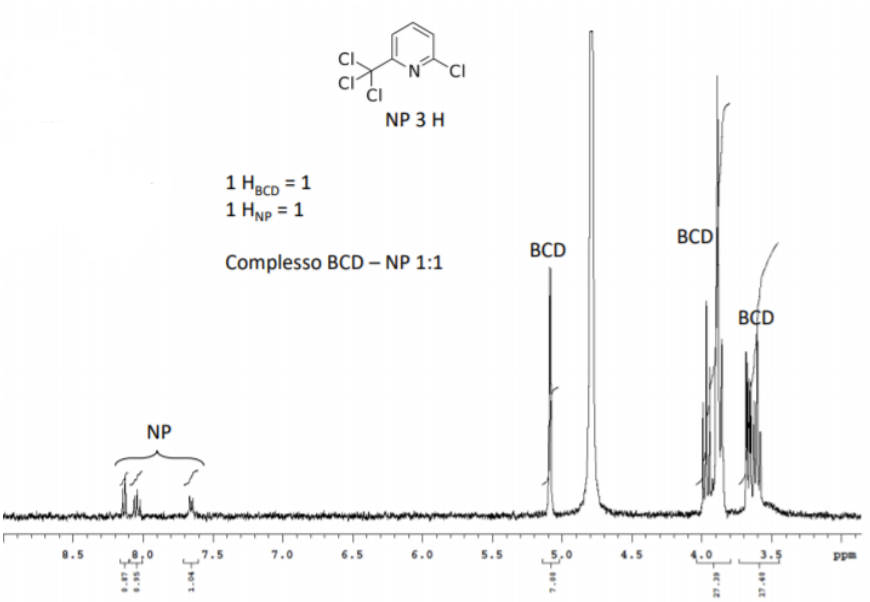

Fig.3: NMR spectrum in D_2O for the complex B-CD-NP.

The TGA analysis provides further evidence of the successful encapsulation of NP and was also employed to evaluate the water content. As shown in fig.4, NP presents a single weight loss in the range 80-180 °C, which is ascribable to its volatility/decomposition. β-CD, instead, loses weight in two distinct steps, related to the dehydration (40-80 °C) and the degradation (300-350 °C). Finally, the complex β -CD-NP presents an intermediate character with the degradation step in the range 250-300° C, preceded by the loss of three water molecules up to 100 °C.

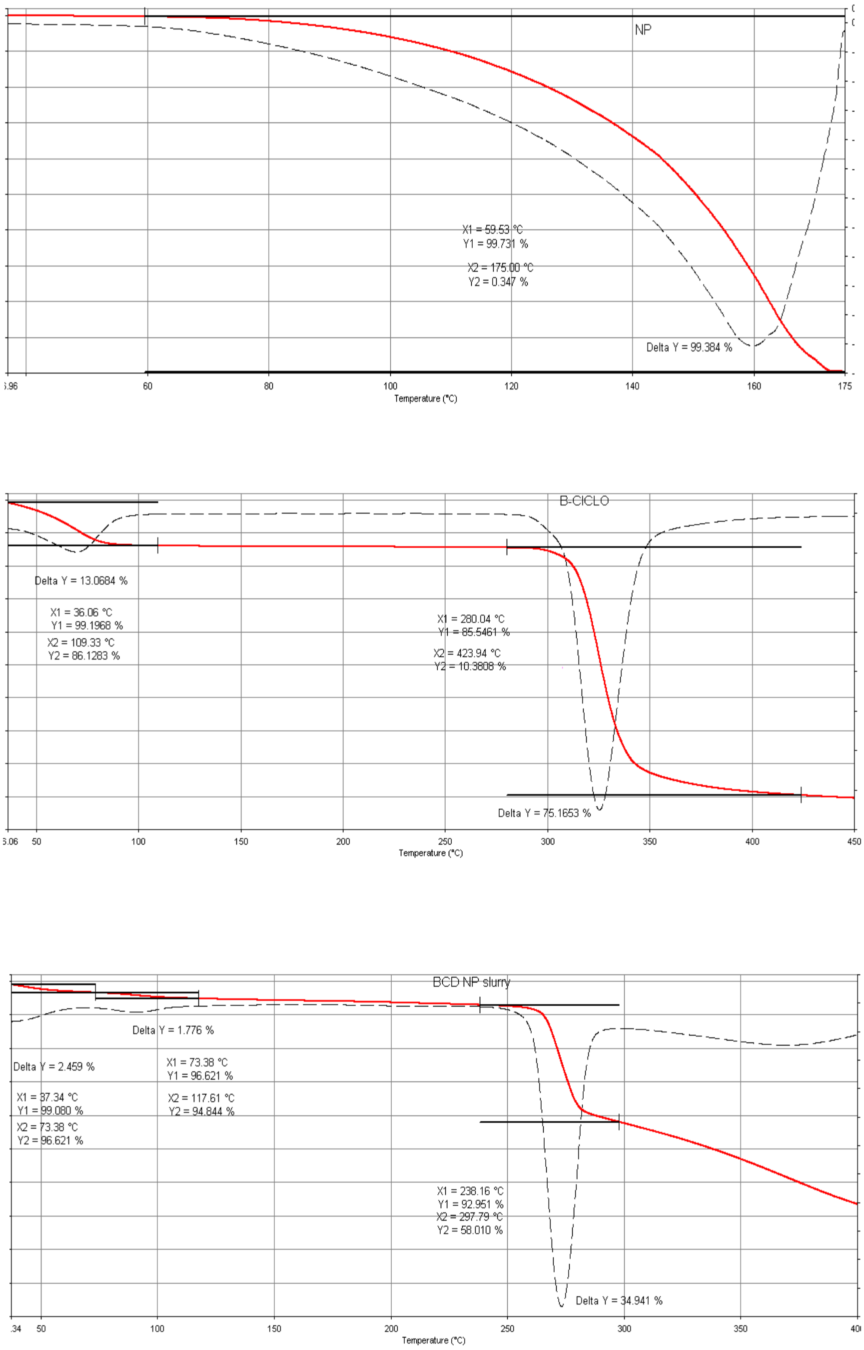

Fig.5: TGA traces for NP (up), B-CD (middle) and B-CD-NP (bottom).

All the performed analysis proved the effective inclusion of NP into β-CD and provided several information concerning the solid-state structure, i.e. the crystal packing, the stoichiometry and the water content. However, further investigation is needed to get an exhaustive information about the crystal structure as well as the intermolecular interactions that occur between the components (*ongoing experiments*).

This study can represent a turning point in the formulation of AMO inhibitors. Through the inclusion of NP into β-CD it is in fact possible to (1) obtain a solid-state formulation of NP, (2) improve the stability of NP, (3) maintain its inhibition capability and (4) increase the water solubility.

References

1. The 41st CIRP Conference on Manufacturing Systems Program & Information. *Program* 8656 (2008).
2. Braga, D., Maini, L. & Grepioni, F. Mechanochemical preparation of co-crystals. *Chem. Soc. Rev.* **42,** 7638–7648 (2013).
3. James, S. L., Adams, C. J., Bolm, C., Braga, D., Collier, P., Frišcic, T., Grepioni, F., Harris, K. D. M., Hyett, G., Jones, W., Krebs, A., Mack, J., Maini, L., Orpen, A. G., Parkin, I. P., Shearouse, W. C., Steed, J. W. & Waddell, D. C. Playing with organic radicals as building blocks for functional molecular materials. *Chem. Soc. Rev.* **41,** 413–447 (2012).
4. Trask, A. V. & Jones, W. Crystal engineering of organic cocrystals by the solid-state grinding approach. *Top. Curr. Chem.* **254,** 41–70 (2005).
5. Friščić, T., Trask, A. V., Jones, W. & Motherwell, W. D. S. Screening for inclusion compounds and systematic construction of three-component solids by liquid-assisted grinding. *Angew. Chemie - Int. Ed.* **45,** 7546–7550 (2006).
6. Gomes, C. S. B., Gomes, P. T. & Duarte, M. T. α-Diimine transition-metal complexes: Mechanochemistry - A new synthetic approach Dedicated to Professor Maria José Calhorda on the occasion of her 65th birthday. *J. Organomet. Chem.* **760,** 101–107 (2014).
7. Quaresma, S., André, V., Fernandes, A. & Duarte, M. T. Mechanochemistry – A green synthetic methodology leading to metallodrugs, metallopharmaceuticals and bio-inspired metal-organic frameworks. *Inorganica Chim. Acta* **455,** 309–318 (2017).
8. André, V., Quaresma, S., Da Silva, J. L. F. & Duarte, M. T. Exploring mechanochemistry to turn organic bio-relevant molecules into metal-organic frameworks: A short review. *Beilstein J. Org. Chem.* **13,** 2416–2427 (2017).
9. Batzdorf, L., Fischer, F., Wilke, M., Wenzel, K.-J. & Emmerling, F. Direct In Situ Investigation of Milling Reactions Using Combined X-ray Diffraction and Raman Spectroscopy. *Angew. Chemie* **127,** 1819–1822 (2015).
10. Klimakow, M., Klobes, P., Thünemann, A. F., Rademann, K. & Emmerling, F. Mechanochemical synthesis of metal-organic frameworks: A fast and facile approach toward quantitative yields and high specific surface areas. *Chem. Mater.* **22,** 5216–5221 (2010).
11. Alloway, B. J. & Tills, A. R. Copper deficiency in world crops. *Outlook Agric.* **13,** 32–42 (1984).
12. Dong, X., Li, Y., Li, Z., Cui, Y. & Zhu, H. Synthesis, structures and urease inhibition studies of

copper(II) and nickel(II) complexes with bidentate N,O-donor Schiff base ligands. *J. Inorg. Biochem.* **108,** 22–29 (2012).

13. Maroney, M. J. & Ciurli, S. Nonredox nickel enzymes. *Chem. Rev.* **114,** 4206–4228 (2014).

14. Casali, L., Mazzei, L., Shemchuk, O., Sharma, L., Honer, K., Grepioni, F., Ciurli, S., Braga, D. & Baltrusaitis, J. Novel Dual-Action Plant Fertilizer and Urease Inhibitor: Urea·Catechol Cocrystal. Characterization and Environmental Reactivity. *ACS Sustain. Chem. Eng.* **7,** 2852–2859 (2019).

15. Casali, L., Mazzei, L., Shemchuk, O., Honer, K., Grepioni, F., Ciurli, S., Braga, D. & Baltrusaitis, J. Smart urea ionic co-crystals with enhanced urease inhibition activity for improved nitrogen cycle management. *Chem. Commun.* **54,** 7637–7640 (2018).

16. Mazzei, L., Broll, V., Casali, L., Silva, M., Braga, D., Grepioni, F., Baltrusaitis, J. & Ciurli, S. Multifunctional urea cocrystal with combined ureolysis and nitrification inhibiting capabilities for enhanced nitrogen management. *ACS Sustain. Chem. Eng.* **7,** 13369–13378 (2019).

17. Chiesi, A., Coghi, L., Mangia, A., Nardelli, M. & Pelizzi, G. The crystal and molecular structure of dichlorodiaquobis(dicyandiamide)copper(II). *Acta Crystallogr. Sect. B Struct. Crystallogr. Cryst. Chem.* **27,** 192–197 (1971).

18. Trukil, V., Fábián, L., Reid, D. G., Duer, M. J., Jackson, G. J., Eckert-Maksić, M. & Friić, T. Towards an environmentally-friendly laboratory: Dimensionality and reactivity in the mechanosynthesis of metal-organic compounds. *Chem. Commun.* **46,** 9191–9193 (2010).

19. Hammersley, A. P., Brown, K., Burmeister, W., Claustre, L., Gonzalez, A., McSweeney, S., Mitchell, E., Moy, J. P., Svensson, S. O. & Thompson, A. W. Calibration and application of an X-ray image intensifier/charge-coupled device detector for monochromatic macromolecular crystallography. *J. Synchrotron Radiat.* **4,** 67–77 (1997).

20. Lin, X., Hasi, W. L. J., Lou, X. T., Han, S. Q. G. W., Lin, D. Y. & Lu, Z. W. Direct and quantitative detection of dicyandiamide (DCD) in milk using surface-enhanced Raman spectroscopy. *Anal. Methods* **7,** 3869–3875 (2015).

21. Prosekov, A. Y. & Ivanova, S. A. Food security: The challenge of the present. *Geoforum* **91,** 73–77 (2018).

22. Beeckman, F., Motte, H. & Beeckman, T. Nitrification in agricultural soils: impact, actors and mitigation. *Curr. Opin. Biotechnol.* **50,** 166–173 (2018).

23. Timilsena, Y. P., Adhikari, R., Casey, P., Muster, T., Gill, H. & Adhikari, B. Enhanced efficiency fertilisers: A review of formulation and nutrient release patterns. *J. Sci. Food Agric.* **95,** 1131–1142 (2015).

24. Byrne, M. P., Tobin, J. T., Forrestal, P. J., Danaher, M., Nkwonta, C. G., Richards, K., Cummins, E., Hogan, S. A. & O'Callaghan, T. F. Urease and nitrification inhibitors-As mitigation tools for greenhouse gas emissions in sustainable dairy systems: A review. *Sustain.* **12,** 1–35 (2020).

25. Rekharsky, M. V. & Inoue, Y. Complexation thermodynamics of cyclodextrins. *Chem. Rev.* **98,** 1875–1917 (1998).

26. Connors, K. A. The stability of cyclodextrin complexes in solution. *Chem. Rev.* **97,** 1325–1357 (1997).
27. Uekama, K., Hirayama, F. & Irie, T. Cyclodextrin drug carrier systems. *Chem. Rev.* **98,** 2045–2076 (1998).
28. Smith, V. J., Rougier, N. M., de Rossi, R. H., Caira, M. R., Buján, E. I., Fernández, M. A. & Bourne, S. A. Investigation of the inclusion of the herbicide metobromuron in native cyclodextrins by powder X-ray diffraction and isothermal titration calorimetry. *Carbohydr. Res.* **344,** 2388–2393 (2009).
29. Macrae, C. F., Edgington, P. R., McCabe, P., Pidcock, E., Shields, G. P., Taylor, R., Towler, M. & van de Streek, J. Mercury: visualization and analysis of crystal structures. *J. Appl. Crystallogr.* **39,** 453–457 (2006).
30. Groom, C. R., Bruno, I. J., Lightfoot, M. P. & Ward, S. C. The Cambridge Structural Database. *Acta Crystallogr. Sect. B* **72,** 171–179 (2016).
31. Coelho, A. A. TOPAS-Academic V4.1. (2007).
32. Caira, M. R. On the isostructurality of cyclodextrin inclusion complexes and its practical utility. *Rev. Roum. Chim.* **46,** 371–386. (2001).

CHAPTER 4

SUNSCREENS

4.1 Sunscreens: state of the art

With an annual incidence constantly growing, skin cancer is considered one of the fastest rising forms of cancer.[1] One of the main risk factor for skin cancer development is ultraviolet (UV) radiation, whose action is also responsible for sunburn and photoaging.[2] The increasing awareness regarding photoprotection has led to a widespread use of sunscreens lotions, meant to prevent skin damage with a concomitant gradual tanning.[3]

Depending on the kind of interaction with UV radiation, the active ingredients of sunscreens are divided into inorganic (physical) and organic (chemical) filters.[4] Inorganic filters - mainly titanium dioxide[5] and zinc oxide - protect from solar radiation by reflecting and refracting UV photons while organic filters are designed to absorb UVA and UVB photons.

Although the main feature of sunscreens should be the photostability, a formulation 100% photostable is still a utopia.[6,7] Indeed, singlet oxygen, reactive oxygen species and other harmful reactive intermediates are generally formed under the UV irradiation, with dreadful consequences for health[8] and environment.[20]

The environmental impact of sunscreens - especially regarding the sea environment - has been highlighted quite recently.[21,15] UV filters were found to be the main responsible of severe damages to the coral reefs in terms of bleaching, depression of coral reproductive system and deformation of coral larvae.[9] Given the huge amount of sun creams annually released in the seawater,[12,21] some countries such as Palau[13] and Hawaii[14] have banned a series of UV filters starting from 2020.[15–17]

The quest for new sun creams formulations is oriented towards a photostabilization of the main UV filters, including avobenzone (UVA filter) and octinoxate (UVB filter). When these two compounds are combined together, they interact with each other, giving rise to a photoproduct which is no longer photoactive.[18–25] Moreover, they can easily photodegrade along with the exposition under the UV radiation:[30,32] avobenzone converts into the diketo form - which absorbs in the UVC range -[7] and degrades in radical fragments, while octinoxate undergoes photoisomerization from E-octinoxate to Z-octinoxate, which is the less active form.[20]

In this research project, the photostabilization of avobenzone and octinoxate has been pursued through their encapsulation into β-CD molecules. Although such approach is already known,[42] the novelty of the topic lies in the utilization of the mechanochemical method as synthetic route and in a fully characterization of the obtained complexes through the solid-state methods.

4.2 β-CD inclusion complexes

β-CD is a cyclic oligosaccharide formed by seven D-glucose units linked by α-1,4 glycosidic bonds with a truncated cone shape (Fig.1). The main feature of β-CD - as of all the cyclodextrins - is to possess a hydrophilic surface and a hydrophobic cavity, thus resulting in a water-soluble compound able to include apolar organic molecules.[30] The main driving force for the inclusion of guest molecules into β-CD cavity is the hydrophobic effect, but also van der Waals interactions and hydrogen bonds may contribute to the formation of host-guest inclusion complexes.

β-CD inclusion complexes represent a powerful tool to improve the chemical-physical properties of the guest molecules in terms of water solubility, chemical stability, bioavailability and dissolution rate,[31] while preserving the characteristics of biocompatibility and bioavailability. As a result of these features, β-CD has been extensively employed in the pharmaceutical field - as a drug carrier - as well as in the food industry and in the environmental sciences.[32,33]

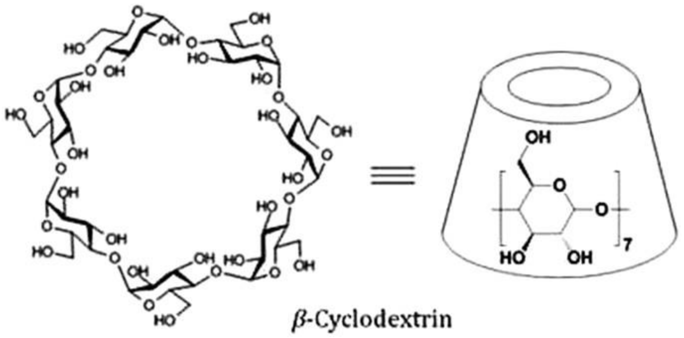

Fig.1: schematic representation of β-CD (ref.30).

Given the wide use of β-CD inclusion complexes, they have been extensively studied from the solid-state point of view, resulting in more than 300 structures deposited in the CSD database. The main technique for crystal structural resolution is single crystal X-ray diffraction, through which it is possible to (1) unequivocally prove the inclusion of the guest molecule into the β-CD cavity, (2) gain a better understanding of the interactions involved as well as of the role of the water molecules in such interactions and (3) obtain a calculated XRPD pattern to use as reference pattern.[34,35]

When it is not possible to grow single crystals suitable for crystal structure resolution, structural information can be obtained from powder diffraction data.[36,37] As already pointed out in Caira's works,[38,39] β-CD molecules crystallize in eight possible isostructural series, each with β-

CD molecules essentially in the same crystal arrangement and the corresponding unit cell parameters almost coincident. Therefore, the XRD patterns are extremely similar - then superimposable - regardless of the chemical nature of the guest molecules.

In this research project, structural information on the mechanochemically synthesized β-CD inclusion complexes were obtained from powder diffraction data: interestingly, both complexes were found to be isostructural and fall in the C2 isostructural series.[40]

With the help of spectroscopic, spectrometric and thermal techniques,[41,42] a fully solid-state characterization was performed and the filters were proven to be effectively improved in terms of photostability.

4.3 Methods and techniques

My contribution to the work was mainly through the use/interpretion of the following techniques and methods:

- Synthesis of the inclusion complexes through the mechanochemical method, via slurry and from solution (water/EtOH).
- X-ray Powder Diffraction (XRPD) to assess the formation of the complexes and deduce the related space groups according to the principle of isostructurality.
- Differential Scanning Calorimetry (DSC) for the detection of eventual phase changes (dehydration/desolvation, polymorphic transition, melting).
- Thermogravimetric Analysis (TGA) to calculate the degree of hydration and evaluate the thermal stability.
- ^{1}H NMR to confirm the stoichiometry of the complexes.

ACS Sustainable Chemistry & Engineering

pubs.acs.org/journal/ascecg

Research Article

Environmentally Friendly Sunscreens: Mechanochemical Synthesis and Characterization of β-CD Inclusion Complexes of Avobenzone and Octinoxate with Improved Photostability

Simone d'Agostino, Alessandra Azzali, Lucia Casali, Paola Taddei,* and Fabrizia Grepioni*

Cite This: *ACS Sustainable Chem. Eng.* 2020, 8, 13215–13225

Read Online

ACCESS | Metrics & More | Article Recommendations | Supporting Information

ABSTRACT: We report on the mechanochemical synthesis of inclusion complexes obtained by reacting β-cyclodextrin (β-CD) with two widely used sunscreens, namely, avobenzone (AVO) and octinoxate (OCT). Formation of crystalline inclusion complexes was confirmed via a combination of solid-state techniques, including X-ray diffraction (XRD), Raman, and ATR-FTIR spectroscopies. A new, metastable polymorph of avobenzone was also isolated and characterized. NMR spectroscopy and thermal analyses (TGA and DSC) allowed us to evaluate the host/guest ratio and the water content (ca. $8H_2O$) in crystalline $(\beta\text{-CD})_2\cdot$AVO and $(\beta\text{-CD})_3\cdot$OCT$_2$. Photodegradation of the two sunscreens upon inclusion in the hydrophobic cavity of β-CD was evaluated in solution via mass spectrometry (ESI-MS) and UV–vis spectroscopy and found to be sharply reduced. All findings indicate that the inclusion of AVO and OCT in β-CD might represent a viable route for the preparation of environmentally friendly sunscreens with improved photostability to be used in formulations of sun creams.

KEYWORDS: *Avobenzone, Octynoxate, Sunscreens, Cyclodextrins, Inclusion complexes, Mechanochemistry*

For copyright reasons only the link to the original article is reported here:

https://doi.org/10.1021/acssuschemeng.0c02735

4.4 Supporting Information

XRPD patterns of the reactants β-CD and avobenzone

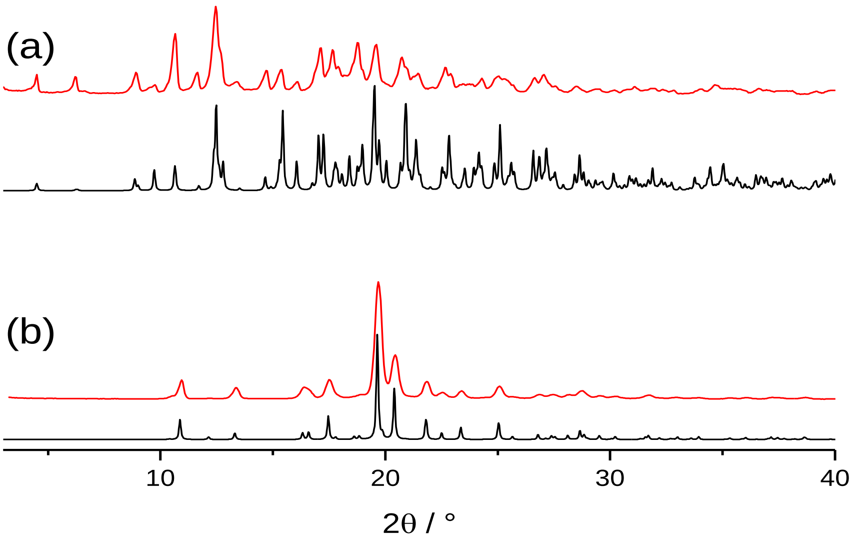

Figure SI-1. Experimental (red line) and calculated (black line) X-ray powder diffraction patterns of: (a) hydrated β-cyclodextrin (CSD refcode: BCDEXD04), and (b) avobenzone Form I (CSD refcode: WEBGAL). Polycrystalline Avobenzone Form I was obtained after recrystallization in acetonitrile.

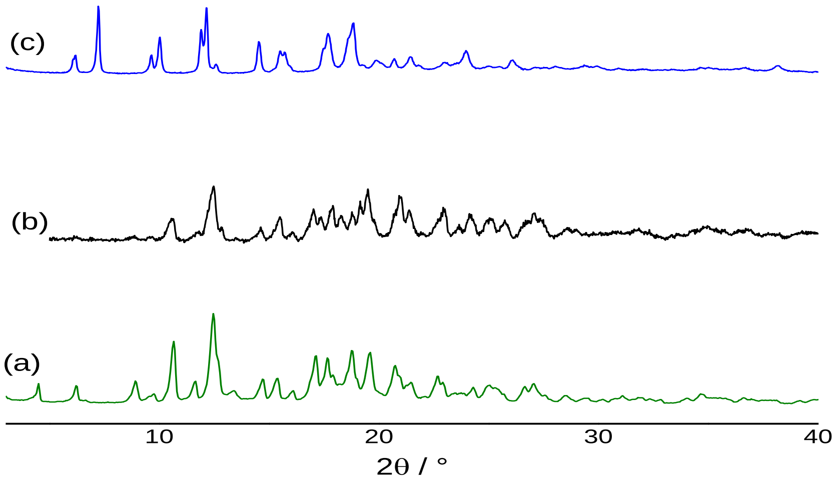

Figure SI-2. Comparison of the XRPD patterns for the mechanochemical synthesis of $(\beta\text{-CD})_3\cdot OCT_2$ from the parent materials: (a) β-CD, (b) the product obtained from grinding, and by (c) kneading with few drops of water.

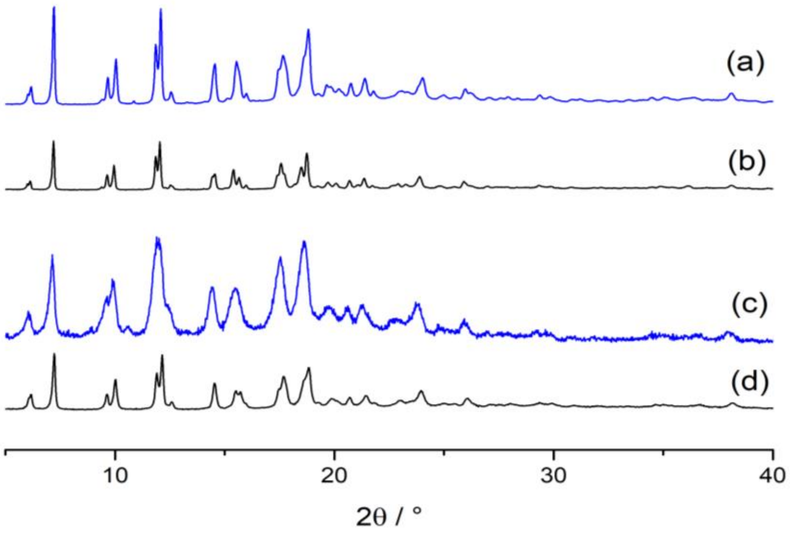

Figure SI-3. Comparison between experimental XRPD patterns for the inclusion complexes obtained from different synthetic methods: (β-CD)$_2$·AVO from kneading (a) and slurry (b), and (β-CD)$_3$·OCT$_2$ from kneading (c) and slurry (d).

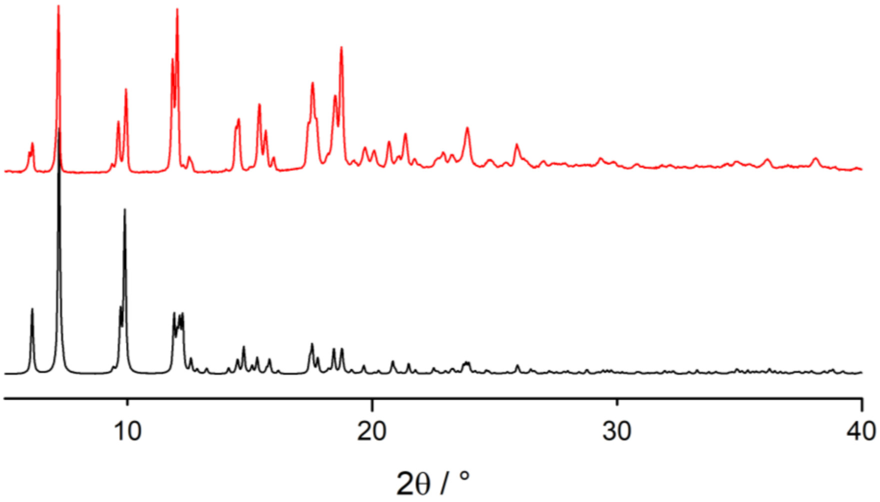

Figure SI-4. Comparison between the X-ray powder diffraction patterns of (β-CD)$_2$·AVO: (a) experimental, recorded at RT (red line), and calculated from the single crystal data as determined at 100K (black line).

Avobenzone Form II

The crystal structure of avobenzone was first published in 1993 by Kagawa et al,[43] and corresponds to the major component of commercial avobenzone. A different form was detected upon phase purity check of commercial avobenzone.

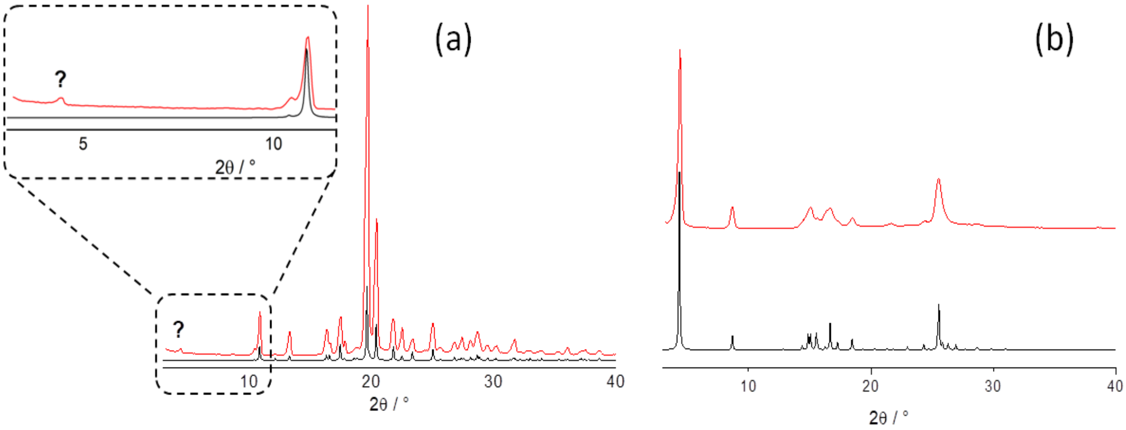

Figure SI-5. (a) The peak at low angle detected upon phase purity check of a commercial sample of avovenzone; experimental (red line) and calculated (CSD refcode: WEBGAL, black line) XRPD patterns. (b) Experimental (red line) and calculated (black line) XRPD patterns for avobenzone Form II.

Thermal analyses (TGA and DSC) allowed us to better understand the behaviour of the avobenzone polymorphic system. The TGA thermogram (Figure SI-9) of commercial powders of avobenzone, corresponding to Form I, shows a degradation process starting at ca. 150°C, while the DSC trace shows a peak at ca 87 °C (74 J/g), ascribable to the melting of avobenzone, as previously reported. The melted material was then cooled to RT and tapped with a needle. A crystallization process took place, and a new DSC (Figure SI-10) was recorded. A new endothermic peak at ca 76°C (36 J/g) was detected.

Variable Temperature PXRD and Hot Stage Microscopy (Figure SI-6) were successfully applied to confirm what previously observed. Avobenzone Form I was melted at 90°C and cooled to RT to afford a high viscous amorphous material, that after tapping crystallized as polycrystalline Form II. This powder was used as seeds to grow single crystals from methanol.

In conclusion, the form obtained from melt is a new, metastable polymorph. As the new Form II is only accessible from melt, and no endothermic transition is observed in the solid state, the two forms constitute a monotropic system.

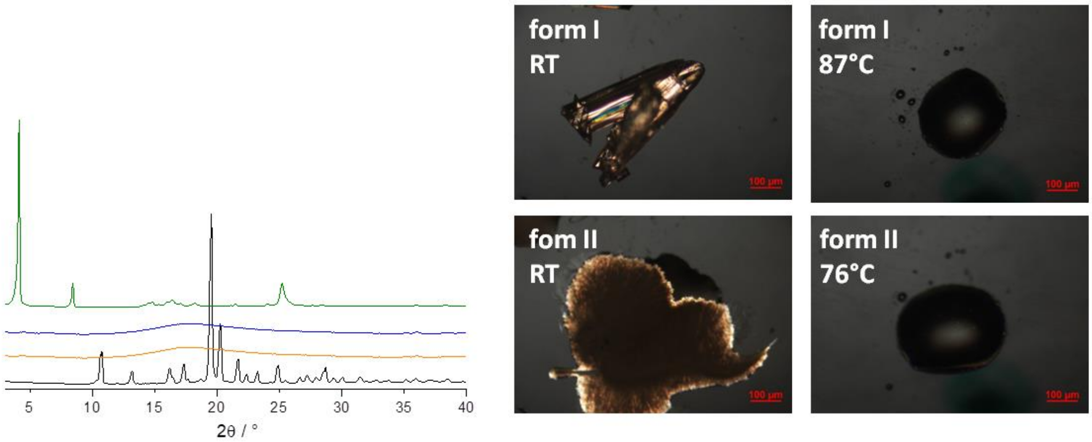

(a) (b)

Figure SI-6. (a) VT-PXRD: avobenzone Form I (black line), melted avobenzone at 90°C (orange line), amorphous phase at RT (blue line), and avobenzone Form II (green line). (b) The same process followed by hot-stage microscopy.

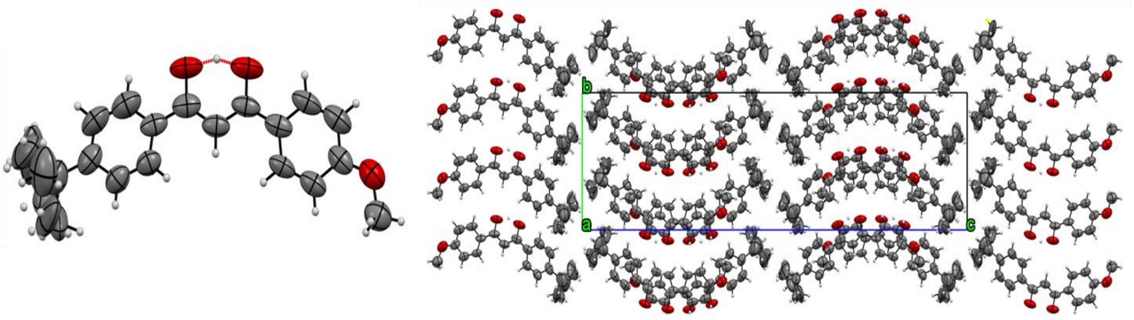

(a) (b)

Figure SI-7. (a) Ortep Plot (thermal ellipsoids drawn at 50% probability) showing the intramolecular hydrogen bond [$O_{OH}\cdots O_{CO} = 2.465(6)$ Å] for avobenzone Form II, and (b) crystal packing viewed along the *a*-axis.

Crystal data and refinement details for crystalline avobenzone Form II and (β-CD)$_2$·AVO

Table SI-1. Crystal data and refinement details for crystalline avobenzone Form II and (β-CD)$_2$·AVO.

	Avobenzone Form II	**(β-CD)$_2$·AVO**
Formula	$C_{20}H_{22}O_3$	$C_{104}H_{178}O_{81}$
fw	310.38	2724,49
Temperature (K)	300	100
Cryst. System	Orthorhombic	Monoclinic
Space group	Pbca	C2
Z'	1	0.5
Z	8	4
a (Å)	7.3175(10)	18.9533(14)
b (Å)	11.8808(10)	24.4863(17)
c (Å)	40.778(7)	15.4504(12)
α (deg)	90	90
β (deg)	90	109.543(4)
γ (deg)	90	90
V (Å^3)	3545.1(8)	6757.4(9)
D_{calc} (g/cm^3)	1.163	1.339
μ (mm^{-1})	0.077	1.009
Measd reflns	12729	51430
Indep reflns	3124	12359
Largest diff. peak/hole (e/Å^3)	0.10/-0.09	0.46/-0.48
R_1[on F_0^2, I>2σ(I)]	0.0761	0.0650
wR_2 (all data)	0.1399	0.1925

Pawley Refinement Plots of the inclusion complexes (β-CD)$_2$·AVO and (β-CD)$_3$· OCT$_2$

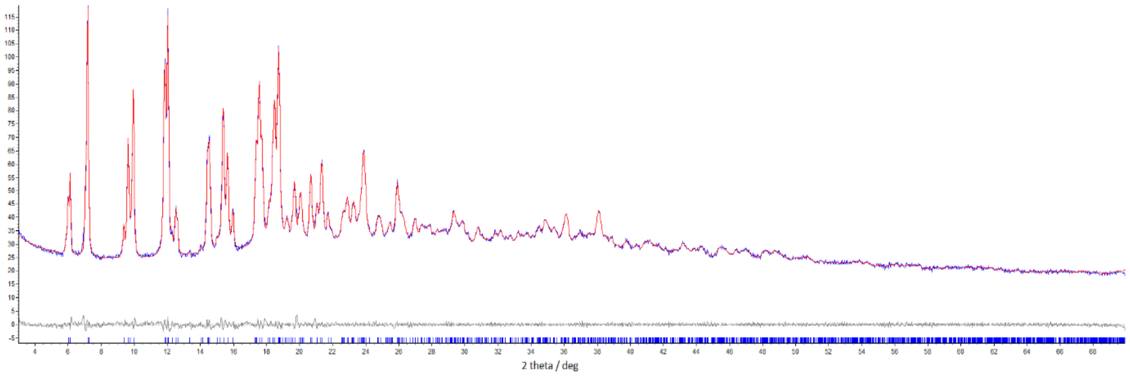

	SG	*a/Å*	*b/Å*	*c/Å*	*α/°*	*β/°*	*γ/°*	*Volume/Å³*	*Rwp; GoF*
(β-CD)$_2$·AVO	C2	18.976(2)	24.533(2)	15.701(2)	90	110.675(8)	90	6839.6(1)	3.4%; 1.8

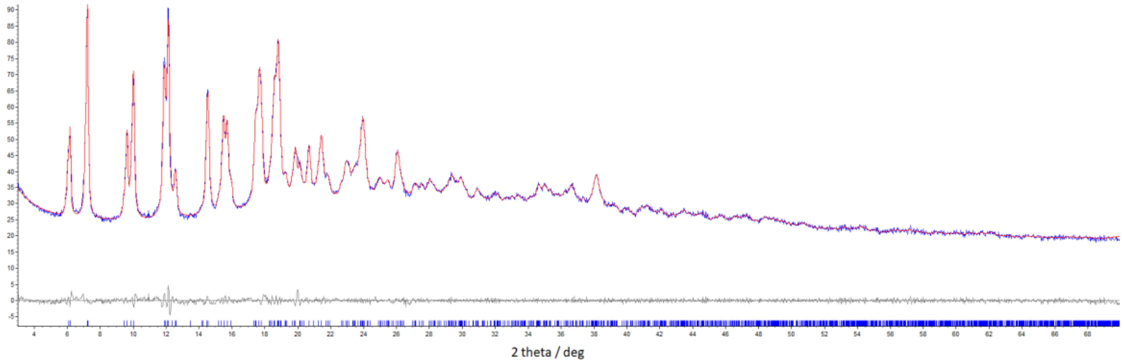

	SG	*a/Å*	*b/Å*	*c/Å*	*α/°*	*β/°*	*γ/°*	*Volume/Å³*	*R_{wp}; GOF*
(β-CD)$_3$·OCT$_2$	C2	18.941(4)	24.433(7)	15.646(3)	90	111.39(1)	90	6742.2(9)	3.5%; 1.7

Figure SI-8. Pawley refinements plots with the corresponding unit cell parameters and FOMs for the inclusion complexes (β-CD)$_2$·AVO (top) and (β-CD)$_3$·OCT$_2$ (bottom) obtained via slurry

^{1}H-NMR of the β-cyclodextrin (β-CD), avobenzone (AVO), and octinoxate (OCT)

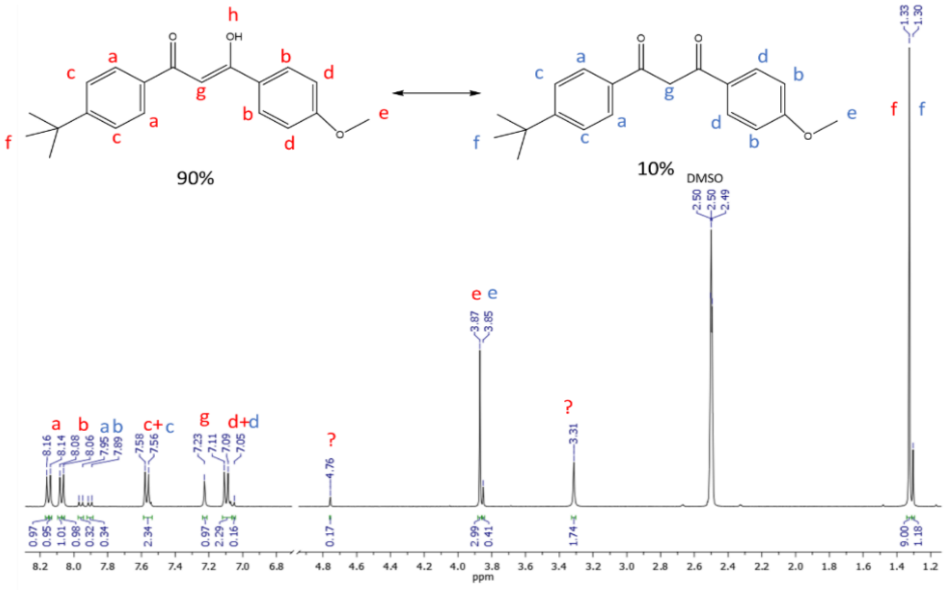

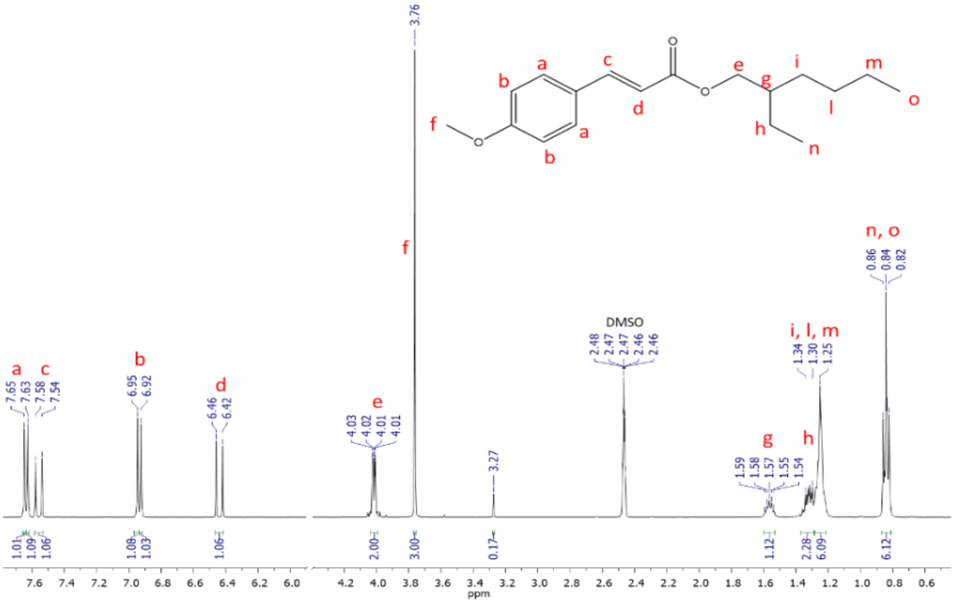

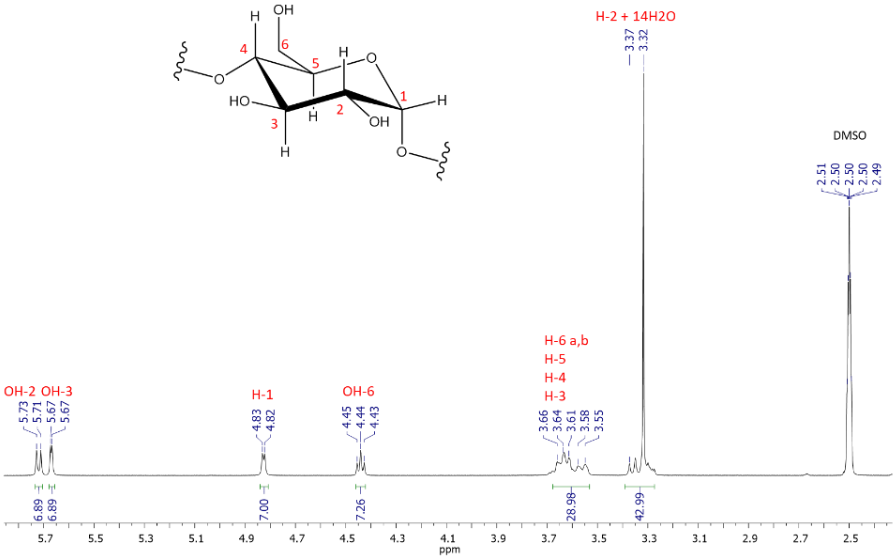

Figure SI-9. ^{1}H-NMR spectra in DMSO-d6 of the starting materials: avobenzone (top), octinoxate (middle), and β-cyclodextrin (bottom). Note: the signal assignment for the β-cyclodextrin was based on the reported one[44].

^{1}H-NMR of the inclusion complexes $(\beta\text{-CD})_2\cdot\text{AVO}$ and $(\beta\text{-CD})_3\cdot\text{OCT}_2$

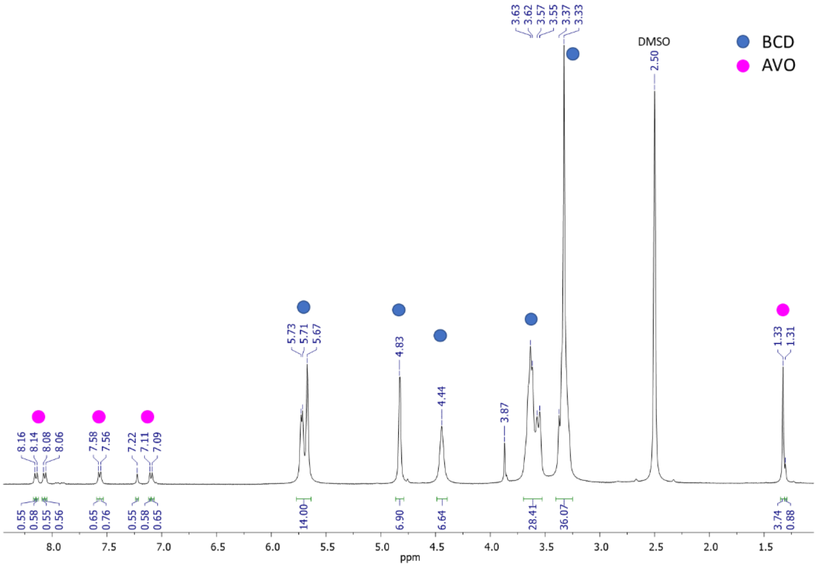

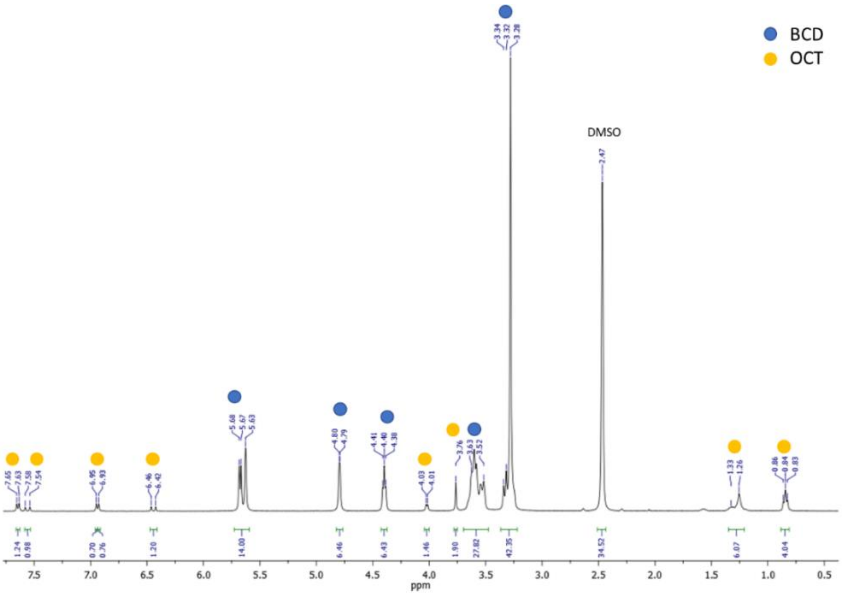

Figure SI-10. ^{1}H-NMR spectra in DMSD-d^6 of the inclusion complexes $(\beta\text{-CD})_2\cdot$AVO (top) and $(\beta\text{-CD})_3\cdot$OCT$_2$ (bottom) obtained via slurry. These ^{1}H-NMR analyses allowed to calculate the host/guest stoichiometric ratio by comparing the integration of the peaks corresponding to the two components. It must be noticed that this calculation can be done in samples containing the inclusion complex alone and the purity of these samples was verified by PXRD analysis. It results in a stoichiometry $(\beta\text{-CD})_2\cdot$AVO for avobenzone (see Figure SI-10 above, peak at 8.16 ppm corresponding to one hydrogen and integrating for 0,55 H-atoms) and $(\beta\text{-CD})_3\cdot$ OCT$_2$ for (see Figure SI-10 under, peak at 7.65 ppm corresponding to two hydrogens and integrating for 1.24 H-atoms).

TGA traces

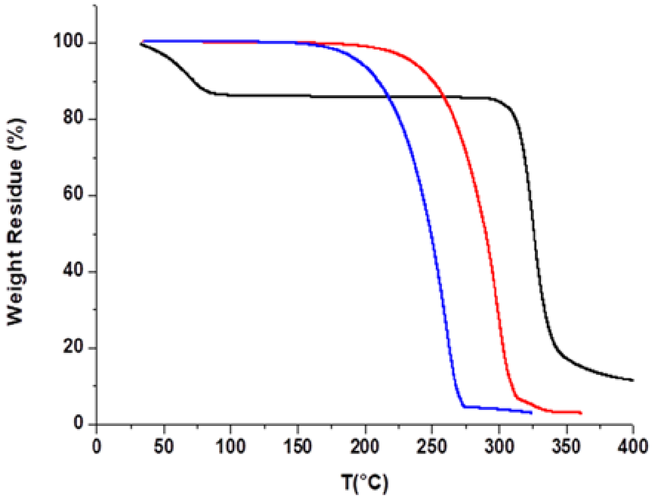

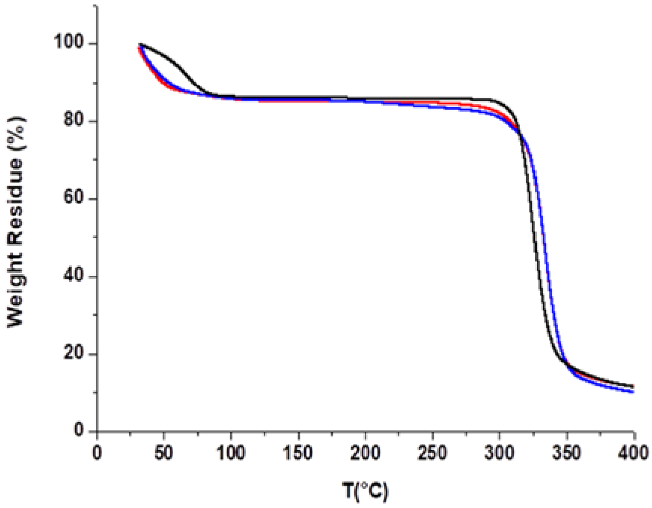

Figure SI-11. Top, TGA thermograms for β-CD (black line), avobenzone form I (red line), and octinoxate (blue line). Bottom, TGA thermograms for inclusion complexes $(\beta\text{-CD})_2{\cdot}\text{AVO}$ (red line) and $(\beta\text{-CD})_3{\cdot}\ \text{OCT}_2$ (blue line) superimposed to the one of the β-CD (black line).

DSC traces

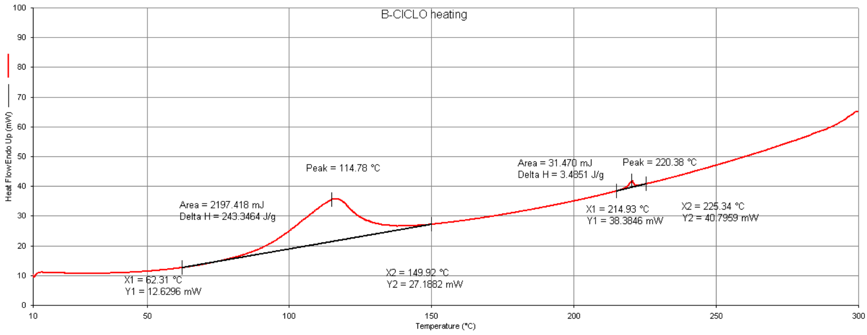

(a)

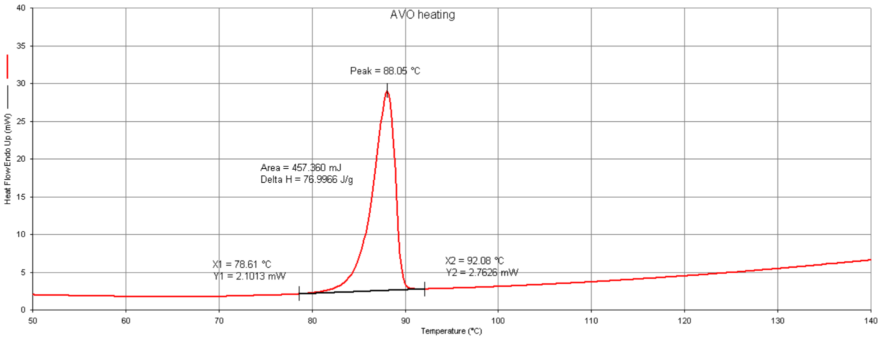

(b)

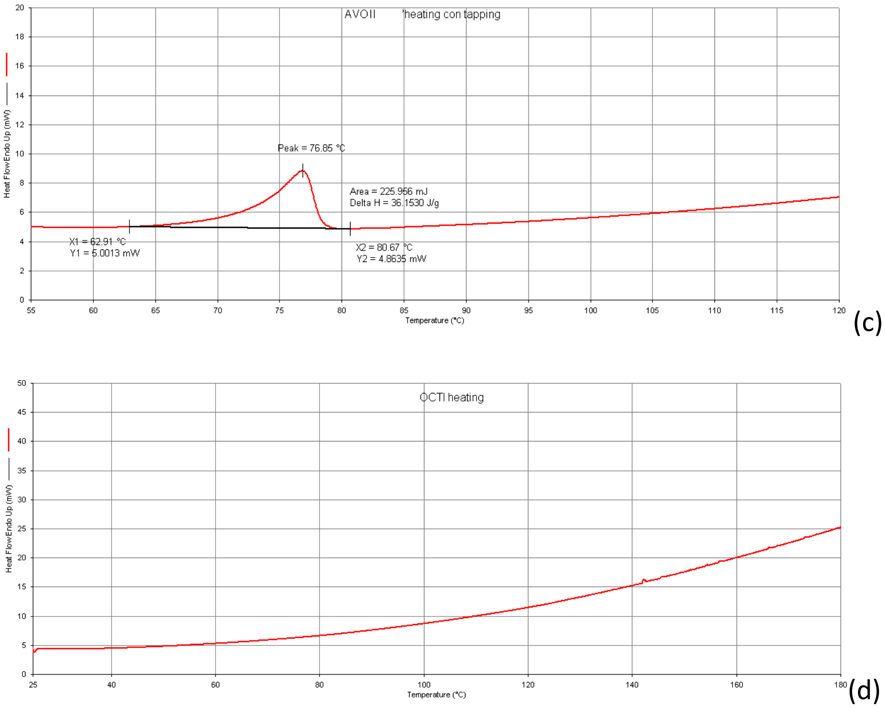

Figure SI-12. DSC traces for β-CD (a), avobenzone Form I (b), avobenzone Form II (c), and octinoxate (d).

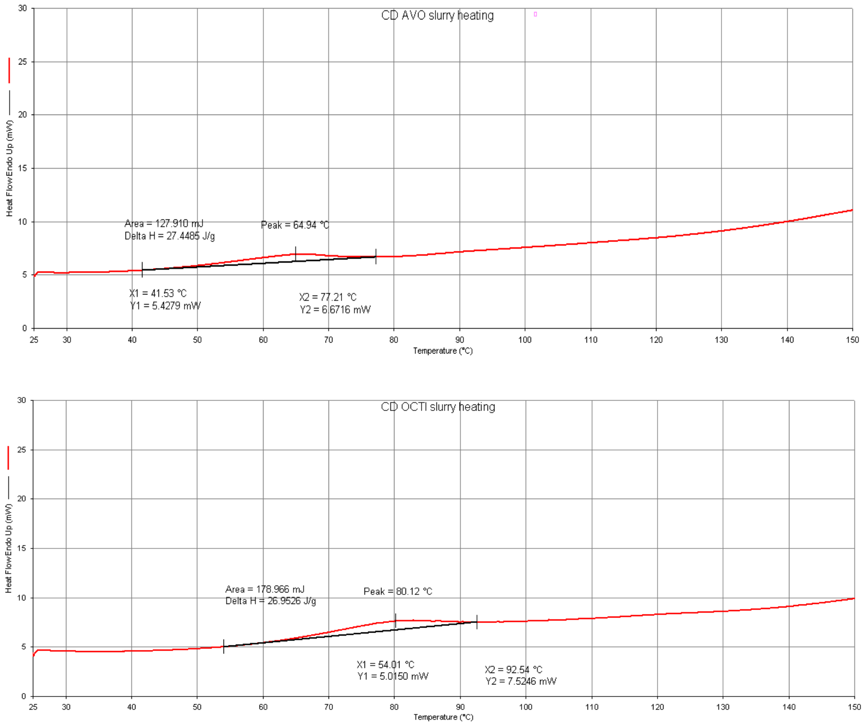

Figure SI-13. DSC traces for the inclusion complexes $(\beta\text{-CD})_2\cdot$AVO (top) and $(\beta\text{-CD})_3\cdot\text{OCT}_2$ (bottom).

Raman and FTIR spectra

Table SI-2. Raman wavenumbers and assignments[45,46] for the main bands of the $(\beta\text{-CD})_3\cdot\text{OCT}_2$ inclusion complex, octinoxate and β-CD. [For sake of clarity, octinoxate and β-CD are indicated here as O and B, respectively.]

$(\beta\text{-CD})_3\cdot\text{OCT}_2$	octinoxate	β-CD	Assignments[45,46]
~ 3290		~ 3290	OH stretching (B)
3073	3073		CH stretching (O)
2940		2937	CH stretching (B)
2903		2903	CH stretching (B)
1709	1708		C=O stretching (O)
1632	1636		exocyclic C=C stretching (O)
1604	1606		ring stretching (O)
1575	1577		ring stretching (O)
1384		1386	CH bending (B)
1327		1334	OH in plane bending (B)
1263	1267		ester and methoxy C-O stretching (O)
1253	1251		ester and methoxy C-O stretching (O)
1205	1205		methoxy C-O-C bending (O)
1170	1172		CH bending (O)
1055-1034		1049	coupled CC and CO stretching (B)
597-579		587-579	ring vibration (B)
535			ring vibration (B)
481		481	ring vibration (B)

449		441	ring vibration (B)
359		351	ring vibration (B)

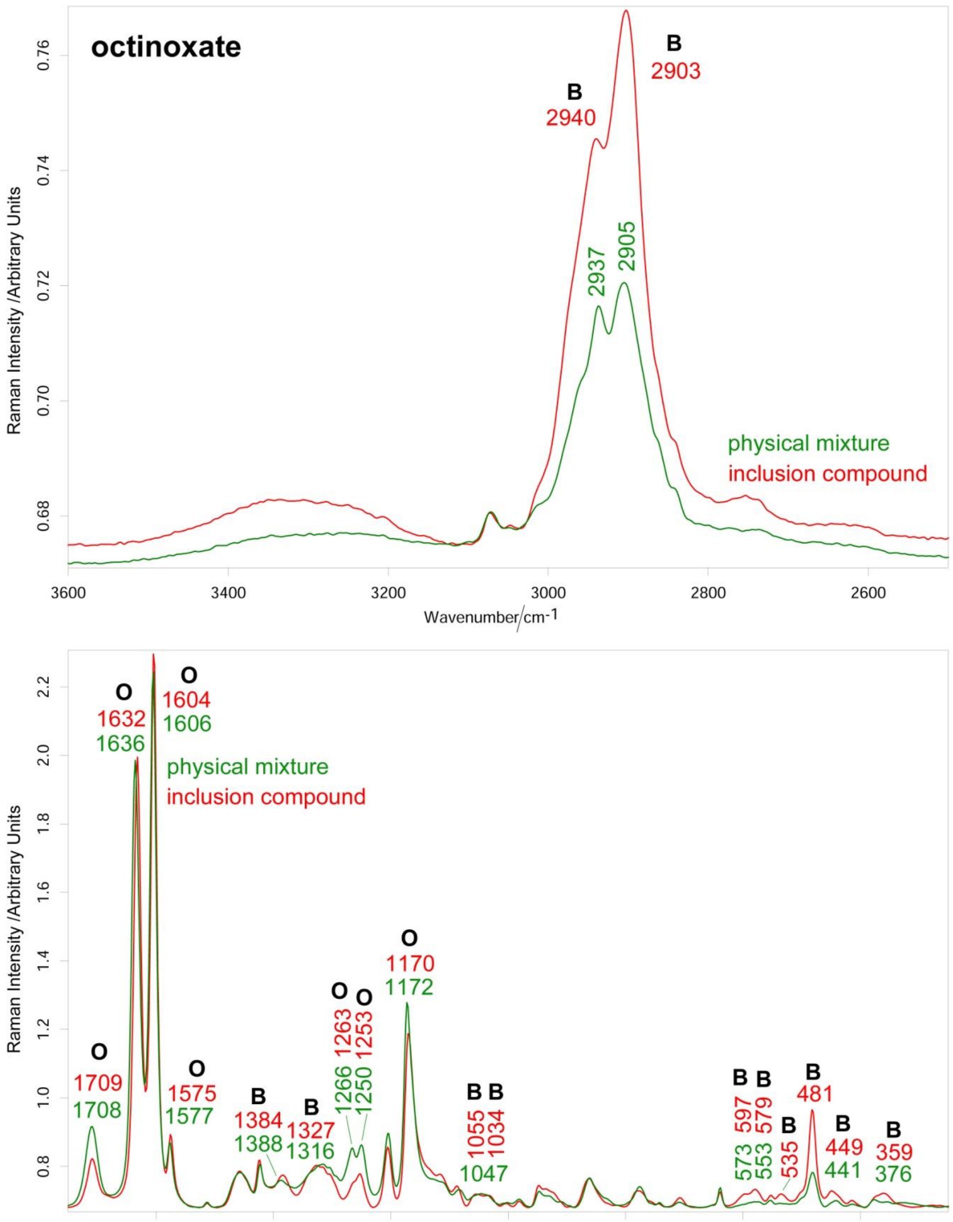

Figure SI-14. Raman spectra of the (β-CD)$_3$·OCT$_2$ inclusion compound and 3:2 physical mixture. The main bands showing differences in the two spectra are indicated and assigned prevalently to octinoxate (O) or β-CD (B).

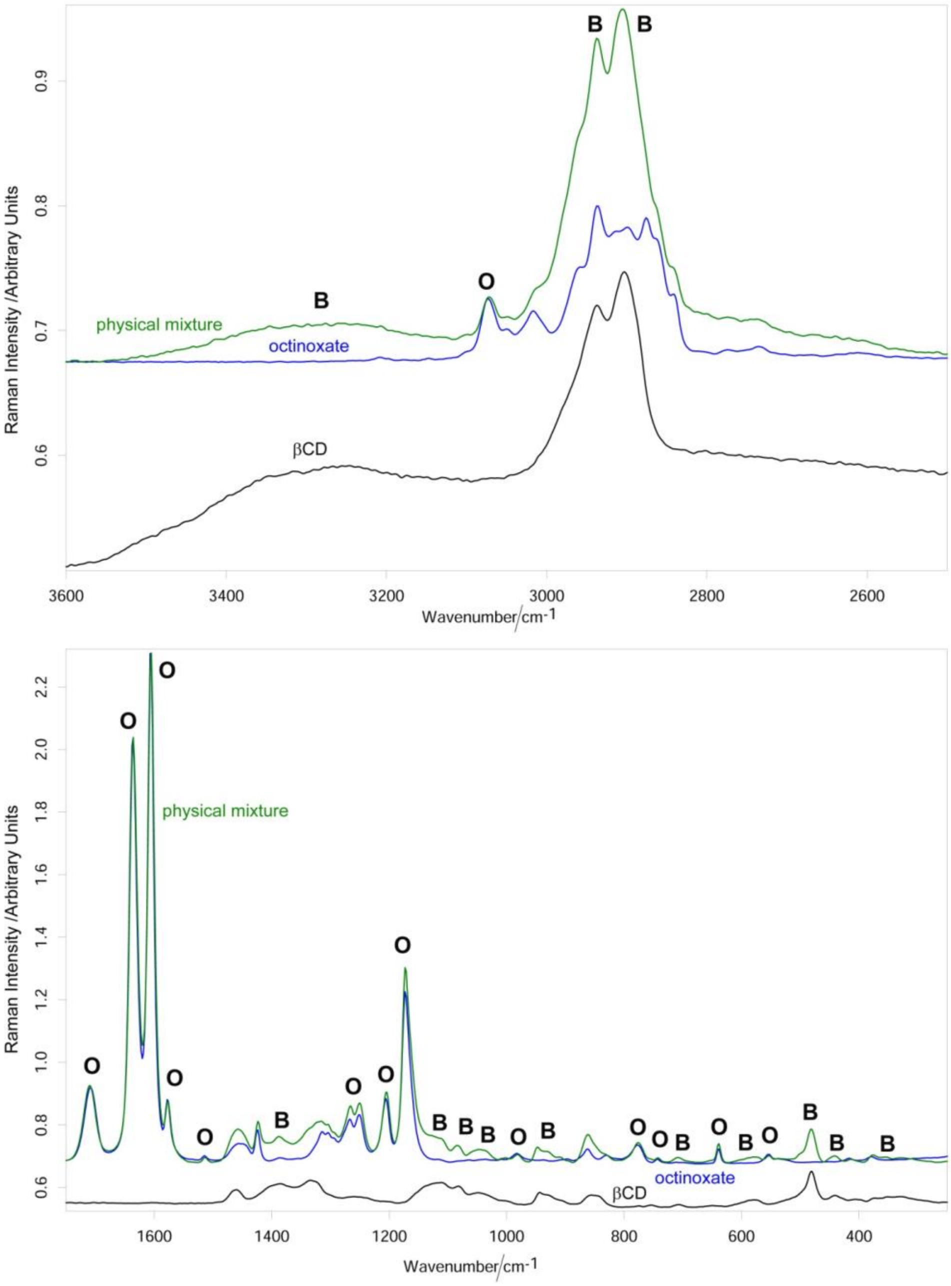

Figure SI-15. Raman spectrum of the 3:2 β-CD/octinoxate physical mixture. The spectra of octinoxate and β-CD are reported for comparison. The bands in the spectrum of the physical mixture prevalently assignable to octinoxate or β-CD are indicated with O and B, respectively. The bands not indicated have comparable contributions from both components.

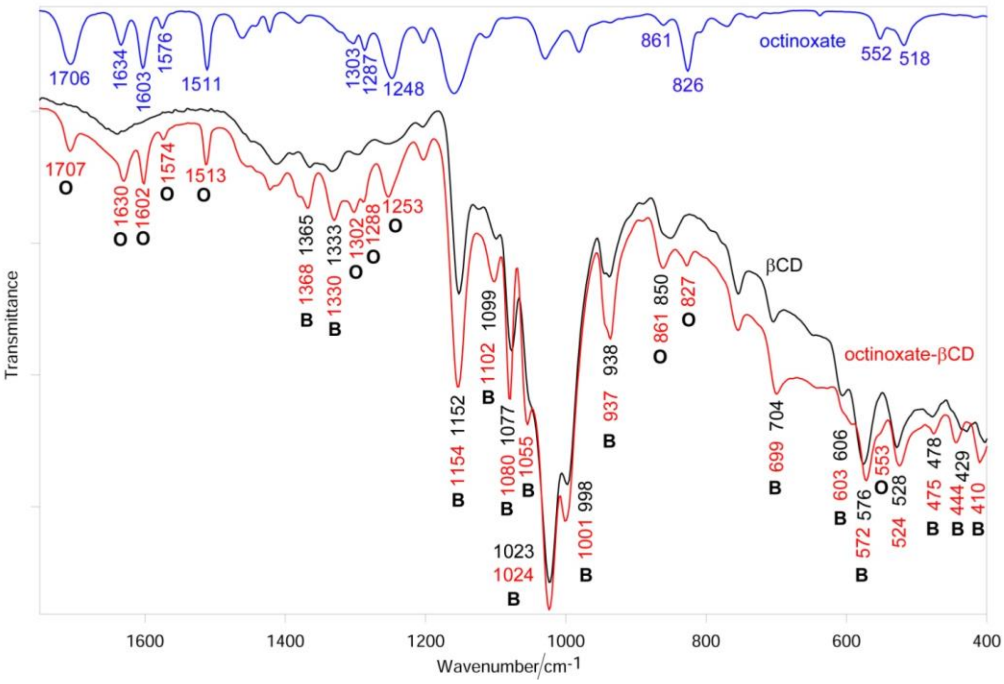

Figure SI-16. IR spectra of (β-CD)$_3$·OCT$_2$, octinoxate and β-CD. The main bands of octinoxate and β-CD that underwent changes upon formation of the inclusion compound are indicated with O and B, respectively.

Table SI-3. Raman wavenumbers and assignments[45–51] of the main bands of (β-CD)$_2$·AVO, avobenzone and β-CD. [For sake of clarity, avobenzone and β-CD are indicated here as A and B, respectively.]

(β-CD)$_2$·A	avobenzone form I	β-CD	Assignments[45–51]
~ 3290		~ 3290	OH stretching (B)
3074	3073		CH stretching (A)
2937		2937	CH stretching (B)
2906		2903	CH stretching (B)
1683			β-diketone C=O stretching (A)
1608	1607		C=O stretching, ring stretching coupled to C-C–C=O asymmetric stretching (A)

	1557		ring stretching coupled to C-C–C=O and OH bending (A)
1513	1518		ring stretching coupled to C-C–C=O and OH bending (A)
1383		1386	CH bending (B)
1309	1298		C-O stretching (A)
1263	1260		methoxy C-O stretching (A)
1230	1231		methoxy C-O stretching (A)
1197	1200		methoxy C-O-C bending (A)
1175	1170		CH bending (A)
1111	1114		CH bending + CO stretching (A)
1088		1082	coupled CC and CO stretching (B)
1055-1031		1049	coupled CC and CO stretching (B)
948		944	ring vibration (B)
865		856	C1 group vibration (B)
772-756	774-756		CH out-of-plane bending + ring deformation (A)
700	698		ring deformation + CH out-of-plane bending (A)
599-580		587-579	ring vibration (B)
535			ring vibration (B)
481		481	ring vibration (B)
449		441	ring vibration (B)
415		406	ring vibration (B)

357		351	ring vibration (B)

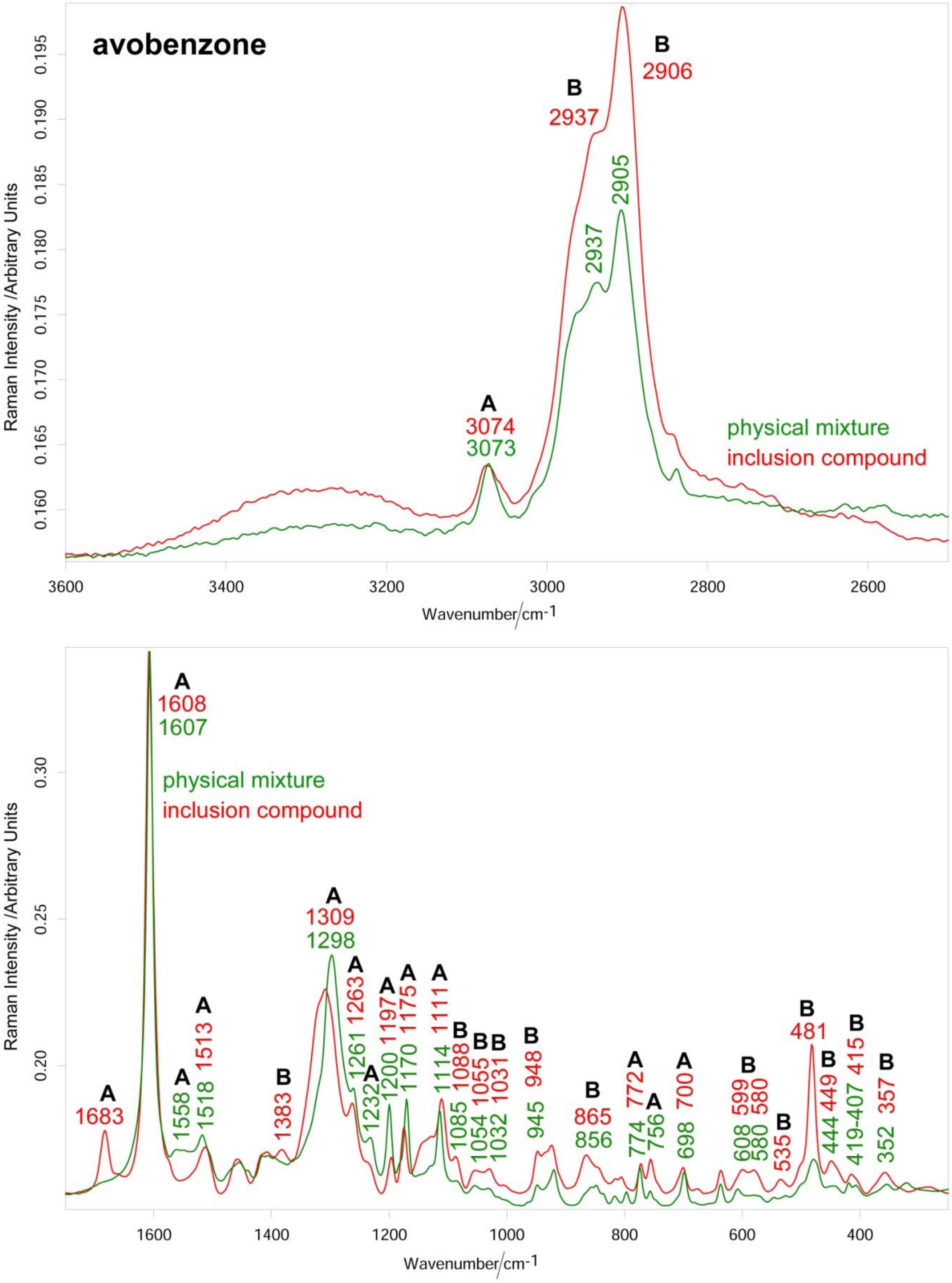

Figure SI-17. Raman spectra of (β-CD)$_2$·A and 2:1 physical mixture. The main bands showing differences in the two spectra are indicated, and assigned prevalently to avobenzone (A) or β-CD (B).

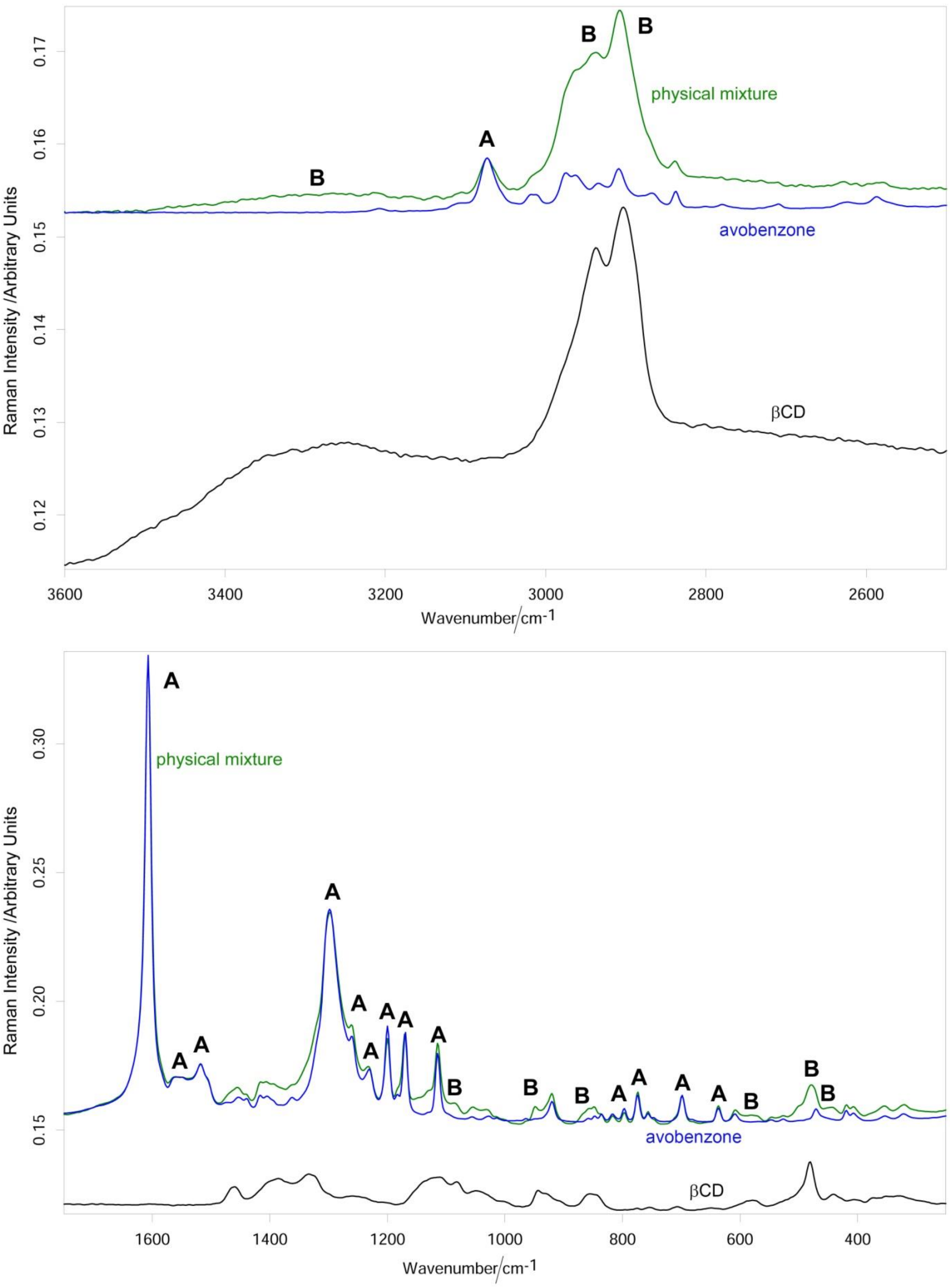

Figure SI-18. Raman spectrum of the 2:1 β-CD/avobenzone physical mixture. The spectra of avobenzone and β-CD are reported for comparison. The bands in the spectrum of the physical mixture prevalently assignable to avobenzone or β-CD are indicated with A and B, respectively. The bands not indicated have comparable contributions from both components.

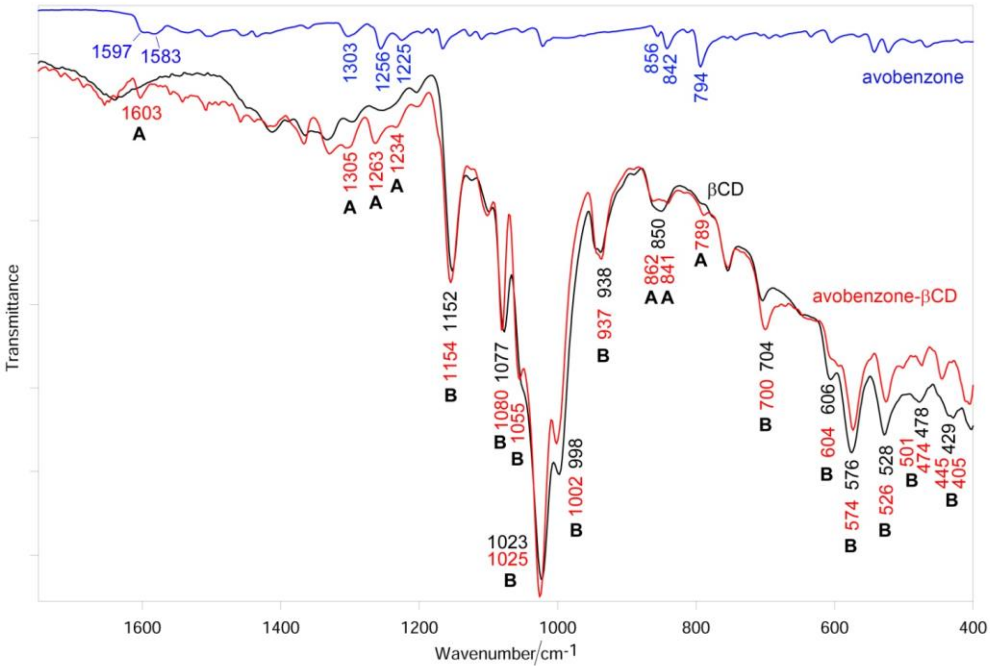

Figure SI-19. IR spectra of the (β-CD)₂·A, avobenzone and β-CD. The main bands of avobenzone and β-CD that underwent changes upon formation of the inclusion compound are indicated with A and B, respectively.

ESI-MS spectra

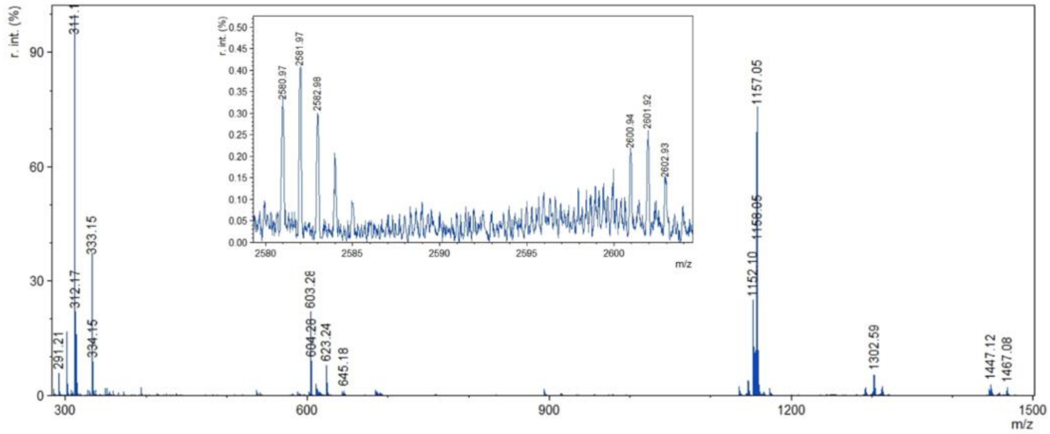

Figure SI-20. ESI-MS spectrum of the non-irradiated physical mixture containing the inclusion complexes (β-CD)₂·AVO and (β-CD)₃·OCT₂.

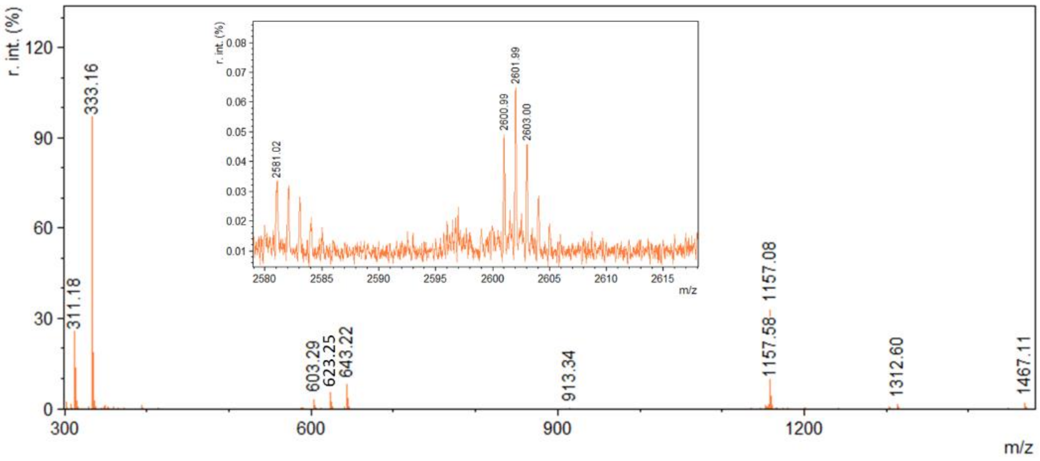

Figure SI-21. ESI-MS spectrum of the irradiated physical mixture containing the inclusion complexes (β-CD)$_2$·AVO and (β-CD)$_3$·OCT$_2$.

Table SI-4. List of the m/z peaks found in the ESI-MS spectrum solution of the non-irradiated inclusion complexes (β-CD)$_2$·AVO and (β-CD)$_3$·OCT$_2$.

m/z	int.	
291,2073	453,9766	[OCT+H]$^+$
311,1702	7698,495	[AVO+H]$^+$
313,182	1304,758	[OCT+Na]$^+$
333,1457	2933,152	[AVO+Na]$^+$
603,2771	1760,921	[2OCT+Na]$^+$
623,2391	620,4783	[AVO+OCT+Na]$^+$
643,2004	75,95998	[2AVO+Na]$^+$
1152,098	2018,459	[β-CD+NH$_4$]$^+$
1157,051	6170,942	[β-CD+Na]$^+$
1291,599	157,1981	[OCT+2β-CD+H$^+$+Na]$^+$
1302,587	432,5796	[OCT+2 β-CD+2Na]$^+$
1312,567	192,6248	[AVO+2 β-CD+2Na]$^+$

1445,107	134,5882	[AVO+β-CD+H]$^+$
1447,115	221,2681	[OCT+β-CD+Na]$^+$
1467,078	171,3711	[AVO+β-CD+Na]$^+$
1724,491	716,0297	[3β-CD+2Na]$^+$
1869,52	194,877	
1879,503	139,8818	
2291,918	462,4195	
2581,97	31,8599	[OCT+2β-CD+Na]$^+$
2601,924	19,70599	[AVO+2β-CD+Na]$^+$

Here it can be evidenced the presence of different stoichiometries for the host guest system[52,53], as 1:1 H:G [AVO+ β-CD+H]$^+$, [OCT+ β-CD+Na]$^+$, [AVO+ β-CD+Na]$^+$ at m/z 1445, 1447 and 1467, respectively. For the stoichiometry 2:1, doubly charged peaks, m/z 1302 and 1312 for species [OCT+2 β-CD+2Na]$^{2+}$and [AVO+2 β-CD+2Na]$^{2+}$, as well as singly charged species at very low intensity [OCT+ 2 β-CD+Na]$^+$ and [AVO+2 β-CD+Na]$^+$ at m/z 2582 and 2602.

It must be noticed that octinoxate being less easily ionized, in this solvents system, with respect to avobenzone, results in a lower intensity of the mass peak. The spectrum of $(\beta\text{-CD})_2{\cdot}\text{AVO}$ and $(\beta\text{-CD})_3{\cdot}\text{OCT}_2$ after irradiation was similar, as shown in SI-19.

Unexpected peaks were found in these spectra at around 600 m/z and more precisely at 603, 623 and 643. These peaks were expected to appear only after irradiation, due to the formation of molecular dimers via [2+2] photoinduced cyclization.[23] MS/MS for all three peaks was conducted and it results that at 603 m/z, by increasing collision energy, the peak at 313 appeared, after MS/MS at 623 the peaks at 313 and 333 appeared (Figure 5) and after MS/MS at 643 the peak at 333 appeared. This means that the peaks at higher m/z are an artefact of the analysis, ionizing two molecules together.

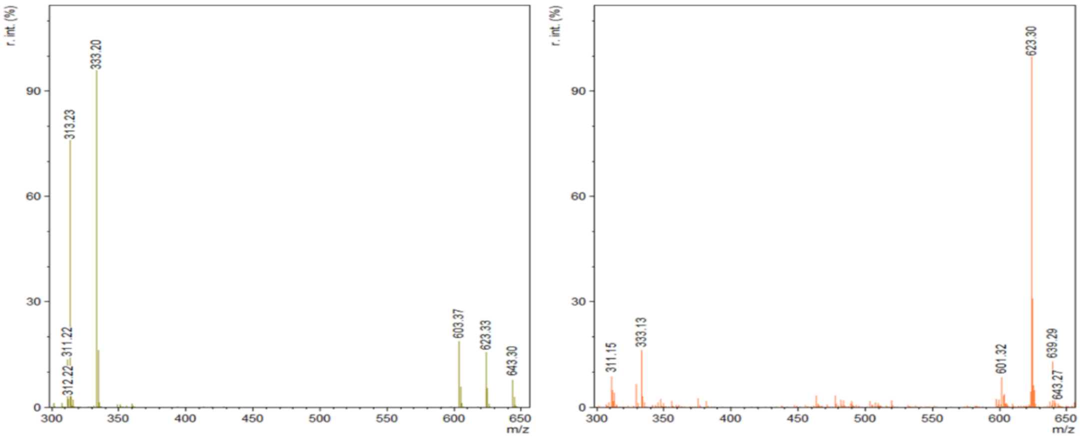

Figure SI-22. MS spectra for a mixture of avobenzone and octinoxate before (left) and after (right) UV irradiation. In the spectrum of the irradiated sample the peak revealing the photoadduct at 623 m/z ([2+2] photoreaction of AVO and OCTI) is predominant and also a small peak around 639 m/z, associated with the adduct [AVO+OCT+K]$^+$ is present here and could not be found before irradiation.

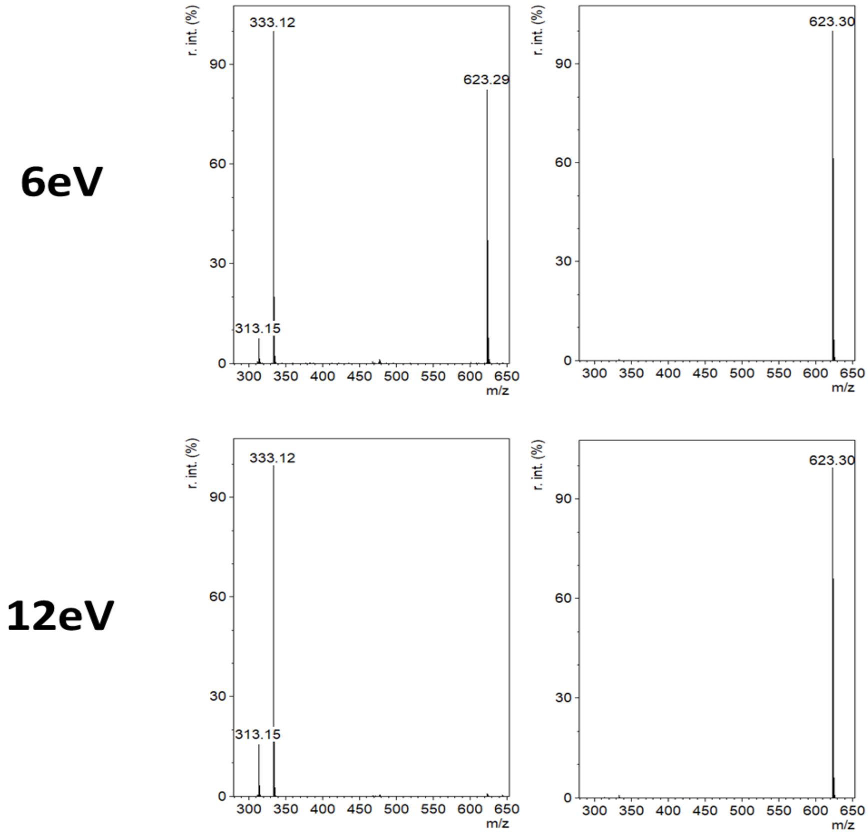

Figure SI-23. MS/MS spectra with collision energy at 6eV (top) and 12eV (bottom) of the peak at m/z 623 for: (left) a mixture of avobenzone and octinoxate, (right) the same mixture after irradiation. Peak at 623 highlights the photodimerization product.

UV-VIS spectra

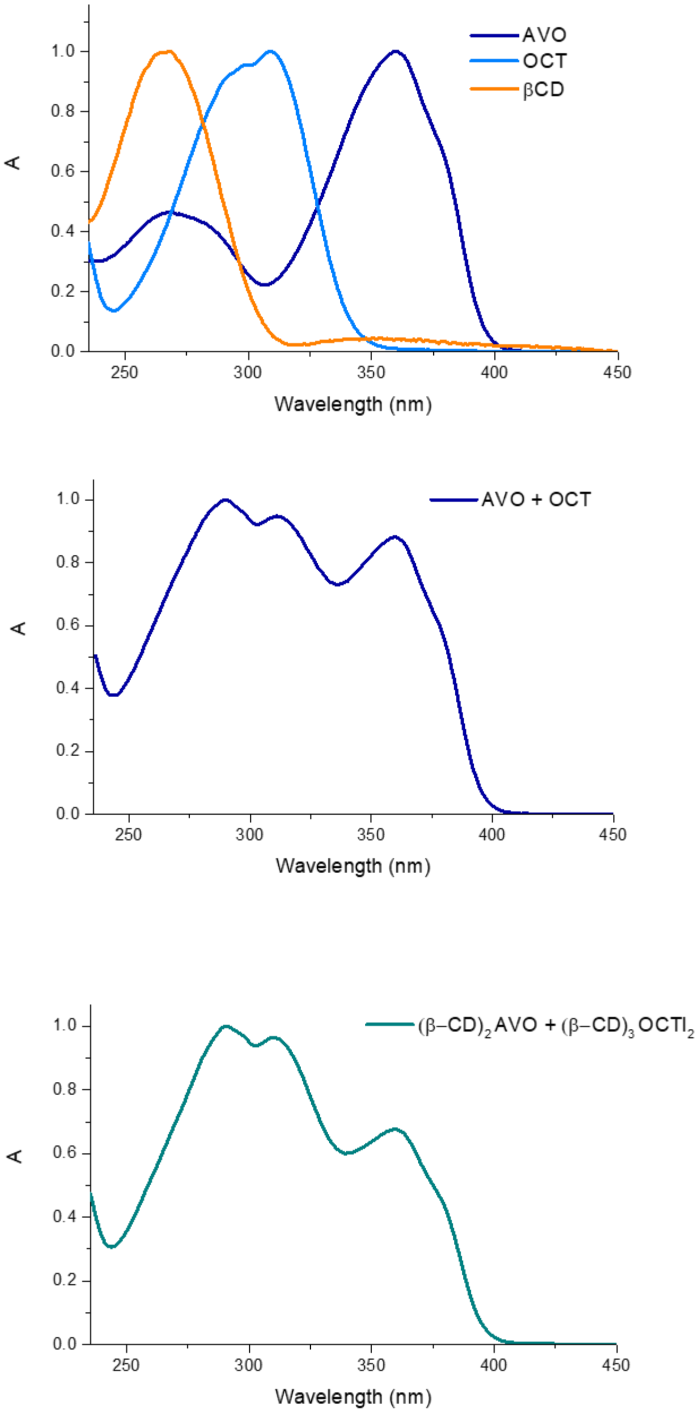

Figure SI-24. Normalized UV-VIS spectra of: (a) the three reactants used, (b) a solution containing equimolar amounts of the sunscreens, and (c) a solution containing an equimolar amount of (β-CD)$_2$·AVO, and (β-CD)$_3$·OCT$_2$. Note how the spectral features of the sunscreens remain unaltered after complexation.

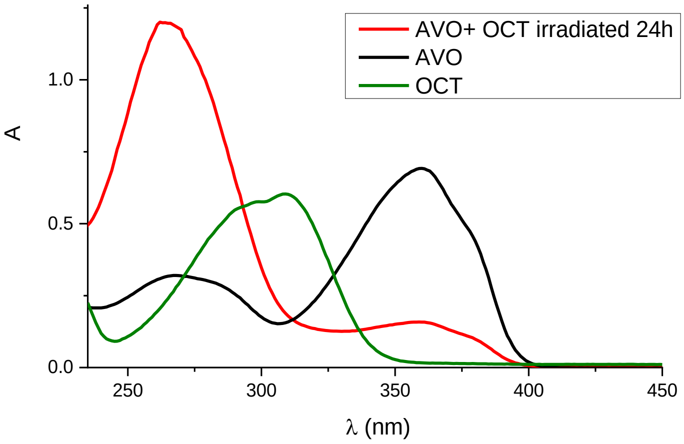

Figure SI-25. UV-VIS spectra recorded in a 50:50 water/ACN solution of avobenzone (black line), octinoxate (green line) and the mixture of the two irradiated for 24 hours (red line).

4.5 Conclusions

Along with the awareness that the UV radiation can be extremely dangerous for human health, the utilization of sun creams has become highly recommended. However, the UV filters contained in the common formulations can present low photostability, thus leading to the formation of species harmful for the health and the environment.

The quest for photostable sunscreens resulted in the investigation of new formulations, such as the inclusion of organic UV filters into β-CD molecules. This approach has been followed in this research project: β-CD inclusion complexes of the UV filters avobenzone and octinoxate were synthesized and characterized through solid-state methods, and were proven to effectively improve the photostability of the included organic filters.

References

1. Australian Institute of Health and Welfare. Melanoma skin cancer (AIHW). 2–3 (2016). at <http://www.aihw.gov.au/cancer/melanoma/>
2. Armstrong, B. K. & Kricker, A. The epidemiology of UV induced skin cancer. *J. Photochem. Photobiol. B Biol.* **63,** 8–18 (2001).
3. Sambandan, D. R. & Ratner, D. Sunscreens: An overview and update. *J. Am. Acad. Dermatol.* **64,** 748–758 (2011).
4. Serpone, N., Dondi, D. & Albini, A. Inorganic and organic UV filters: Their role and efficacy in sunscreens and suncare products. *Inorganica Chim. Acta* **360,** 794–802 (2007).
5. Morsella, M., D'Alessandro, N., Lanterna, A. E. & Scaiano, J. C. Improving the Sunscreen Properties of TiO2 through an Understanding of Its Catalytic Properties. *ACS Omega* **1,** 464–469 (2016).
6. Gaspar, L. R. & Campos, P. M. B. G. M. Photostability and efficacy studies of topical formulations containing UV-filters combination and vitamins A, C and E. *Int. J. Pharm.* **343,** 181–189 (2007).
7. Kockler, J., Oelgemöller, M., Robertson, S. & Glass, B. D. Photostability of sunscreens. *J. Photochem. Photobiol. C Photochem. Rev.* **13,** 91–110 (2012).
8. Cambon, M., Issachar, N., Castelli, D. & Robert, C. An in vivo method to assess the photostability of UV filters in a sunscreen. *J. Cosmet. Sci.* **52,** 1–11 (2001).
9. Wood, E. Impacts of Sunscreens on Coral Reefs Funded With the Support of the Government of Sweden and the Fondation Pour La Recherche Sur La Biodiversite. *ICRI* 20 (2018).
10. Schneider, S. L. & Lim, H. W. Review of environmental effects of oxybenzone and other sunscreen active ingredients. *J. Am. Acad. Dermatol.* **80,** 266–271 (2019).
11. Danovaro, R., Bongiorni, L., Corinaldesi, C., Giovannelli, D., Damiani, E., Astolfi, P., Greci, L. & Pusceddu, A. Sunscreens cause coral bleaching by promoting viral infections. *Environ. Health Perspect.* **116,** 441–447 (2008).

12. Downs, C. A., Kramarsky-Winter, E., Segal, R., Fauth, J., Knutson, S., Bronstein, O., Ciner, F. R., Jeger, R., Lichtenfeld, Y., Woodley, C. M., Pennington, P., Cadenas, K., Kushmaro, A. & Loya, Y. Toxicopathological Effects of the Sunscreen UV Filter, Oxybenzone (Benzophenone-3), on Coral Planulae and Cultured Primary Cells and Its Environmental Contamination in Hawaii and the U.S. Virgin Islands. *Arch. Environ. Contam. Toxicol.* **70,** 265–288 (2016).

13. Republic of Palau: Signing Statement SB No 10-135, SDI, HDI.

14. State of Hawaii: SB No. 2571, SD2, HD2, CD1.

15. Ouchene, L., Litvinov, I. V. & Netchiporouk, E. Hawaii and Other Jurisdictions Ban Oxybenzone or Octinoxate Sunscreens Based on the Confirmed Adverse Environmental Effects of Sunscreen Ingredients on Aquatic Environments. *J. Cutan. Med. Surg.* **23,** 648–649 (2019).

16. Adler, B. L. & DeLeo, V. A. Sunscreen Safety: a Review of Recent Studies on Humans and the Environment. *Curr. Dermatol. Rep.* (2020). doi:10.1007/s13671-020-00284-4

17. Palau is first country to ban 'reef toxic' sun cream. *BBC*

18. Damiani, E., Astolfi, P., Giesinger, J., Ehlis, T., Herzog, B., Greci, L. & Baschong, W. Assessment of the photo-degradation of UV-filters and radical-induced peroxidation in cosmetic sunscreen formulations. *Free Radic. Res.* **44,** 304–312 (2010).

19. Pattanaargson, S., Munhapol, T., Hirunsupachot, P. & Luangthongaram, P. Photoisomerization of octyl methoxycinnamate. *J. Photochem. Photobiol. A Chem.* **161,** 269–274 (2004).

20. Pattanaargson, S. & Limphong, P. Stability of octyl methoxycinnamate and identification of its photo-degradation product. *Int. J. Cosmet. Sci.* **23,** 153–160 (2001).

21. Cantrell, A. & McGarvey, D. J. Photochemical studies of 4-tert-butyl-4'-methoxydibenzoylmethane (BM-DBM). *J. Photochem. Photobiol. B Biol.* **64,** 117–122 (2001).

22. Dondi, D., Albini, A. & Serpone, N. Interactions between different solar UVB/UVA filters contained in commercial suncreams and consequent loss of UV protection. *Photochem. Photobiol. Sci.* **5,** 835–843 (2006).

23. D'Agostino, S., Boanini, E., Braga, D. & Grepioni, F. Size Matters: [2 + 2] Photoreactivity in Macro- and Microcrystalline Salts of 4-Aminocinnamic Acid. *Cryst. Growth Des.* **18,** 2510–2517 (2018).

24. D'Agostino, S., Taddei, P., Boanini, E., Braga, D. & Grepioni, F. Photo- vs Mechano-Induced Polymorphism and Single Crystal to Single Crystal [2 + 2] Photoreactivity in a Bromide Salt of 4-Amino-Cinnamic Acid. *Cryst. Growth Des.* **17,** 4491–4495 (2017).

25. Serpone, N., Salinaro, A., Emeline, A. V., Horikoshi, S., Hidaka, H. & Zhao, J. An in vitro systematic spectroscopic examination of the photostabilities of a random set of commercial sunscreen lotions and their chemical UVB/UVA active agents. *Photochem. Photobiol. Sci.* **1,** 970–981 (2002).

26. Schwack, W. & Rudolph, T. Photochemistry of dibenzoyl methane UVA filters Part 1. *J. Photochem. Photobiol. B Biol.* **28,** 229–234 (1995).

27. Afonso, S., Horita, K., Sousa E Silva, J. P., Almeida, I. F., Amaral, M. H., Lobão, P. A., Costa, P. C., Miranda, M. S., Esteves Da Silva, J. C. G. & Sousa Lobo, J. M. Photodegradation of avobenzone:

Stabilization effect of antioxidants. *J. Photochem. Photobiol. B Biol.* **140,** 36–40 (2014).

28. Coelho, L., Almeida, I. F., Sousa Lobo, J. M. & Sousa e Silva, J. P. Photostabilization strategies of photosensitive drugs. *Int. J. Pharm.* **541,** 19–25 (2018).

29. Giacomoni, P. U., Teta, L. & Najdek, L. Sunscreens: The impervious path from theory to practice. *Photochem. Photobiol. Sci.* **9,** 524–529 (2010).

30. Szejtli, J. Introduction and general overview of cyclodextrin chemistry. *Chem. Rev.* **98,** 1743–1753 (1998).

31. Connors, K. A. The stability of cyclodextrin complexes in solution. *Chem. Rev.* **97,** 1325–1357 (1997).

32. Trellu, C., Mousset, E., Pechaud, Y., Huguenot, D., van Hullebusch, E. D., Esposito, G. & Oturan, M. A. Removal of hydrophobic organic pollutants from soil washing/flushing solutions: A critical review. *J. Hazard. Mater.* **306,** 149–174 (2016).

33. Li, L., Liu, H., Li, W., Liu, K., Tang, T., Liu, J. & Jiang, W. One-step synthesis of an environment-friendly cyclodextrin-based nanosponge and its applications for the removal of dyestuff from aqueous solutions. *Res. Chem. Intermed.* **46,** 1715–1734 (2019).

34. Braga, S. S., Gonçalves, I. S., Herdtweck, E. & Teixeira-Dias, J. J. C. Solid state inclusion compound of S-ibuprofen in β-cyclodextrin: Structure and characterisation. *New J. Chem.* **27,** 597–601 (2003).

35. Caira, M. R., De Vries, E. J. C. & Nassimbeni, L. R. Crystallization of two forms of a cyclodextrin inclusion complex containing a common organic guest. *Chem. Commun.* **3,** 2058–2059 (2003).

36. Rácz, C. P., Borodi, G., Pop, M. M., Kacso, I., Sánta, S. & Tomoaia-Cotisel, M. Structure of the inclusion complex of Β-cyclodextrin with lipoic acid from laboratory powder diffraction data. *Acta Crystallogr. Sect. B Struct. Sci.* **68,** 164–170 (2012).

37. Wang, Q., Zhang, L. L., Wu, X. Q., Pan, Q. Q., Su, Y. H. & Li, H. X-ray powder diffraction data for inclusion complex of β-cyclodextrin with fraxinellone. *Powder Diffr.* **28,** 234–236 (2013).

38. Smith, V. J., Rougier, N. M., de Rossi, R. H., Caira, M. R., Buján, E. I., Fernández, M. A. & Bourne, S. A. Investigation of the inclusion of the herbicide metobromuron in native cyclodextrins by powder X-ray diffraction and isothermal titration calorimetry. *Carbohydr. Res.* **344,** 2388–2393 (2009).

39. Caira, M. R. On the isostructurality of cyclodextrin inclusion complexes and its practical utility. *Rev. Roum. Chim.* **46,** 371–386. (2001).

40. Ramos, A. I., Braga, T. M., Silva, P., Fernandes, J. A., Ribeiro-Claro, P., De Fátima Silva Lopes, M., Paz, F. A. A. & Braga, S. S. Chloramphenicol·cyclodextrin inclusion compounds: Co-dissolution and mechanochemical preparations and antibacterial action. *CrystEngComm* **15,** 2822–2834 (2013).

41. Lin, S. Z., Kohyama, N. & Tsuruta, H. Characterization of steroid/cyclodextrin inclusion compounds by X-ray powder diffractometry and thermal analysis. *Ind. Health* **34,** 143–148 (1996).

42. Djedaïni, F. & Perly, B. Nuclear magnetic resonance investigation of the stoichiometries in β-cyclodextrin:steroid inclusion complexes. *J. Pharm. Sci.* **80,** 1157–1161 (1991).

43. Kagawa, H., Sagawa, M. & Kakuta, A. 3-(4-tert-Butylphenyl)-3-hydroxy-1-(4-methoxyphenyl)-2-

propen-1-one: an SHG active β-diketone. *Acta Crystallogr. Sect. C* **49,** 2181–2183 (1993).

44. Divakar, S. Structure of a β-Cyclodextrin-Vanillin Inclusion Complex. *J. Agric. Food Chem.* **38,** 940–944 (1990).

45. Beyere, L., Yarasi, S. & Loppnow, G. R. Solvent effects on sunscreen active ingredients using Raman spectroscopy. *J. Raman Spectrosc.* **34,** 743–750 (2003).

46. Russell, N. R. & McNamara, M. FT-IR and raman spectral evidence for metal complex formation with β-cyclodextrin as a first sphere ligand. *J. Incl. Phenom. Mol. Recognit. Chem.* **7,** 455–460 (1989).

47. Costa, M. M. da, Alves, L. P., Osório, R. A. L., Pacheco, M. T. T. & Silveira, L. Detecting active ingredients of insect repellents and sunscreens topically in skin by Raman spectroscopy. *J. Biomed. Opt.* **23,** 1 (2018).

48. Tayyari, S. F., Rahemi, H., Nekoei, A. R., Zahedi-Tabrizi, M. & Wang, Y. A. Vibrational assignment and structure of dibenzoylmethane. A density functional theoretical study. *Spectrochim. Acta - Part A Mol. Biomol. Spectrosc.* **66,** 394–404 (2007).

49. Hammond, G. S., Borduin, W. G. & Guter, G. A. Chelates of β-Diketones. I. Enolization, Ionization and Spectra. *J. Am. Chem. Soc.* **81,** 4682–4686 (1959).

50. Rachmawati, H., Edityaningrum, C. A. & Mauludin, R. Molecular inclusion complex of curcumin-β-cyclodextrin nanoparticle to enhance Curcumin skin permeability from hydrophilic matrix gel. *AAPS PharmSciTech* **14,** 1303–1312 (2013).

51. Mohan, P. R. K., Sreelakshmi, G., Muraleedharan, C. V. & Joseph, R. Water soluble complexes of curcumin with cyclodextrins: Characterization by FT-Raman spectroscopy. *Vib. Spectrosc.* **62,** 77–84 (2012).

52. Al-Burtomani, S. K. S. & Suliman, F. E. O. Inclusion complexes of norepinephrine with β-cyclodextrin, 18-crown-6 and cucurbit[7]uril: experimental and molecular dynamics study. *RSC Adv.* **7,** 9888–9901 (2017).

53. Suliman, F. E. O. & Varghese, B. Inclusion complexes of pantoprazole with β-cyclodextrin and cucurbit[7]uril: experimental and molecular modeling study. *J. Incl. Phenom. Macrocycl. Chem.* **91,** 179–188 (2018).

CHAPTER 5

SUMMARY

The frame of this doctoral project was the synthesis and characterization of environmentally friendly crystalline materials through solid-state methods.

The research activity was focused on two main topics, that can be summarised as follows:

1. Optimization of materials of agrochemical interest, mainly through the co-crystallization method.
2. Improvement in the photostability of organic UV filters commonly used in sunscreen formulation by their inclusion into β-cyclodextrin.

1. The main topic of my PhD activity was based on the design and development of urea-based co-crystals as a novel class of crystalline fertilizers, aimed to improve the chemical-physical properties of urea - by reducing its water solubility/dissolution rate - and explicit an inhibition activity towards the enzymes urease and/or AMO. The inhibition activity of these materials was tested by the research group of prof. Stefano Ciurli - Laboratory of Bioinorganic Chemistry, Department of Pharmacy and Biotechnology, University of Bologna.

The first system succesfully synthesized and characterized was the molecular co-crystal urea·catechol. The dual objective of improving the chemical-physical properties of urea and inhibiting the enzyme urease was achieved: the water solubility and hygroscopicity of urea were reduced, while the inhibition activity carried out by catechol was improved. The second system developed was the ionic co-crystal $ZnCl_2 \cdot KCl \cdot$urea, which presented the added benefit of supplying the soil with other essential elements for the plants, i.e. macronutrients and micronutrients. Finally, urea was co-crystallized with $ZnCl_2$ and thiourea, an improved system thanks to its dual use as inhibitor of both urease and AMO.

A further development of this research project concerned the synthesis and characterization of crystalline materials based on AMO inhibitors, aimed to modulate the chemical-physical properties of these inhibitors in terms of water solubility, thermal stability, and inhibition activity. A thorough solid-state analysis of these materials was performed at the research institute BAM - Federal Institute for Materials Research and Testing, Berlin - where I have spent a 3-month research period under the supervision of Dr. Franziska Emmerling.

The compound mainly investigated was dicyandiamide, whose solid-state reactivity was explored by monitoring the mechanochemical reactions with two copper salts, i.e. $Cu(NO_3)_2 \cdot 3H_2O$ and $CuCl_2 \cdot 2H_2O$. The preliminary data suggested that the milling conditions can affect the formation of one polymorph/hydrate over other crystalline forms as well as the kinetic of the reactions.

2. This project - which represented a branch line of my research activity - was aimed to the optimization of the UV filters avobenzone and octinoxate, whose photostability is quite low despite of their extensive use in sunscreens formulations.

Through the inclusion of such compounds into the β-CD cavity, their photostability turned out to be dramatically improved, thus representing interesting systems for future applications.

The leitmotif of these two lines of research was the use of mechanochemistry as solvent-free synthetic method. Given the highlighted advantages related to this method in terms of sustainability, versatility and efficiency, it should be further developed for the synthesis of novel materials.

A future development of the project may rely on the design of materials able to control the release of chemicals (both agrochemicals and pharmaceuticals) such as MOFs (Metal Organic Frameworks), silicates (clays and zeolites) and clathrates, while maintaining the characteristics of bio- and eco-compatibility.